Investigation into Non-Aqueous Aluminium-ion Battery Electrolyte and Cathode Materials for Enhanced Power and Capacity

Liam Plunkett

This thesis is submitted for the degree of

Doctor of Philosophy

School of Engineering

Newcastle University

March 2021

Abstract

Energy storage is one of the most important resources in today's society. Developing this resource to be more efficient and sustainable is one of the biggest challenges to overcome. For decades, lithium has been at the forefront of energy storage, powering our technology from mobile phones to electric vehicles. The dwindling amount of available lithium left in the world signals that it's time for the next battery material. Aluminium is not only substantially more abundant across the world, making it cheaper with a lower carbon footprint, but due to its trivalency it possesses a larger capacity than monovalent lithium which could result in smaller, higher capacity and more affordable batteries.

This work investigated different electrolyte compositions of aluminium-ion batteries (AIB), a eutectic melt of 1-ethyl-3-methylimidazolium chloride with $AlCl_3$ and its impact on electrochemical stability, anode and cathode performance, and battery coulombic efficiency, degradation, and capacity. The anodic limit of the electrolyte increased with increasing $AlCl_3$ content due to formation of $Al_2Cl_7^-$ species. Electrolyte degradation studies revealed electrolyte oxidation produces chlorine gas which was detected as HCl. Several carbon-based and metal oxide cathode materials were investigated for AIBs. Cathode potential, mechanism of reaction, coulombic efficiency, specific capacity, and degradation rates were recorded. Charged and discharged cathode material characterisations were carried out using XRD, STM, and Raman spectroscopic techniques. The dominant two mechanisms were found to be chloroaluminate intercalation or electro-adsorption.

Cell tests were performed to study the interplay between the Al metal anode, cathodes, and varying electrolyte compositions on charge/discharge. Battery performance was assessed using key performance indicators: specific capacity, specific energy, and coulombic efficiency. Carbon-based materials displayed the greatest performance with graphite giving a specific capacity of 295 $mAhg^{-1}$ with an energy density of 500 $Whkg^{-1}$. A hybrid lithium-aluminium cell using an NMC 811 positive electrode resulted in a capacity of 58 $mAhg^{-1}$.

Acknowledgements

First and foremost, I would like to express my thanks to my supervisor Dr Mohamed Mamlouk for his unparalleled support and guidance throughout this project, for having the time and patience to deal with my questions and queries, and for always being able to teach me something new.

I would also like to thank:

- The Engineering and Physical Sciences Research Council for funding this research.
- Ravi Kumar and Gaurav Gupta; two great post-doctoral researchers who gave their time and expertise to help me when needed, and for making my time in the lab more enjoyable.
- The entire Merz Court technical team, never a dull moment to be had and always on hand to build whatever contraption needed or answer any questions.
- Both Maggie White and Steve Ward for running XRD samples for me in between their very busy schedules.
- The SAgE Analytical services team for help with Raman.
- Lukas Seidl and the team at TUM for hosting me and for use of their STM facilities.

Table of Contents

List of Figures

List of Tables

List of Abbreviations

Abbreviation	Definition
AIB	Aluminium Ion Battery
LIB	Lithium Ion Battery
CIB	Chloride Ion Battery
SHE	Standard Hydrogen Electrode – 0V
SCE	Saturated Calomel Electrode – 0.24V vs SHE
SEI	Solid Electrolyte Interface
GPE	Gel Polymer Electrolyte
SPE	Solid Polymer Electrolyte
LISICON	Lithium Super Ion Conductor
NASICON	Sodium Super Ion Conductor
EG	Ethylene Glycol
EC	Ethylene Carbonate
PC	Propylene Carbonate
DMC	Dimethyl Carbonate
HBD	Hydrogen Bond Donor
DES	Deep Eutectic Solvent
IL	Ionic Liquid
RTIL	Room Temperature Ionic Liquid
TbaTF	Tetrabutylammonium Trifluoromethanesulfonate
TBAC	Tetrabutylammonium chloride
EMC	Ethyl Methyl Carbonate
DM	Dipole Moment
ChCl	Choline Chloride
$PP_{14}Cl$	1-butyl-1-methyl piperidinium chloride
TFSI	Bis(trifluoro methylsulfonyl)imide
Emim	1-ethyl-3-methylimidazolium
Bmim	1-butyl-3-methylimidazolium
Emic	1-ethyl-3-methylimidazolium chloride
DCM	Dichloromethane

ET	Triethylamine hydrochloride
CAN	Acetonitrile
PAN	Polyacrylonitrile
PVDF	Polyvinylidene Fluoride
HFP	Hexafluoropropylene
PMMA	Polymethylmethacrylate
UGF	Ultrathin Graphitic Foam
HOPG	Highly Ordered Pyrolytic Graphite
rGO	Reduced Graphene Oxide
IPA	Isopropyl Alcohol
THF	Tetrahydrofuran
PEEK	Polyether Ether Ketone
TBAP	Tetrabutylammonium Perchlorate
XPS	X-Ray Photoelectron Spectroscopy
XRD	X-Ray Diffraction
STM	Scanning Tunnelling Microscopy
SEM	Scanning Electron Microscopy
BET	Brunauer Emmett Teller surface area analysis
EPMA	Electron Probe Microanalysis
SAXS	Small Angle X-Ray Scattering
CT	Computational Tomography
CV	Cyclic Voltammogram
FRA	Frequency Response Analysis
EIS	Electrochemical Impedance Spectroscopy
WE	Working Electrode
CE	Counter Electrode
REF	Reference Electrode

Chapter 1. Introduction

Energy storage technology is used almost everywhere; from storing energy harvested from renewable sources, down to the batteries in household appliances, electric vehicles, or even the watches on our wrists. Improving this technology is globally beneficial with energy storage being one of the major shortcomings in today's society.

What are batteries? Batteries are made up of one or more cells in series or parallel and convert stored chemical energy into electricity by way of electrochemical reactions. Each cell consists of two electrodes either side of an electrolyte: the anode, which is called the negative electrode, and the cathode, which is called the positive electrode. They take on either a positive or negative moniker due to the directional flow of electricity through them; the negatively charged electrons leave the anode, where a higher concentration of negative electrons are located and flow towards the electron deficient and therefore positive cathode on discharge. The electrons cannot flow through the electrolyte to the opposite side of the cell, instead flow through an external circuit, which provides power to whatever device is attached.

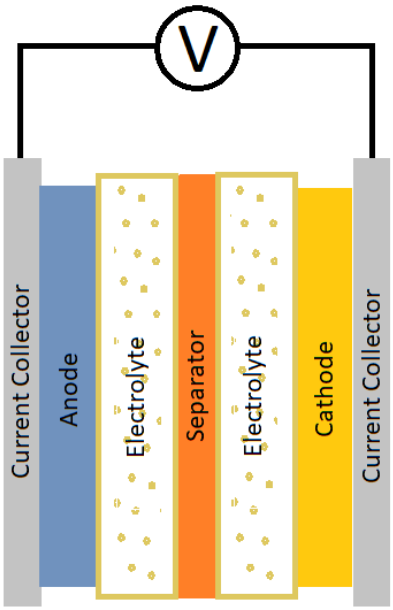

Figure 1-1: Structure of a battery showing the electrodes, electrolyte, and the separator connected to an external circuit through the current collectors

The electrolyte is often made up of a liquid but can also be solid. This liquid electrolyte is comprised of ions both positively and negatively charged, allowing for a transfer of charge across the cell between the electrodes, subsequently providing power and discharging the battery. The

electrodes are prevented from touching one another usually by a fibre separator which allows for the electrolyte and consequently ions to move freely through it.

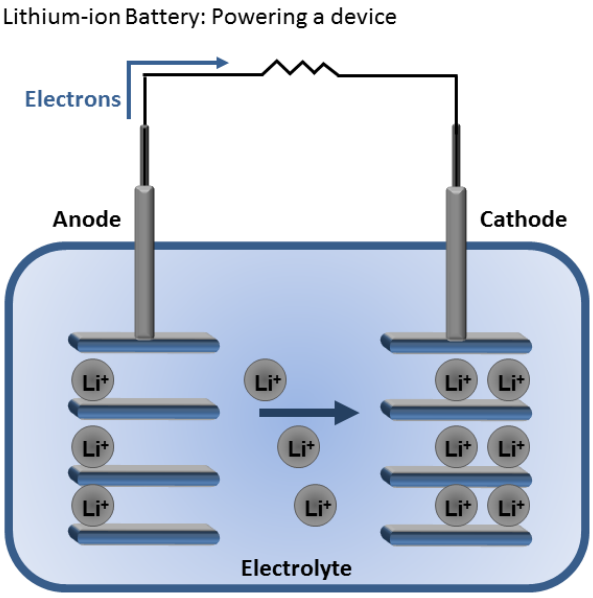

Figure 1-2 – Lithium-ion battery basic operation demonstrating the lithium ions transferring charge from anode to cathode [1]

When the external circuit of the cell is complete, the awaiting chemical reactions at the electrodes can begin, causing a current to be passed between the two main electrodes providing power to the external device. The reactions occurring at the electrodes are two distinct reactions: an oxidation reaction and a reduction reaction.

$$Oxidaton\ Reaction: \qquad Mx \rightarrow Mx^{+} + e^{-}$$

$$Reduction\ Reaction: \qquad Mz^{+} + e^{-} \rightarrow Mz$$

The oxidation takes place at the negative electrode, which provides the electrons that travel through the circuit that are needed by the positive electrode to carry out the corresponding reduction. These redox reactions that are taking place alter the oxidation state of the electrode materials by way of doping or intercalation. The electrolyte that sits between the electrodes allows for the mobility of ions that maintain the balance of charge across the cell. As more positive ions are formed at the anode, their concentration increases and the charge of the local environment changes to become more positive which encourages the positively charged cations to diffuse and migrate toward the cathode. The same is true of negative anions moving toward the anode.

A rechargeable, otherwise known as a secondary battery, can have an external current applied to it to replenish the original reactants; the cell can then be reused repeatedly. The opposite occurs when

charging a battery than when discharging it as the redox reactions are forcibly reversed; during discharge the reactants are used up as electrons flow from negative to positive, while during charge the current is reversed by an external power source that causes the electrons to flow from what was the positive electrode toward the negative electrode.

In the case of lithium-ion batteries, an example of $LiCoO_2$ electrode discharge equations are as below. The reverse (right to left) is true for charging.

$$Cathode: \quad Li_{1-x}CoO_2 + xLi^+ + xe^- \leftrightarrow LiCoO_2$$

$$Anode: \quad LiC_6 \leftrightarrow C_6 + Li^+ + e^-$$

Aluminium ion battery half-cell equations are as follows for an Aluminium/Carbon cell:

$$Cathode: \quad 3C_nAlCl_4 + 3e^- \leftrightarrow 3C_n + 3AlCl_4^-$$

$$Anode: \quad Al + 7AlCl_4^- \leftrightarrow 4Al_2Cl_7^- + 3e^-$$

The total charge a battery can hold, measured in mAh or coulombs, and subsequently the battery's runtime or recharge time depends on the type and amount of the materials used for the electrodes as well as the electrolyte. It can be reasoned from these equations that in Al-ion batteries, the electrolyte, in addition to its role to allow movement of ions, plays a distinct role in storing the cell's charge which is not generally the case. When charging, chloroaluminate ions are intercalated into the cathode while being regenerated during the plating of aluminium onto the anode. The electrolyte essentially depletes its store of $Al_2Cl_7^-$ to charge and replenishes it when discharging, acting in a similar fashion to a hybrid redox flow battery, whereas for Lithium cells the Li^+ ion travels through the electrolyte after leaving the anode and transferring charge by reacting with the cathode; it is the electrodes that deplete and restore. This charge capacity is limited by how much of the active material we apply and the change of its oxidation state, and so specific capacity is reported per mass in $mAhg^{-1}$. In the case where the electrolyte constitutes part of the battery capacity such as in redox flow batteries, concentration of ions stored in electrolyte and their change of oxidation state are limiting factors.

1.1 Research Questions

Studies have previously investigated electrolytes for their reaction kinetics or for their specific charge transferring ion. Most have researched a single electrode material or type. Few studies

expand to incorporate comparisons of multiple electrode materials and so there is a lack of a holistic approach to aluminium battery research that builds upon an initial electrolyte or electrode study.

When comparing different aluminium ion batteries across separate studies, the degree of comparability is questionable as the experimental methodology and calculations may not be identical.

From these gaps in the literature, certain questions can be asked:

- Which electrolyte is most suitable for Aluminium-ion batteries?
- Which electrode material performs better for secondary Aluminium-ion batteries?
- How does the charging mechanism of electrode materials correlate across different characterisation techniques?

The coming chapters will look into existing literature on Lithium-ion as well as Aluminium-ion batteries, researching the electrolyte and electrode materials used. Following this will be a breakdown of a battery into constituent parts investigating the electrolyte and electrode behaviour and what is standing in the way of superior performance.

1.2 Aims

The electrolyte is one of the key components of a battery and must be able to work in tandem with the electrodes. Aiming to understand the mechanisms by which the electrolyte functions as well as finding out any limitations is key to developing a successful battery.

The need for cheaper alternatives to lithium-ion batteries warrants further study into aluminium ion batteries. This project aims to investigate a variety of electrode materials for use in an aluminium ion battery setting and understand how they influence the power output, capacity, and recharge ability.

1.3 Objectives

- Review existing literature on lithium ion and aluminium ion batteries
- Carry out voltammetry on different electrolyte ratios to determine oxidation and reduction limits as well as degradation products.
- Carry out voltammetric tests to assess the performance of different carbonaceous electrodes.

- Carry out voltammetric tests to assess the performance of different positive electrode materials.
- Characterisation of positive electrode materials at different states of charge to assess intercalation ability.
- Use assessment criteria of specific capacity and specific energy to determine the stability and rechargeability of the overall cell.

Chapter 2. Review of Literature

2.1 Aluminium Ion Batteries

2.1.1 Background

Lithium has been the dominant material choice for ion batteries for decades, due to the wealth of research that has been carried out across the globe. The first commercial lithium ion battery was released by Sony in 1991 [2] after a breakthrough by Goodenough et al. 10 years earlier after his team investigated a better cathode material: Li_xCoO_2, that provided superior performance in a reversible battery system [3]. Lithium-ion batteries have since come to power computers, mobile devices, electric vehicles, as well as energy storage. However, lithium and cobalt resources are limited and have become increasingly more expensive with lithium reaching a high of £19,500 per tonne in 2017 [4] but has since been on the decline as presumably supply has increased. Incidents have also occurred that question the safety of lithium ion batteries; they have been known to overheat, causing a small explosion [5]. These incidents occur due to the formation of what is known as dendrites. Dendrites are long, thin pieces of pure metal, formed from the constant deposition of metal ions on top of each other which advance from one electrode to the opposite electrode. They grow so large, piercing the separator and causing a short circuit as the two electrodes effectively touch one another. This leads to the death of the cell and potentially ignition due to poor thermal stability [6].

Aluminium has also been researched over the last few decades in an effort to try and supplant lithium as the leading metal for rechargeable batteries. Aluminium ion batteries provide benefits over lithium such as being inherently safer and being more abundant worldwide and therefore a cheaper alternative at a cost of roughly £1,500 per tonne in 2018 [7]. An important characteristic in determining the effectiveness of a battery is the specific energy; the power produced by the cell per unit weight. A material used for an electrode that can hold a large amount of energy per unit weight is more beneficial to the energy industry as this would lead to cheaper or longer lasting batteries per charge that is particularly important for transport applications.

Due to its trivalent nature, Al has the potential for large theoretical gravimetric energy densities meaning that it possesses more energy per unit mass, being able to transfer three electrons for every atom, three times more than the monovalent lithium atom. Compared to lithium-ion batteries, which are used in most modern-day electronics, an aluminium-ion battery utilising an λ-Mn_2O_4 cathode has a theoretical gravimetric specific energy of 1060 $Whkg^{-1}$ and a theoretical capacity of

400 $mAhg^{-1}$ [8] compared to 593 $Whkg^{-1}$ for the lithium-ion variety, assuming single metal ion intercalation, with a theoretical capacity of 148 $mAhg^{-1}$. Calculations for these theoretical values can be found in Appendix 2. This isn't the case in the previous example equation, in which the intercalating ion is tetrachloroaluminate, having a single electron charge which would reduce the figures of AIBs to a third of their theoretical values. Research into aluminium ion batteries is therefore filled with potential and provides interesting materials to investigate.

2.2 Electrolyte Materials

2.2.1 Aqueous Electrolytes

Aqueous electrolytes have very good conductivities due to water being a strong polar aprotic solvent with a dielectric constant of 80, which can fully disassociate a large number of inorganic salts, and ions generally have large diffusion coefficient in aqueous solutions. These water based electrolytes have been used with lithium ion batteries, where reversible intercalation into the positive electrode took place at potentials lower than that of water oxidation, though due to the reduction of water at the negative electrode in the cell leading to hydrogen evolution, with over all a potential stability window of only 1.23 V [9].

$$Hydrogen\ Evolution\ Reaction: \qquad 2H^+ + 2e^- \rightarrow H_2 \qquad E^o = 0.00\ V$$

$$Oxygen\ Evolution\ Reaction: \quad 2H_2O \rightarrow 4H^+ + 4e^- + O_2 \quad E^o = +1.23\ V$$

This smaller window means a smaller energy density is available in the cell compared to that of standard LIBs. However, with the use of a gel polymer electrolyte (GPE) and a film of a commercial lithium super ion conductor (LISICON) on the lithium electrode, the stability of the electrode in the electrolyte increased along with its energy density, with no hydrogen evolution detected [10]. The LISICON consists of Li_2O–Al_2O_3–SiO_2–P_2O_5–TiO_2–GeO_2. The increased performance is due to the Li^+ ions being able to transfer through both the gel polymer electrode as well as the LISICON film at the required potential while the unwanted aqueous ions and water are kept at bay in the electrolyte. As the potential reaches that required for hydrogen evolution, there is no contact for electron donation and therefore no hydrogen evolution occurs. The GPE coating and the LISICON film in this scenario allow for the operation of a high voltage battery in aqueous conditions. The GPE is required not only to ensure better contact with the lithium metal but to increase the electrochemical stability of the LISICON and protect the solid electrolyte from changes in volume attributed to stripping or deposition of lithium metal. In order to work with Al^{3+}

ions, an aluminium super ion conductor would be needed in combination with a GPE suitable for aluminium.

With the increase in concentration of aqueous electrolytes, an increase in conductivity is seen, as more ions are available to transfer the charge. However, a peak concentration level or saturation point will be reached, whereby high concentration results in an increase in electrolyte viscosity and decrease in diffusion coefficient, and the ionic density causes additional electrolyte to exist in molecular form obstructing the flow of electricity, limiting and possibly decreasing the conductivity [9]. Comparing the conductivities of aqueous versus non-aqueous: aqueous electrolytes such as $LiNO_3$ solution have been shown to have conductivities of 10^{-1} Scm^{-1} compared to non-aqueous electrolytes, such as $LiPF_6$ mixed with ethylene carbonate (EC) and dimethyl carbonate (DMC), which resulted in a conductivity 17 times lower [11]. This review also looked at how aqueous electrolytes also have a lower activation energy of interfacial ion transfer than organic electrolytes, around 25 $kJmol^{-1}$ compared to 50 $kJmol^{-1}$ respectively, meaning less energy needed for intercalation of Li^+ ions into and out of the positive electrode. Aqueous electrolytes also prevent films or solid electrolyte interfaces (SEI) from forming on the negative electrode as opposed to organic electrolytes. The absence of an SEI allows for direct contact of the ions to the electrode resulting in no extra resistance to the charge transfer [9]. This also leaves the anode exposed to the possibility of side reactions with the electrolyte. Faster charge transfer kinetics observed by aqueous electrolytes over organic mean that identical concentrations produce lower overall resistances in the former.

When it comes to aqueous AIBs, the well-known and promising $AlCl_3$ salt can be used if prepared correctly. If mixed directly with water, the hygroscopic nature causes the exothermic release of Cl_2 gas and HCl, but dissolving aluminium oxides in HCl generates aqueous aluminium hexahydrate: $Al(H_2O)_6Cl_3$. Liu et al. demonstrates the use of an aqueous 1 molar $AlCl_3$ electrolyte operating between -1.5 V to -0.1 V vs SCE stably to reversibly intercalate Al^{3+} ions into the positive electrode [12]. Similar behaviour is reported by Lahan et al. successfully intercalating and de-intercalating Al^{3+} showing electrochemical stability up to 0.5 V vs Ag/AgCl [13] . This was directly compared to aqueous $Al_2(SO_4)_3$ and $Al(NO_3)_3$ electrolytes, the former of which gave slightly lower capacity performance but greater coulombic efficiency while the latter displayed large negative currents indicating H_2 evolution. With $AlCl_3$ and $Al_2(SO_4)_3$ outperforming $Al(NO_3)_3$, additions of SO_4^{2-} and Cl^- ions were added to the electrolyte which boosted performance sharpening the redox peaks [14]. Without these additional ions, $Al(NO_3)_3$ delivers extreme rapid decay in capacity while $AlCl_3$ is

shown to outperform even $Al_2(SO_4)_3$ due to a higher conductivity and slower capacity decay of around 700 $mAhg^{-1}$ down to 150 $mAhg^{-1}$ after 350 cycles compared to around 800 $mAhg^{-1}$ down to 150 $mAhg^{-1}$ over 100 cycles. An aqueous $Al_2(SO_4)_3/Zn(CHCOO)_2$ electrolyte has also been reported by Wang et al. which shows good stability allowing for large redox peaks compared to similar electrolytes missing Al^{3+} ions which only show capacitive behaviour [15]. The inclusion of aluminium in the electrolyte therefore boosts the intercalation ability of the electrolyte.

Aqueous electrolytes have large conductivities and can prevent SEI formation, however due to their voltage window being limited by hydrogen evolution when a compatible GPE is not used; they are not a good route for further study within the timeframe of this project.

2.2.2 Non-Aqueous Electrolytes

2.2.2.1 Solvents

Knowing more about the solvents that make up electrolytes can allow for a custom-made medium that is suited to battery design needs. Petrowsky et al. investigated LIB electrolytes regarding the use of solvent viscosity as well as their dipole moment, looking closely at the solute tetrabutylammonium trifluoromethanesulfonate (TbaTF). This is because the two components of an electrolyte solvent generally consist of a high dielectric component to maximise the charge that can be carried, and a low viscosity component to increase the electrolyte's ion mobility. This low viscosity addition is needed, as the first component would have a high boiling point and consequently a high viscosity. An equal ratio of the two often produce an electrolyte with a higher conductivity than if they were separate. The dipole moment in a solvent affects the conductivity of the electrolyte and so a higher dipole moment is preferred. TbaTF in propylene carbonate (PC) displayed a higher conductivity of 4.4 $x10^{-3}$ Scm^{-1} compared to TbaTF in ethyl methyl carbonate (EMC) at 3.26 $x10^{-4}$ Scm^{-1}. The dipole moments of PC and EMC are 4.94 D and 0.89 D respectively with PC and its high DM giving over an order of magnitude higher conductivity. 1, 2-dimethoxyethane has a low viscosity and a dipole moment of 1.75 D, thus aiding in reducing the overall viscosity. A combination of solvents for TbaTF using 1, 2-dimethoxyethane and PC gives a higher conductivity of 6.24 $x10^{-3}$ Scm^{-1} [16].

2.2.2.2 Additives

There are additions to a solvent/ salt mixture such as receptors, that can complex ions and increase the electrolyte solubility. Boron-based anion receptors have been added to LiF, complexing the fluorine anions [17]. The larger complexes aid in the dissociation of the salt in turn increasing the

electrolyte conductivity. The trialkyl and triaryl-borates and boranes are stable up to 5.1 V vs. Li/Li^+. The complexation of the anions in solution helps to disassociate the salt that is introduced, increasing the transference numbers of the ions and subsequently increasing the conductivity. The problem of a solid electrolyte interface (SEI) has been overcome as it was found that the complexing anions could also dissolve and remove insoluble inorganic materials from the SEI, further increasing conductivity and cell performance that was thought to be lost. These receptors could be used to further complex ions in AIBs to speed up the dissociation of the salt, which would potentially increase the conductivity.

2.2.2.3 Deep Eutectic Solvents

Deep eutectic solvents (DES) comprised of a salt and a complex anion, utilise hydrogen bonds or the metal halide bonds of the anion to interact. When combined, they lower the overall mixtures melting point to create a liquid at room temperature. Increasing the salt content within the liquid increases the viscosity of DESs due to the decrease in molar free volume. Similarly, with increasing hydrogen bond donor (HBD) molecule size, slower molecular mobility also results in increasing viscosity. The conductivity is linked to the amount of salt contained within the DES and therefore linked to the viscosity; too little and there are not enough ionic species to conduct electrons, but too much and although there are more ions to carry charge, the mixture becomes too viscous which will prevent the motion of the ionic species. Increasing the temperature decreases the viscosity, which raises the conductivity. Research that has been done on tetrabutylammonium chloride (TBAC) with HBDs looked at glycerol, ethylene glycol (EG), and triethylene glycol [18]. For the TBAC / EG mix, a high conductivity of 7.22 $mScm^{-1}$ was reached using a 1:4 ratio at an elevated temperature of 353.15 K, past its eutectic melting point of 256.31 K. The conductivity declines almost linearly with temperature down to around 2.5 $mScm^{-1}$ at 300 K. The use of ethylene glycol outperformed both alternatives with lower viscosities and much higher conductivities of a factor of at least three.

There are four different types of DESs, based on quaternary ammonium or phosphonium salts along with a metal halide, hydrated metal halide, or organic components [18]. They are also cheaper than ILs. Quaternary ammonium ions are more electrochemically stable and harder to reduce compared to imidazolium and pyridinium ions making them a better choice for use as an electrolyte. When used with $AlCl_3$, the four attached alkyl groups need to be long enough to bring down the melting point of the mixture to room temperature as the eutectic point would not be low enough otherwise. The longer the alkyl chains the lower the overall melting point is, but at the cost of increasing the

viscosity and lowering the electrolyte conductivity. Aryl groups can also be used to lower the melting point. Smaller aryl components have the benefit of not raising the viscosity or decreasing the conductivity beyond that which is still practical, yet the conductivity and viscosity performance are still comparably low compared to 1-ethyl-3-methylimidazolium chloride [19].

Choline chloride is a quaternary ammonium salt with a melting point of 575 K. However, when used in conjunction with urea, this allows for a eutectic point of 285 K. An ethylene glycol mix creates a eutectic melt at an even lower temperature of 233 K. The choline chloride / ethylene glycol mix has the benefit of being non-corrosive and provides a high current efficiency with negligible gas evolution when used for electro-polishing stainless steel or zinc electroplating. The same DES could be used to transport aluminium instead of zinc ions, or chloride instead of metal ions [18]. Fullarton investigated the use of DESs as an electrolyte in a Zn-polymer battery finding that the choline chloride/ ethylene glycol (ChCl/EG) and $ZnCl_2$/EG electrolytes had excellent performance with respective capacitances of 206 Fg^{-1} and 139 Fg^{-1}. When using ChCl, cationic transfer of $[Ch]^+$ was dominant over the $[2EG.Cl]^-$ anion, although in the $ZnCl_2$/EG electrolyte, the anionic transfer of $[ZnCl_4]^{2-}$ was dominant over the neutral molecule [EG] being transferred [20]. This could allow products to form at different electrodes in AIBs if ionic transfer is dominated by a particular ion.

Chlorine ion batteries (CIB) are a lesser researched battery system, though 1-butyl-1-methyl piperidinium chloride ($PP_{14}Cl$) has proven to be an effective electrolyte for transferring chloride ions across a CIB when mixed with propylene carbonate (PC), with a conductivity of $4.4x10^{-3}$ Scm^{-1} and a window of 3.2 V vs Li/Li^+ [21]. When mixed with 1-butyl-1-methylpiperidiniumbis (trifluoromethylsulfonyl)imide ($PP_{14}TFSI$) however, the conductivity of the electrolyte decreases to only $0.61x10^{-3}$ Scm^{-1} [22].

2.2.2.4 Ionic Liquids

2.2.2.4.1 Lithium-Ion Batteries

LIBs have used ILs containing imidazolium salts and have noted that their reduction potentials are around 1.5 V vs Li/Li^+ [23] or 0.17 V vs Al/Al^{3+}. Other salts tested include piperidinium and pyrrolidinium salts, which possess lower reduction potentials, and higher oxidation potentials at 6 V vs Li/Li^+ which allow for use in high voltage batteries. As for the solvent, sulfones were found not only to have a lower viscosity to aid in electrode interactions but to have a high oxidation potential of 5.5 V which could be made higher through the use of functionalisation with strong

electron withdrawing groups such as quaternary amine or ammonium groups or sulfonates. These salts could possibly be used in AIBs for high voltage applications.

2.2.2.4.2 Aluminium Ion Batteries

Non-aqueous electrolytes are used to protect electrodes or used to increase the electrolyte stability window above 1.23 V of that of aqueous electrolyte. Electrolytes can consist of a room temperature ionic liquid (RTIL); a molten salt comprised of an anion and a cation. An example of this is the combination of $AlCl_3$ and 1-ethyl-3-methylimidazolium chloride (EmimCl), two salts which form a eutectic mix.

$$AlCl_3 + EmimCl \rightarrow AlCl_4^- + Emim^+$$

$AlCl_3$ mixed with EmimCl offers a reliable electrochemical window of 2.45 V with a coulombic efficiency of 96%, although when this window is increased beyond this towards 2.6 V vs Al/Al^{3+}, the efficiency drops to 51% due to side reactions [24].

An electrolyte combining $AlCl_3$ with Acetamide performed in much the same way with different working electrodes as when EmimCl is used. Increasing the ratio of $AlCl_3$ results in larger oxidation and reduction peaks due to the decrease in viscosity allowing for a higher ion mobility [25]. This increased performance ends when the ratio reached 1.5 mol, attributed to the increased amount of $Al_2Cl_7^-$ hindering the intercalation of $AlCl_4^-$. Decreasing the viscosity is theorised to increase capacity so dichloromethane (DCM) is used, however an increase of DCM further than a 30% addition resulted in coulombic efficiency losses.

There are different rates of migration for anions and cations between the electrodes with larger ions moving slower than smaller unencumbered ions, and so the concentration gradient between the electrodes is increased [26]. In an AIB with EmimCl, this would mean that the larger $Emim^+$ cations would be slower than smaller Cl^- anions, unless the Cl^- was complexed into larger anions therefore reducing the concentration gradient. The solvation of anions with $Emim^+$ would also hinder the movement of the anion. The directional momentum therefore depends on the ratio of cations to anions determining which ionic force pulls harder.

Using an electrolyte made from $AlCl_3$ and pyridinium chloride allows for intercalation of $AlCl_4$ into the cathode, the presence of which was confirmed by Raman spectra of the electrolyte showing the presence of $AlCl_4^-$ and $Al_2Cl_7^-$. XPS spectra also revealed that intercalation of these ions took place within the spherical graphite electrode. The cell cycled between 0.5-2.5 V vs Al/Al^{3+}

maintaining a coulombic efficiency of 97% after 500 cycles, proving electrolytic stability. Cycling to 2.6 V reduced the efficiency to 79% which was attributed to side reactions [27]. This is most likely degradation of the electrolyte as the oxidation potential was reached.

An electrolyte of $AlCl_3$ reacted with 4-ethylpyridine in different ratios up to a molar ratio of 1.4 $AlCl_3$ also showed signs of degradation, however this occurred earlier above potentials of 2.3 V. The electrolyte was intended to avoid the corrosivity caused by $Al_2Cl_7^-$ anions and replace it with an Al^{3+} cation as the electroactive species. No $Al_2Cl_7^-$ ions were detected with Raman and $AlCl_4^-$ remained the intercalated ion confirmed by XPS when cycled between 0-2.7 V. Beyond 2.3 V, coulombic efficiencies decrease suggesting degradation of the electrolyte [28].

Chloride free electrolyte have been investigated that could avoid the chloride oxidation that limits the electrochemical potential window in chloride electrolytes. A bis(trifluoromethyl)sulfonamide (TFSI) anion was used with Al^{3+} in acetonitrile (ACN), providing reversible Al deposition [29]. This electrolyte provides a larger potential window of 3.5 V compared to 2.5 V when using $AlCl_3$/ EmimCl concluding that the chloride oxidation reactions had been avoided. A slight overpotential was caused by an oxide layer on the aluminium electrode which is normally corroded via chloride ions [30].

A comparison of the $AlCl_3$/Emim to a new $AlCl_3$ triethylamine hydrochloride ($AlCl_3$/ET) electrolyte, showed increased capacity results of 85 $mAhg^{-1}$ and 58 $mAhg^{-1}$ at 1 Ag^{-1} and 5 Ag^{-1} of $AlCl_3$/Emim were held up against 99 $mAhg^{-1}$ and 78 $mAhg^{-1}$ at 1 Ag^{-1} and 5 Ag^{-1} of $AlCl_3$/ET. Coulombic efficiencies for the two electrolytes were similarly in the high 90%s at 1 Ag^{-1}, though for 5 Ag^{-1} efficiencies ventured both above and below 100% [31].

2.2.3 Porous Membrane Separator

A review on LIB membrane separators by Lee at al. explains that battery separators should have good wettability and porosity characteristics as electrolyte absorption is required for the transport of ions, and retention aids in low internal resistance and high ionic conductivity. Typical membrane thicknesses would be 20-50 um although LIBs have a smaller 20-25 um range. Thinner separators reduce resistance leading to higher power and energy densities while thick separators increase resistance but also increase cell safety due to increased mechanical strength [32].

The review carries on discussing how electrolyte membranes do not need additional liquid electrolyte in order to conduct ions across it due to their high ionic conductivity. A subcategory of

electrolyte membranes: solid ceramic electrolytes, such as LISICON, NASICON or glass ceramics have proven successful [32]. They have high conductivities and electrochemical stability windows, though their brittleness makes them a poor choice in ion batteries. The super ion conductor LISICON, which as discussed previously has the ability to avoid the hydrogen redox reactions can work at various temperatures, so although the scope of this project will focus on room temperature electrolytes, the ability to operate at higher temperatures up to 80^{o}C make for an intriguing material choice. Solid polymer electrolytes (SPE) have low conductivities due to the crystalline structure limiting the transport of the ions [33]. Gel polymer electrolytes (GPE) membranes possess increased conductivities to the aforementioned types of 10^{-3} Scm^{-1} for polyacrylonitrile (PAN) compared to SPEs at around 10^{-7} Scm^{-1}. GPEs also have a large electrochemical stability window of up to 4.5 V for PAN at room temperature, making them a more reasonable choice over ceramic electrolytes. Composite electrolytes; the combination of inorganic materials into SPEs or GPEs have shown increased electrochemical stability and higher conductivities for example poly(butyl methacrylatestyrene) filled with SiO_2 exhibited results of a 5.2 V stability window and $2.15x10^{-3}$ Scm^{-1} respectively. Other inorganic filling materials include Al_2O_3, TiO_2 and MgO. Using ILs to fill GPEs also results in high conductivities; filling polyvinylidene fluoride hexafluoropropylene (PVDF-HFP)/ polymethyl methacrylate (PMMA) with BMIM-BF_4 achieved $1.4x10^{-3}$ Scm^{-1} within a stability window of 4.5 V.

Aluminium tungstate $Al_2(WO_4)_3$ has been used as a solid electrolyte with a conductivity of $4x10^{-6}$ Scm^{-1} at 600^{o}C [34] capable of conducting Al^{3+} and plating onto platinum and aluminium, confirmed with SEM and electron probe microanalysis (EPMA) [35]. $Al_2(WO_4)_3$ as an electrolyte, only exists as a thin film of 10-20 μm, small enough that it does not affect cell resistance [36]. The electrolyte performs stably between voltages of 0.8-2 V however pores formed on the material believed to be due to sub-standard fabrication methods. Thicker forms of the film exhibit microcracking due to the thicker and more brittle nature.

Current aluminium ion battery (AIB) technology has shown that RTILs provide good performance and still offer much to be explored. Their many benefits include displaying a high thermal stability, a low flammability/ volatility, and have large electrochemical windows. These windows have been shown to be determined by the stability of the anions and cations [23]. Many studies have gained success with the use of $AlCl_3$ mixed with EmimCl [24, 37] which would allow for stable investigation of electrode materials. The use of TFSI to avoid chloride oxidation to extend the

electrochemical window also offers opportunities and could be studied to create high voltage batteries.

Table 2-1 Comparison of electrolyte conductivity and voltage window

Electrolyte	Conductivity (Scm^{-1})	Electrochemical Potential Window (V)	Reduction Potential (V)	Oxidation Potential (V)	Reference
LISICON	$5x10^{-3}$	-	-	-	[38]
$LiNO_3$(aq)	$1.7x10^{-1}$	2.5	-0.75 vs Ag	1.75 vs Ag	[11, 39]
$LiPF_6$/EC/DMC	10^{-2}	-	-	-	
$Al(H_2O)_6Cl_3$	$1.3x10^{-1}$	1.3	-1.43 vs SCE	-0.1 vs SCE	[12, 40]
$Al(NO_3)_3$ (aq)	$1.8x10^{-1}$	-	-	-	
TbaTF/PC	$4.4x10^{-3}$	-	-	-	[16]
TbaTF/EMC	$3.26x10^{-4}$	-	-	-	
TbaTF/PC/1, 2-dimethoxyethane	$6.24x10^{-3}$	-	-	-	
TBAC/EG	$7.22x10^{-3}$	-	-	-	[18]
ChCl/EG	$8.53x10^{-3}$	2.1	-0.8 vs Ag	1.3 vs Ag	[41-43]
$PP_{14}Cl$/PC	$4.4x10^{-3}$	3.2	-	3.2 vs Li	[21]
$PP_{14}Cl/PP_{14}TFSI$	$6.1x10^{-4}$	1.9	-	-	[22]
$AlCl_3$/EmimCl	-	-	-	2.45 vs Al	[24]
$AlCl_3$/pyridinium chloride	$5.1x10^{-4}$	-	-	2.5 vs Al	[27]
$AlCl_3$/ 4-ethylpyridine	$9.1x10^{-4}$	-	-	2.3 vs Al	[28]
Al(TFSI)/ACN	-	3.6	-0.7 vs Ag	2.9 vs Ag	[29]
$AlCl_3$/ET	-	-	-	2.54 vs Al	[31]
PAN-based	10^{-3}	4.5	-	-	[32]
SiO_2/Poly(butyl methacrylatestyrene)	$2.15x10^{-3}$	5.2	-	-	
PVDF-HFP/PMMA/ Bmim-BF_4	$1.4x10^{-3}$	4.5	-	-	
$Al_2(WO_4)_3$	$4x10^{-6}$	1.2	-	-	[34, 36]

2.3 Electrode Materials

2.3.1 Aluminium

In alkaline electrolytes, an aluminium negative electrode revealed under SEM that small current densities etched small pores into the metal, while larger current densities created larger pores, believed to be due to the aluminium dissolution reaction occurring at various rates across the surface [44]. Looking into the chemical stability of aluminium electrodes when exposed to acidic electrolytes, in particular those containing chloroaluminate ions; these ions have also been confirmed responsible by SEM for galvanic corrosion of Al metal causing cracks and craters in the surface. The thin film Al-oxide layer is dissolved but more interestingly is redeposited back onto the surface as Al_2O_3 [30]. The native oxide film across an Al electrode suppresses any dendrite growth avoiding associated cell degradation. After 10,000 cycles, cross sections of SEM revealed increased porosity within the Al surface forming dendrites, all coated by a thin film across the top [45]. XPS spectra revealed Al 2p peaks corresponded to that of Al_2O_3 derived from the initial oxide film. Cyclic voltammograms (CV) were run using two separate Al electrodes: one with a surface oxide layer and one without. After 10,000 cycles, the oxide covered Al electrode revealed etching upon the electrolyte facing side while the Al electrode without the protective oxide layer was all but disintegrated. After only 1,000 cycles, SEM revealed dendrite formation on the oxide-less Al electrode. Any protective thin film therefore originates from the native thin oxide film of aluminium.

2.3.2 Carbonaceous materials

Carbon has been a widely investigated electrode material choice for electrochemistry for decades primarily due to its inert nature making for a leading electrode material for exposure to corrosive chloride electrolytes [46], as well as existing in many different structural and morphological forms such as highly ordered graphite or more amorphous forms like glassy carbon.

The highly ordered structure of graphite allows for intercalation of ions into the van der Waals gaps between the graphite layers and therefore expansion of those layers to accommodate such large ions.

The way that ions intercalate into graphite has been investigated, as calculation and experiments haven't come to an agreement. Gao et al reviewed and discussed the many views behind the principles of intercalation of chloroaluminate ions, whether they exist in a planar geometry that slides in between graphite layers or in a tetrahedral structure, whether these ions intercalate

individually per layer or are double stacked [47]. From computational modelling Gao finds that the most favoured geometry is tetrahedral requiring less energy than planar, in agreement with Bhauriyal et al. [48] though an added observation is made that the van der Waals forces compress the intercalated ion slightly distorting the molecular bond length and angles. By way of computational tomography (CT), SAXS and XRD, it was observed that upon the insertion of $AlCl_4^-$ into the graphite layers, the expansion causes a large decrease in the porosity and pore size of the material [49]. This is believed to be the reason for the initial irreversibility of the first cycle capacity exhibited with pyrolytic graphite as the crystal structure traps $AlCl_4^-$ to relieve stress caused by the expansion.

With regards to intercalation and the number of inserted ions stacked per graphite layer, modelling indicates that the ions insert in a single layer as opposed to doubly stacked due to the more stable energy requirements of a single layer and due to calculated theoretical capacity of a single layer corresponding to experimental data of 60-70 $mAhg^{-1}$ [47].

The use of exfoliated graphite in LIBs has achieved capacities of 540 $mAhg^{-1}$ at 50 mAg^{-1} up to 1264 $mAhg^{-1}$ at 100 mAg^{-1} [50, 51] with the former decreasing to a stable 290 $mAhg^{-1}$ after 20 cycles at 54% efficiency, and the latter decreasing to 1144 $mAhg^{-1}$ after 5 cycles. Such a large capacity was due to the enhanced surface area caused by exfoliation of the graphite [51].

The performance of graphite and activated carbon are constantly being enhanced and often depend on the materials used in conjunction with them. Commercially available carbon materials are a quick substitute for lab-fabricated materials when the investigation does not call for it. Purchased materials such as bulk graphite, expanded graphite, and pyrolytic graphite have been recently studied. A bulk graphite cathode prepared with an alginate sodium binding agent in a lithium cell displays high cycling stability of over 2000 cycles at a rate of 20C, where a c-rate indicates the speed of charge, 1C equating to 1 hour and 20C being 20 times faster. This provides an average coulombic efficiency of 98.4% [52]; an aluminium cell using a second prepared bulk graphite cathode also achieved a high average coulombic efficiency of around 97-98% when cycled at 20C. This implies that AIBs can achieve similar efficiencies to LIBs albeit at lower capacities perhaps due to the intercalation ability of the Li^+ ions in the LIB compared to that of $AlCl_4^-$ in Al-ion battery.

The intercalation of $AlCl_4^-$ into pyrolytic graphite, as previously mentioned, can exhibit some irreversibility due to the contraction of graphite layer around the $AlCl_4^-$ ions [49]. A Panasonic pyrolytic graphite cathode displayed similar irreversibility with an initial coulombic efficiency of

only 70% [53]. XRD of the discharged electrode showed structural changes after deintercalation of chloroaluminate ions when compared to a pristine electrode, while XPS detected the presence of Al and Cl_2 in the fully discharged electrode indicating that some of the $AlCl_4^-$ ions had not been deintercalated. It is also theorised that there is initial co-intercalation of the $Emim^+$ cations into the PG which add to the irreversible change in graphite structure [53]. This initial irreversibility appeared to benefit the cell as the specific capacity of the Panasonic graphite cell after 500 cycles at 100 mAg^{-1} was around 65 $mAhg^{-1}$, in keeping with other graphite studies, after an initial capacity of 45 $mAhg^{-1}$ at 100 mAg^{-1}. However, reports of $AlCl_4^-$ stage 4 intercalation at capacities around 60 $mAhg^{-1}$ led Dong et al. to theorise and verify using SEM that additional capacity sufficiently above the normal 60 $mAhg^{-1}$ for graphite is due to deposition of $AlCl_4^-$ onto the surface [31], though a commercial expanded graphite was used for this investigation and cannot be applied across all graphitic materials.

Activated carbon, which is believed to gain capacity through the double electric layer, achieved a higher specific capacity than flake graphite of 117 $mAhg^{-1}$ to 59 $mAhg^{-1}$ respectively at 75 mAg^{-1} [54]. Initial specific capacities for carbon are higher than those for graphite albeit at the cost of a lower coulombic efficiency at 60% compared to 90% for graphite. However, this is short lived as the capacity of carbon decreases below that of graphite after the 8^{th} cycle.

The specific capacity can be increased slightly by replacing the aluminium foil electrode in an AIB with a second graphite electrode plating with the same mechanism as an aluminium electrode, maintaining a potential window of 2.2 V [55]; specific discharge capacities of 76 $mAhg^{-1}$ at 200 mAg^{-1} were reported along with a coulombic efficiency stable around 98% over 1000 cycles at 500 mAg^{-1}. This is directly compared within the same study with a standard Al foil anode cell achieving lower capacities between 60-70 $mAhg^{-1}$ at 200 $mAhg^{-1}$. This disparity is attributed to the interaction of the acidic electrolyte corroding the aluminium metal foil. SEM indicated intercalation from structural changes in the graphite cathode and lack thereof in the graphite anode; a dual graphite electrode battery utilises the deposition of metallic aluminium on the graphite anode surface during charging while $AlCl_4^-$ intercalates into the graphite cathode.

An ultrathin graphitic foam (UGF) in a $LiPF_6$ organic carbonate electrolyte cell reported a conductivity of 1.3 $x10^5$ Scm^{-1} though the surface area was not reported. This UGF cathode remained stable when cycled between 2-5 V vs Li/Li^+ achieving specific capacities around 160 $mAhg^{-1}$ at 16 mAg^{-1} down to 36 $mAhg^{-1}$ at 2560 mAg^{-1} [56]. Compare this to a 3D graphitic foam

in an aluminium chloride cell, fabricated using pyrolytic graphite fully charged by intercalating chloroaluminate ions for 40 hours. The resulting expanded graphite underwent rapid thermal heating followed by use as a cathode in hydrogen evolution reactions [57]. The final form of the graphite had a BET surface area of 75 m^2g^{-1} providing a specific capacity of 60 $mAhg^{-1}$ and a coulombic efficiency of around 100% at 12 Ag^{-1} over 4000 cycles proving to be incredibly stable. The efficacy of the super-fast charging is shown after charging at 12 Ag^{-1}, when discharging at a slower rate of 2 Ag^{-1} gave a near 100% coulombic efficiency. However, charging and discharging at such high current densities results in a pseudo-capacitive cell with a quicker linear discharge and a low average voltage, when compared to slower intercalation providing higher capacities.

Table 2-2 Comparison of Carbon cathode materials

Working electrode	Specific Capacity ($mAhg^{-1}$)	Specific Energy ($Whkg^{-1}$)	Operating/Midpoint Voltage (V)	Reference
Activated Carbon	117	293	2.5 vs Al/Al^{3+}	[54]
Flake Graphite	59	148	2.5 vs Al/Al^{3+}	
Exfoliated Graphite	540	-	-	[50]
Panasonic Pyrolytic	65	156	0.4-2.4 vs Al/Al^{3+}	[53]
Commercial Bulk Graphite	75	334	3-5 vs Li/Li^+	[52]
Ultrathin Graphitic Foam	160	800	2-5 vs Li/Li^+	[56]
3D Graphitic Foam	60	148	0-2.46 vs Al/Al^{3+}	[57]

2.3.3 Current Collectors

The electrode doesn't always consist solely of one material. The active electrode material is often backed onto a current collector made of a different material. A titanium nitrate (TiN) sputtered stainless steel current collector was used to mount graphite, providing stability against a highly

acidic chloroaluminate electrolyte with capacities above 120 $mAhg^{-1}$ at 10 Ag^{-1} with an efficiency of 99.5% [58]. Chromium nitrate (Cr_2N) prepared in the same manner displayed capacities of 130 $mAhg^{-1}$ at 500 mAg^{-1}. In another $AlCl_3$ cell, natural graphite mounted onto a nickel current collector provided a stable specific capacity of 100 $mAhg^{-1}$ at 198 mAg^{-1} [59].

Graphite can also be used as the current collector where it can also contribute to intercalation; nickel phosphide nanosheets supported on reduced graphene oxide (rGO) achieved a much larger initial capacity of 275 $mAhg^{-1}$ at 100 mAg^{-1} though this reduced to 73 $mAhg^{-1}$ after 500 cycles with 93.5% coulombic efficiency [60]. The stable capacity is comparable to graphite literature however the initial capacity spike appears to be due to side reactions that degrade the system. Corrosive reactions affect current collectors when they are not suitable to the electrolyte environment; the acidic nature of $AlCl_3$ electrolytes cause corrosion on stainless steel among other materials. Tungsten's high oxidative stability makes it a good candidate for a current collector when paired with a polypyrene cathode material, a capacity of around 70 $mAhg^{-1}$ at 200 mAg^{-1} is reported [61]. Molybdenum current collectors have been shown to have good stability; Raman and XPS spectra of a chloroaluminate electrolyte showed no Mo peaks indicating that the current collector did not take part in any reactions whilst the cell was cycled [27].

2.3.4 Metal oxides

Looking at the major metal oxide cathode materials that have been used in lithium-ion batteries as well as aluminium ion batteries may indicate that certain materials have an innate battery excellence or allow us to see what types of metal oxides work with which ion type and why.

For LIBs, $LiCoO_2$ is a commonly used cathode material with a specific capacity of around 150 $mAhg^{-1}$ and a voltage of 3.9 V vs Li/Li^+. $LiFePO_4$ provides a slightly higher capacity at 160 $mAhg^{-1}$ but a slightly lower voltage of 3.45 V vs Li/Li^+. Achieving both a relatively high capacity and voltage is $LiNiMnCoO_2$ which has a capacity of 180 $mAhg^1$ at a voltage of around 3.8 V vs Li/Li^+, though these three cathodes were tested at a slow C/20 rate [62]. $LiNi_{0.8}Co_{0.2-x}Al_xO_2$ is a slightly more complex Al-doped material operating at 4 V offering discharge capacities of around 175 $mAhg^{-1}$ though with a coulombic efficiency of just over 80% [63]. There is potential for hybrid lithium-aluminium cells using an aluminium metal anode and a lithium metal oxide cathode; in an $EmimCl\text{-}AlCl_3$/ $LiAlCl_4$ electrolyte, a $LiFePO_4$ cathode achieved a specific capacity of 71 $mAhg^{-1}$ with lithium plating on the Al anode [64]. Even higher capacities can be achieved for LIBs using shale – Co_3O_4, a spinel material that has attained a capacity of 1045 $mAhg^{-1}$ at 200 mAg^{-1} after 100

cycles [65]. Another spinel Fe_3O_4 powder doesn't perform nearly as well delivering 170 $mAhg^{-1}$ at 20 mAg^{-1} over 30 cycles [66]. The spinel structure allowed for the insertion of lithium ions but might not support intercalation of the larger chloroaluminate ions.

Using Co_3O_4 for AIBs yields a specific capacity of 195 $mAhg^{-1}$ at 200 mAg^{-1} decreasing to 122 $mAhg^{-1}$ after 100 cycles with a coulombic efficiency of around 80-90% [67]. This is far below what was reported for LIBs due to the large size difference between the intercalants. Liu J. et al. also reports the mechanism for intercalation involves the intercalation of Al^{3+} cations as opposed to $AlCl_4^-$ anions, confirmed with XRD. The constant intercalation and de-intercalation of Al^{3+} cause structural changes to the cobalt oxide as well as trapped aluminium that accounts for the loss in capacity. The intercalation of trivalent aluminium has been reported before albeit in an aqueous $AlCl_3$ system. TiO_2 nanotube arrays on a titanium foil substrate were used as a cathode material, allowing for Al^{3+} insertion into the array before the potential for the hydrogen evolution reaction was reached [12]. The insertion of the aluminium is reasoned by Liu S. et al. to be due to the small steric effect of the aluminium ions; due to the increased nucleus' charge, along with more electrons held within few shells, the radius of aluminium is smaller than the lithium, sodium, or magnesium counterparts.

AIB research has looked into the use of Mn_2O_4 cathode which provides a theoretical capacity and gravimetric energy density of 400 $mAhg^{-1}$ and 1060 $Whkg^{-1}$ respectively based on a cell voltage of 2.65 V which is higher than the theoretical values for a LIB using Mn_2O_4 reported at 406 $Whkg^{-1}$[8]. However, the theoretical capacity is based on the notion that the trivalent Al^{3+} will be intercalating into the positive electrode allowing the transfer of 3 electrons. When using an $AlCl_3$ based electrolyte, the monovalent $AlCl_4^-$ ion is intercalated instead, thus limiting the actual capacity and energy density. A LIB using a $LiMn_2O_4$ cathode operating between 3.3-4.4 V vs Li/Li^+ displayed a specific capacity of 85 $mAhg^{-1}$ at 1 $mAcm^{-2}$ after 300 cycles [68]. The performance of manganese oxides is good when it comes to LIBs, however the large theoretical performance in AIBs makes it a promising electrode material.

MoO_2 on a Ni foam was tested as a potential cathode in AIBs however transfer of the MoO_2 to the separator due to the corrosivity of the chloroaluminate electrolyte lead to an inevitable decline in performance: the capacity decreased over 100 cycles from around 90 $mAhg^{-1}$ to 25 $mAhg^{-1}$ [69]. A vanadium metal electrode similarly experienced a fast decline in performance and the metal, exposed to chloroaluminate ions, underwent an irreversible oxidation with each cycle [70].

Switching to a solid VCl_3 composite electrode, initial capacities of 76 $mAhg^{-1}$ were seen at 3.33 mAg^{-1} which was far below the theoretical capacity of 170 $mAhg^{-1}$. The capacity also quickly degrades due to the dissolution of the solid VCl_3 into the acidic chloroaluminate electrolyte.

WO_3 has shown promise in AIBs producing a specific capacity of 70 $mAhg^{-1}$ at 100 mAg^{-1} [71]. The use of VO_2 by Wang et al. achieved a capacity of 116 $mAhg^{-1}$ at 50 mAg^{-1} after 100 cycles and an energy density of 48 $Whkg^{-1}$ [72]. The cell only operated across a range of less than 0.9 V to test for the redox potentials, so a more thorough study is needed to ensure the electrode materials do not limit the voltage window further than the electrolyte. Wang et al. noted that V_4O_8 could theoretically produce a capacity of up to 485 $mAhg^{-1}$ if two Al ions could be packed into segments of the vanadium structure.

V_2O_5 composited with carbon attained a capacity of around 50-60 $mAhg^{-1}$ at a C/10 rate in an $AlCl_3$-based electrolyte with a theoretical capacity of 442 $mAhg^{-1}$ [73]. The lack of imidazolium chloride from the electrolyte may contribute to the Al^{3+} insertion into the cathode, as chloroaluminate ions are not formed without the presence of available Cl^- ions. The intercalation of Al^{3+} into V_2O_5 occurs at 1.6 V vs Al/Al^{3+} which limits the cell voltage compared to other positive electrodes.

A cathode made of Vanadium oxychloride (VOCl) attained energy densities of up to 189 $Whkg^{-1}$ and a specific capacity of 113 $mAhg^{-1}$ at 522 mAg^{-1} after 100 cycles operating in a small voltage window between 1-2.8 V vs Li/Li^+ [21]. A similar cell featured Iron oxychloride (FeOCl), though achieved higher capacities of 162 $mAhg^{-1}$ after 30 cycles but at a much lower current density of 10 mAg^{-1} with a potential window of 1.9 V between 1.6-3.5 V [74].

*Table 2-3 - Comparison of metal oxide cathode materials; (**T**) stands for theoretical values*

Working electrode	Specific Capacity ($mAhg^{-1}$)	Specific Energy ($Whkg^{-1}$)	Operating/Midpoint Voltage (V)	Reference
S-Co_3O_4	1045	940 – 1150	0.9-1.1 vs Li/Li^+	[65]
$LiMn_2O_4$	85	374	4.4 vs Li/Li^+	[68]
$LiCoO_2$	150	200	3.9 vs Li/Li^+	[62]
$LiFePO_4$	160	552	3.45 vs Li/Li^+	
$LiNiMnCoO_2$	180	220	3.8 vs Li/Li^+	

$LiNi_{0.8}Co_{0.2-x}Al_xO_2$	175	700	4 vs Li/Li^+	[63]
Fe_3O_4	170	255 - 290	1.5-1.7 vs Li/Li^+	[66]
FeOCl	60	114 - 156	1.9-2.6 (vs Li/Li^+)	[74]
VOCl	113	189	1.6 (vs Li/Li^+)	[21]
Co_3O_4	122	73 - 110	0.6-0.9 vs Al/Al^{3+}	[67]
MoO_2@Ni	90	171	1.9 vs Al/Al^{3+}	[69]
Mn_2O_4	400 (**T**)	1060 (**T**)	2.65 (**T**) vs Al/Al^{3+}	[8]
MnO_2	332 (**T**)	255 (**T**)	0.8 vs Al/Al^{3+}	[75]
WO_3	70	-	-	[71]
VCl_3	76	177 (**T**)	0.9 vs Al/Al^{3+}	[70]
VO_2	116	48	0.5 vs Al/Al^{3+}	[33]
V_4O_8	485 (**T**)	-	-	
V_2O_5/C	~50-60	-	-	[73]

2.4 Summary

From the literature above and Table 1.2, it can be surmised that a carbonaceous cathode provides the platform for reliable performance for the cell it is housed, regardless of the electrolyte chosen. The variations of carbon with metal oxides as well as more recently reported graphitic electrodes make them a prime candidate for investigation, not to mention the reduced cost of carbon compared to more expensive electrode materials. Reports show that graphite electrodes provide on average, a capacity of around 60-75 $mAhg^{-1}$ which is hindered by the materials porosity, affecting de-intercalation of chloroaluminate ions. With such a wide array of graphite types along with electrolyte and cell arrangement, it would be prudent to compare different carbonaceous materials in the same cell setup to investigate the performance changes as well as intercalation effects by way of different characterisation methods. Activated carbon performs well with a large capacity of 117 $mAhg^{-1}$, as does ultra-graphitic foam at 160 $mAhg^{-1}$ and exfoliated graphite at 540 $mAhg^{-1}$. The addition of different metal oxides to the carbon electrodes would also allow for increased theoretical capacities and performance that is more promising. Testing different carbons both with and without additional elements will give more insight into the effects of double layer capacitance versus intercalation behaviour of certain materials.

Specific capacity is reported generously across literature but not the method of calculation. The theoretical capacity of Mn_2O_4 excludes how the calculation was carried out which confuses or could misleads the reader. Certain specific capacities are calculated taking into account just the intercalated ions, others including the electrode active material with which the ions interact. This can inflate or deflate the capacity value. This is something with which research should focus on and be open about when comparing results.

From Table 1.3, the most interesting metal oxides appear to be the shale cobalt oxide with such a large specific capacity, however the average voltage of the cell is very low for a lithium-ion battery. If used in an aluminium setting, the reduction potentials of -0.43 V to -0.23 V vs Al/Al^{3+} would be too low. This would be expected to change with respect to the electrolyte used as cobalt oxide nanosphere rods reduce between 0.6-0.9 V vs Al/Al^{3+} in an $AlCl_3$ setting. Molybdenum oxide on nickel provides the greatest voltage in an AIB at 1.9 V, however the initial capacity is comparatively low which only proceeds to decay due to corrosion. The stability of manganese-based electrodes as well as the high theoretical capacity and energy densities make them a promising material to research along with cobalt oxide and vanadium(V) oxide due to their high capacities. The lower voltage is an inevitably common by-product of AIBs due to chlorine evolution. Graphite electrodes as discussed previously have higher redox potentials due to the intercalation redox around 1.8 V vs Al/Al^{3+} and so make for higher voltage batteries; different carbonaceous materials will also be investigated, but potentially composite electrodes will be the key to unlocking the optimum cell performance. Testing such a large array of materials using the same methodology will also make it easier for direct comparison of the electrode materials to conclude which performs better, as well as making it easier for future researchers regarding reviewing literature on the subject.

One issue that was evident whilst reviewing literature on electrode materials was the intended meaning behind the cell voltage, whether the value given was the voltage plateau at the ohmic loss region of the electrode discharge profile or an optimum operating voltage window. For most cells, a singular redox potential for the cell represents a midpoint in the discharge. However, this is based off the notion that the kinetics of intercalation are fast, and voltage drops slowly while the discharge reaction occurs such as in Li-ion battery Figure 2-1a. This is not always the case as rapid voltage decay can be observed on discharge such as in Figure 2-1b for hybrid dual ion Li^+ and PF_6^- or for Al-ion battery where the midpoint cell voltage is not clear, or perhaps the discharge is a multi-step process in which case there would be a disparity with regards to the midpoint.

As for electrolytes, non-aqueous IL electrolytes have the advantage of being non-flammable and customisable. ChCl/EG as well as $PP_{14}Cl$ could be studied to look at transferring chloride ions as they both have large conductivities depending on the solvent used, and in the case of $PP_{14}Cl$ a large electrochemical potential window of 3.2 V. The stability of electrolytes differs depending on the cell setup and so actively observing the electrochemical potential window of a cell across different cell setups would unite previously fragmented areas of study.

As for solid and gel polymer electrolytes, the large voltage windows are very impressive however they operate at large temperatures to achieve good conductivities. The brittle nature of solid electrolytes is not conducive to battery investigations and the GPEs reviewed here require increased levels of complexity in order to facilitate ideal mechanical properties such as increased ductility. Therefore, Ionic liquids are a more suitable area of study. Investigations into aluminium ion electrolyte performance revolves around the chloroaluminate ions, those created using $AlCl_3$ salt. The differences in performance of the accompanying cation are not a major contributing factor when looking into anion intercalation-based performance. However, the use of TFSI cation in order to avoid Cl^- oxidation potentially expanding the electrochemical window is a promising avenue for investigation. Given this and the well-reported stability of imidazolium cations with $AlCl_3$ in a reliable 2.5 V window, Emim-Cl will be used as the main cationic salt to focus on with the possibility of an investigation into a TFSI-based electrolyte.

Much of the literature reviewed here looks at the whole cell and it can be difficult to separate the contributions to efficiency and capacity, of the electrolyte or electrode material from the overall cell performance, as the two performance indicators are inherently linked. This needs to be investigated and attempts need to be made to research them separately using three electrode cell measurement for better understanding and comparison.

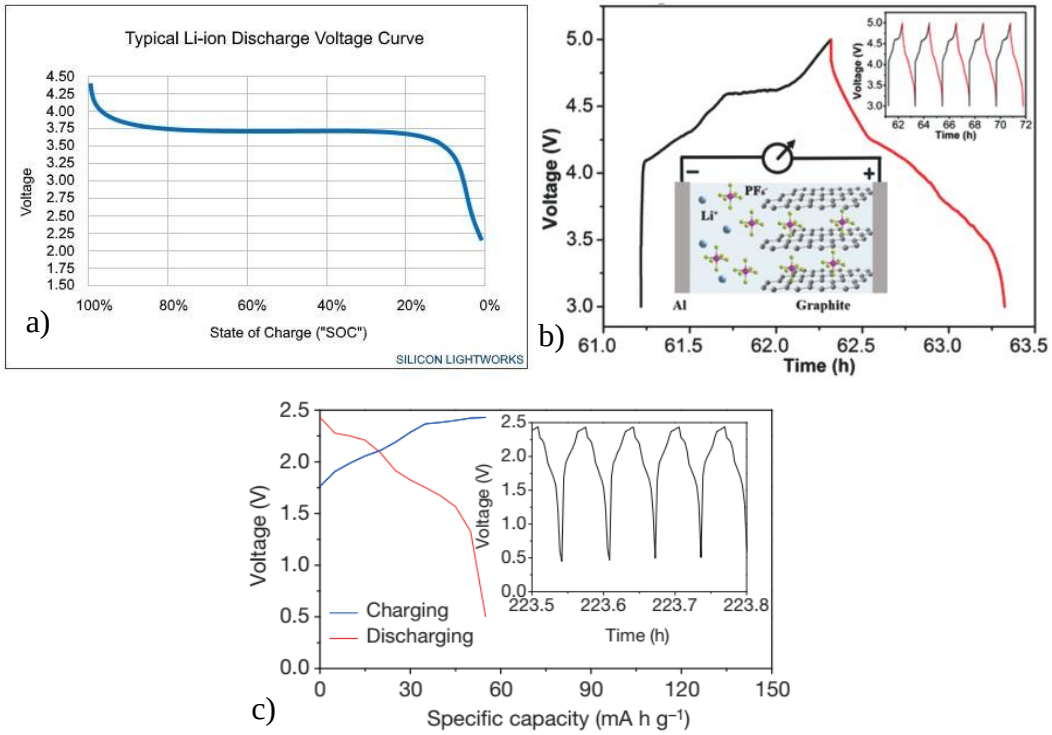

Figure 2-1- a) Typical discharge curve of lithium-ion battery displaying steady ohmic losses [76] b) atypical Li dual-ion battery displaying non-uniform charge (black) and discharge (red) curves as real world conditions differ from the ideal with an inset displaying multiple cycles [77] c) atypical Al-ion battery charge (blue) and discharge (red) curves displaying the non-uniformity of cell reaction rates with multiple cycles inset [24]

Chapter 3. Experimental Methodology

3.1 Anode

Annealed aluminium metal foil (Sigma Aldrich) is used as the anode. 18mm discs are cut from a 0.1mm thick metal sheet using an El-Cell precision cutter. Exposure to the open atmosphere causes the surface of the aluminium to oxidise, and so inside of an argon glove box before cell assembly, the aluminium discs are sanded down to remove the surface layer to allow for adequate conductivity through the anode, and aid aluminium dissolution into the electrolyte. Sanding down the aluminium also benefits the interaction of the electrode and electrolyte by increasing the surface area, enhancing the surface coverage of the electrolyte. Tests involving an open-top glass cell within the glove box use strips of aluminium or platinum foil.

3.2 Cathode Fabrication

Cathodes were fabricated using the selected catalyst powder, which was mounted onto a backing substrate. Preliminary testing revealed that a carbon paper substrate contributed to the performance of the cell, invalidating the results. The use of vitreous carbon, also known as glassy carbon, as the substrate and current collector for powdered cathodes was implemented to avoid additional intercalation of ions that would otherwise affect the results. Glassy carbon is very resistant and incredibly stable making it an ideal choice for use with acidic electrolytes.

A catalyst ink solution was mixed using the chosen powdered material, and an appropriate binding agent for adequate adhesion to the substrate. The binder used throughout was polyvinylidene fluoride (PVDF) (Alfa Aesar). To apply the loading evenly across the backing material, the volume of catalyst ink prepared was calculated for a loading of 1 $mgcm^{-2}$. The loading is multiplied by the electrode area, giving a total weight needed to coat the surface. Due to preparation of multiple electrodes and undesired losses of the ink, a bulk factor of was taken into consideration when preparing the required volume of catalyst ink.

Catalyst materials used include Ketjen black carbon powder, Co_3O_4 from Sigma Aldrich, $CoAl_2O_4$ and Al_3Mn from Alfa Aesar, and MnO_2 and WO_3 from U.S. Nanomaterials. An exfoliated graphite sheet, rGO powder, $NiCo_2O_4$ and $LiNi_{0.8}Mn_{0.1}C_{0.1}O_2$ were non-commercially sourced.

For the PVDF binding agent, 10% weight of that of the total catalyst was used. Too much binder would increase the resistance within the cathode and too little wouldn’t see the catalyst bind effectively to the substrate. To mix the catalyst and the binding agent, and to load them onto the

substrate, they were first suspended in separate solvents: isopropyl alcohol (IPA) for the catalyst and tetrahydrofuran (THF) for the binder. A stronger solvent than IPA was required to create a PVDF suspension. Both suspensions were sonicated for 30 minutes and 15 minutes respectively before being mixed and sonicated for a further 30 minutes. 0.1 ml of IPA was used per 1 mg of catalyst material, with 0.33 ml of THF used per 1 mg of PVDF.

An example set of calculations for the required amounts of materials are as follows:

Loading $= 1\ mgcm^{-2}$

Area of substrate $= 1\ cm^2$

Required catalyst material $= 1\ mgcm^{-2} \times 1\ cm^2 = 1\ mg$

Included Bulk Factor $= 10 \times 1\ mg = \mathbf{10\ mg}$

PVDF needed $= 10\ mg \times 10\% = \mathbf{1\ mg}$

IPA needed $= 0.1\ ml\ per\ 1\ mg \therefore 0.1\ ml \times 10 = \mathbf{1\ ml}$

THF needed $= 0.33\ ml \times 1\ mg = \mathbf{0.33\ ml}$

The best method for coating the glassy carbon with the catalyst ink was found to be drop casting: the act of using a fine syringe to eject droplets of the catalyst ink onto the surface of the substrate and allow it to dry. The electrode would then be left to dry under an infrared lamp to speed up the evaporation of the solvents at a speed that would not result in cracking of the resultant cathode layer.

3.3 Electrolyte Preparation

The electrolyte being investigated is 1-ethyl-3-methylimidazolium chloride/ Aluminium chloride. Differing ratios were used, a ratio of 1:1 as well as a 1:1.3 ratio. 1:1 Emic/ $AlCl_3$ of 99.999% purity (Sigma Aldrich) is used with no additions for the 1:1 experiments, and with an excess of $AlCl_3$ 99.999% (Sigma Aldrich) added for the higher 1:1.3 ratio experiments. The $AlCl_3$ is added slowly whilst being stirred to avoid any potentially violent emissions due to the highly exothermic nature of the imidazolium chloride and aluminium chloride reaction. The exothermic effect is lessened as the starting electrolyte already exists at a 1:1 ratio, meaning that most of the highly reactive effects have already been played out.

Once mixed inside of an argon-filled glovebox, the resulting solution was then placed into a pressurised vessel and vacuumed at 100^{o}C for 42 hours to ensure minimum water content that

would otherwise interfere with the performance of the cell. Discolouration occurred after heating as the solution changed from pale yellow to a darker brown.

Molar calculations were based on mass and molar mass of the imidazolium chloride. Increasing the number of moles of $AlCl_3$ by 30% and multiplying by the molar mass of $AlCl_3$ gives the required weight addition. Calculations for electrolyte preparation can be found in Appendix 1.

$$m_{Emic} \div M_{Emic/AlCl_3} = mols_{Emic/AlCl_3}$$

$$\left(mols_{AlCl_3} \times 30\%\right) \times M_{AlCl_3} = m_{AlCl_3}$$

3.4 Cell Assembly

3.4.1 Electrochemical Cell Design

Based off the El-Cell Ref design, a test cell as seen in Figure 3-1 was fabricated to overcome experimental issues discussed below. This new design incorporated an entirely sealed inner cell, with a built-in reference wire, encompassed by a larger stainless-steel cell casing.

Figure 3-1 – Assembled 3-electrode electrochemical cell fabricated in-house, stainless steel shell, stainless steel reference pin connector encased in PEEK screwed into top, all holes sized for 2 mm banana plugs

The PEEK plastic inner sleeve permanently houses an aluminium reference wire which when assembled, sits in contact with the electrolyte-soaked glass fibre separator. The outer side of the wire touches a stainless-steel reference pin which screws into the top of the steel outer shell. Two glassy carbon electrodes with O-rings slot into place, sealing the electrolyte in between them both. Conductive compression springs act upon both electrodes to complete the circuit and to ensure adequate contact of the electrodes. A polyethylene washer in the shell and an O-ring on the reference pin act as a secondary seal for an air-tight cell.

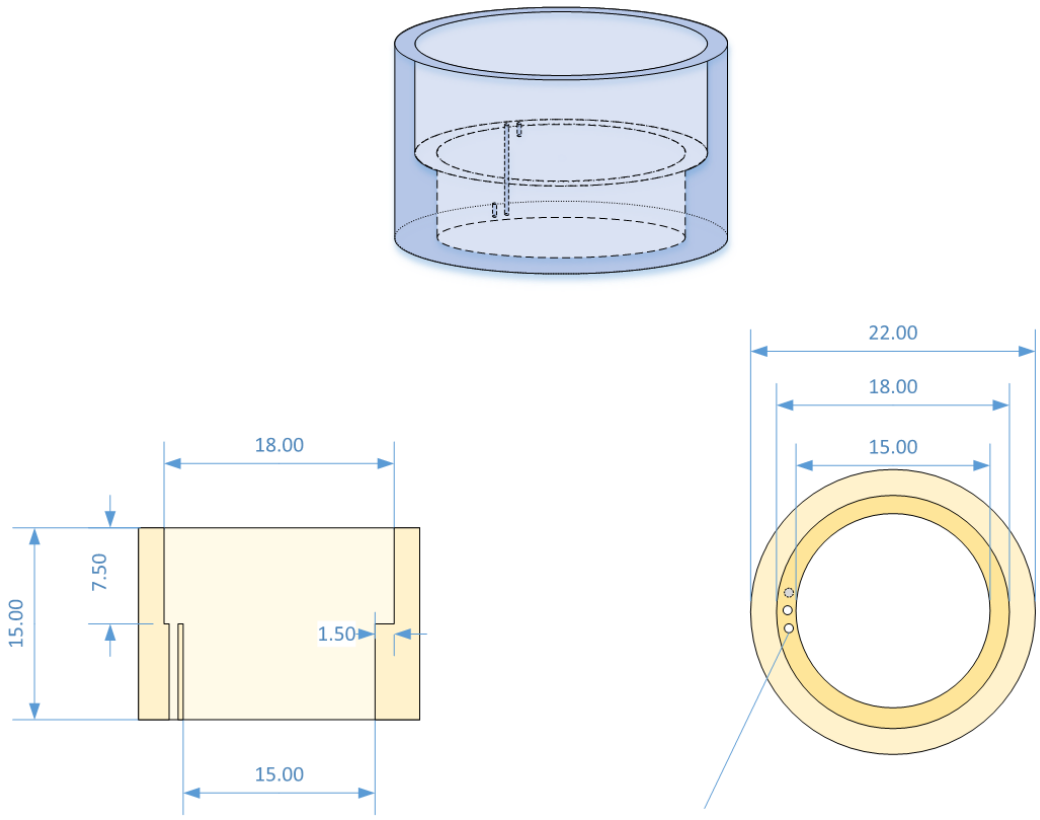

Figure 3-2 – 3D, profile, and top view of PEEK plastic inner sleeve. Two inner diameters accommodate different electrode sizes with a slot for a reference wire to be folded back on itself into smaller adjacent holes and secured

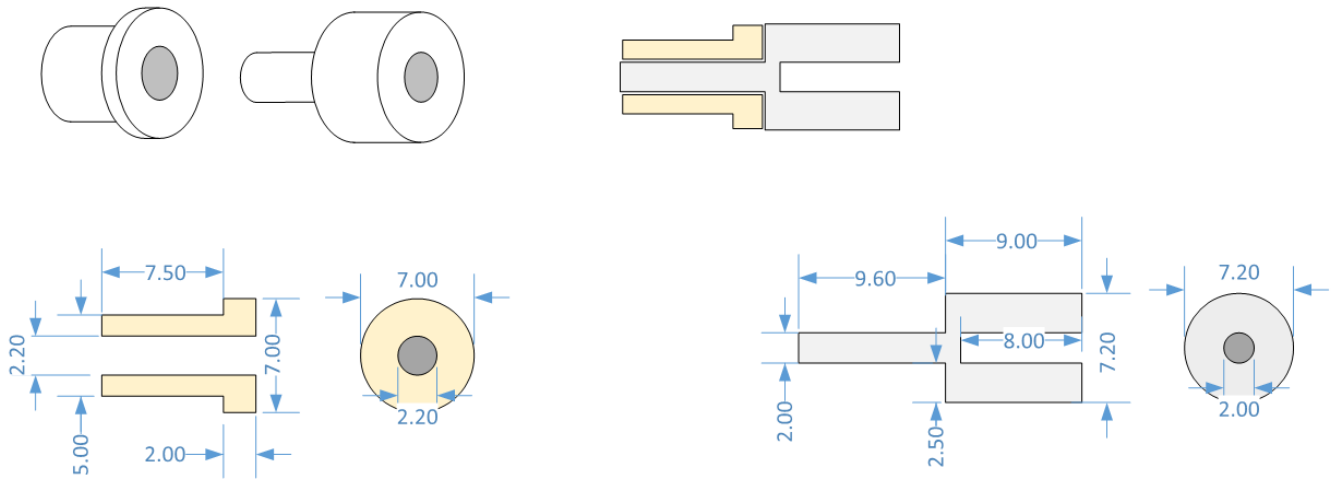

Figure 3-3 – 3D, profile, and top views of PEEK covered stainless steel reference pin with 2 mm hole drilled for banana plug

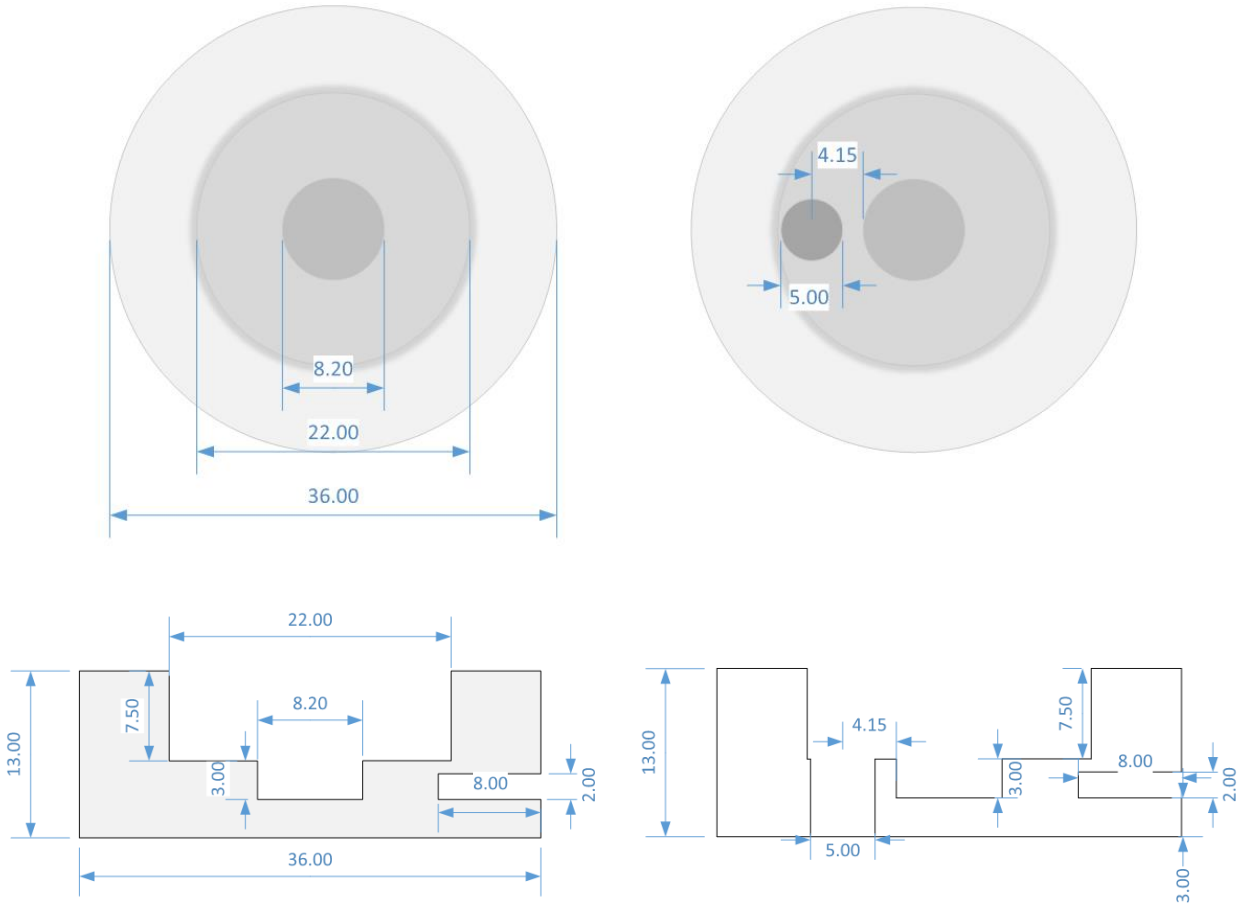

Figure 3-4 – Top and profile views of lower (left) and upper (right) stainless steel shell components for electrochemical test cell

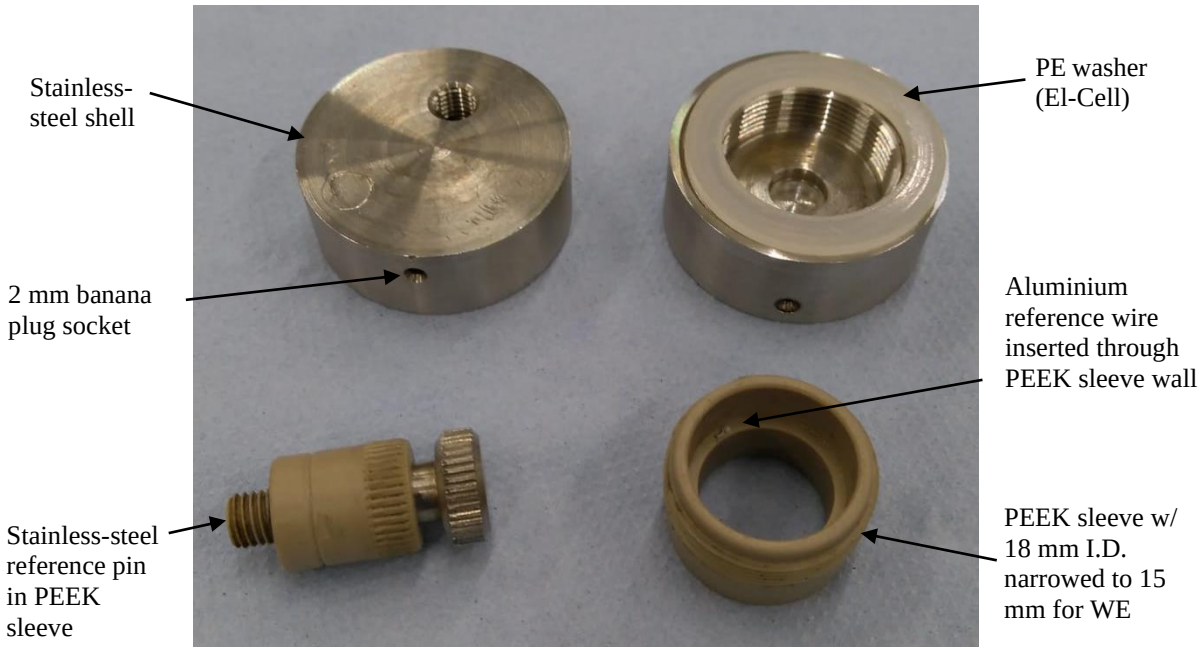

Figure 3-5 - Electrochemical cell breakdown showing the upper stainless-steel shell (top left), lower stainless-steel shell (top right), stainless-steel and PEEK reference pin (bottom left), inner PEEK sleeve with inserted Al reference wire (bottom right)

3.4.2 Assembly

The narrower working electrode is inserted into the PEEK sleeve and pushed into place followed by the placement of an 18 mm diameter, 0.65 mm thick glass fibre separator (El-Cell). 150 μl of electrolyte is added to effectively wet the separator. The sanded aluminium anode is placed sanded-side down into the sleeve followed by the larger glassy carbon current collector which is pushed into place. The self-contained cell can then be placed into the outer shell paying close attention to align the PEEK sleeve aluminium reference wire with the reference pin, as well as align the compression springs with their respective shell half.

Half-cell testing took place in a small open-top glass beaker with excess electrolyte up to 1 mL to utilise the accuracy of a leakless miniature Ag/AgCl reference electrode with a filling electrolyte of 3.4 mol/L KCl. This modified setup could help confirm the accuracy of the Al wire reference electrode as well as remove the electrolyte as a limiting factor in the half-cell test results.

3.4.3 Experimental Challenges

When using an El-Cell Ref test cell, experimental issues arose. The reference wire was at a fixed height which meant that compression of the cell via a steel plunger would often compress too much allowing the working electrode to contact the reference wire and short the cell.

Electrolyte issues occurred due to the use of an acidic electrolyte. The corrosivity of the Cl-based electrolyte caused corrosion of the steel components due to electrolyte leaking around both electrodes. This meant that the steel plunger and current collector was corroding and needed to be replaced. A titanium plunger suffered the same fate, as did a gold leaf disc used as a barrier between the plunger and the rear of the cathode. The corrosion was an unforeseen side reaction that was contributing to the data gained from the experiment and therefore deemed invalid. A graphite plunger was next used which did not corrode, however experimental data indicated that ions were intercalating into the graphite plunger invalidating the results once again. A new cell was designed and built, using glassy carbon current collectors were found to negate these issues.

An unknown impurity emerged within the electrolyte demonstrating a highly reversible, stable redox. To ensure that the reference is accurate as well as to confirm the observed oxidation reaction in section 4.2.1.1 is not caused by potential drift, the internal reference ferrocene is added to the electrolyte. It is noted that literature shows an instability of ferrocene in chloride-based electrolytes [78] with results indicating that the redox potential negatively shifts to <0.1 V vs Ag/AgCl demonstrating irreversible behaviour. A large oxidation at around 0.5 V vs Ag/AgCl was seen,

resulting in a small reduction. This is the oxidation of ferrocene into ferrocenium, but the diffusion away from the electrode results in the small reduction peak. The half wave potential of ferrocene is 0.45 V confirming the AgCl reference accuracy. Since the peaks are not present when using a stock electrolyte, it is likely an impurity from the Emic salt or propylene carbonate solvent. Some such impurities in the imidazolium chloride salt could be small quantities of the precursor 1-methylimidazole that did not react to form 1-ethyl-3-methylimidazolium chloride. However, the oxidation potential of 1-methylimidazole peaks at around 1 V vs Ag/Ag^{+} with no reduction [79] meaning that this unknown redox cannot be 1-methylimidazole. Since the impurity is not a precursor or degradation product of the electrolyte, its identity is not relevant to this study and can be disregarded.

3.5 Electrochemical Measurements

An Autolab potentiostat/galvanostat was used as the potential/current control source. Counter electrode and reference wires were connected to the base of the cell while the working sense and working electrode were connected to the top of the cell. The additional wires from the PX1000 module were connected to the reference and working electrode in order to measure the cathode potential.

Figure 3-6 shows a step by step procedure used for cell cycling. This begins with a frequency response analysis (FRA) that was run on the cell to check that the cell resistance was at an appropriate value, ensuring everything was working correctly. Discharging of the cell was first carried out to start cycling from the lower potential limit of 0.2 V vs $Al/AlCl_4^-$. The initial applied current varied depending on the material used and the initial test results, with the current later being altered in an attempt to maintain a 1C rate. The concentration of $Al_2Cl_7^-$ would also increase to its maximum, ready for the charge cycle. Once the data is exported, this was followed by a charge step with a constant applied current which finishes when the potential reaches 2.4 V vs $Al/AlCl_4^-$ where the data is then exported separately.

Where equipment would allow, an advanced procedure was implemented that could automatically control and alter the applied current mid-test after an intial cycle's data had been exported. This worked by creating a repeat function in the Nova 2.1 electrochemical software and importing the previous cycle's current value and resultant C-rate which had been exported previously.

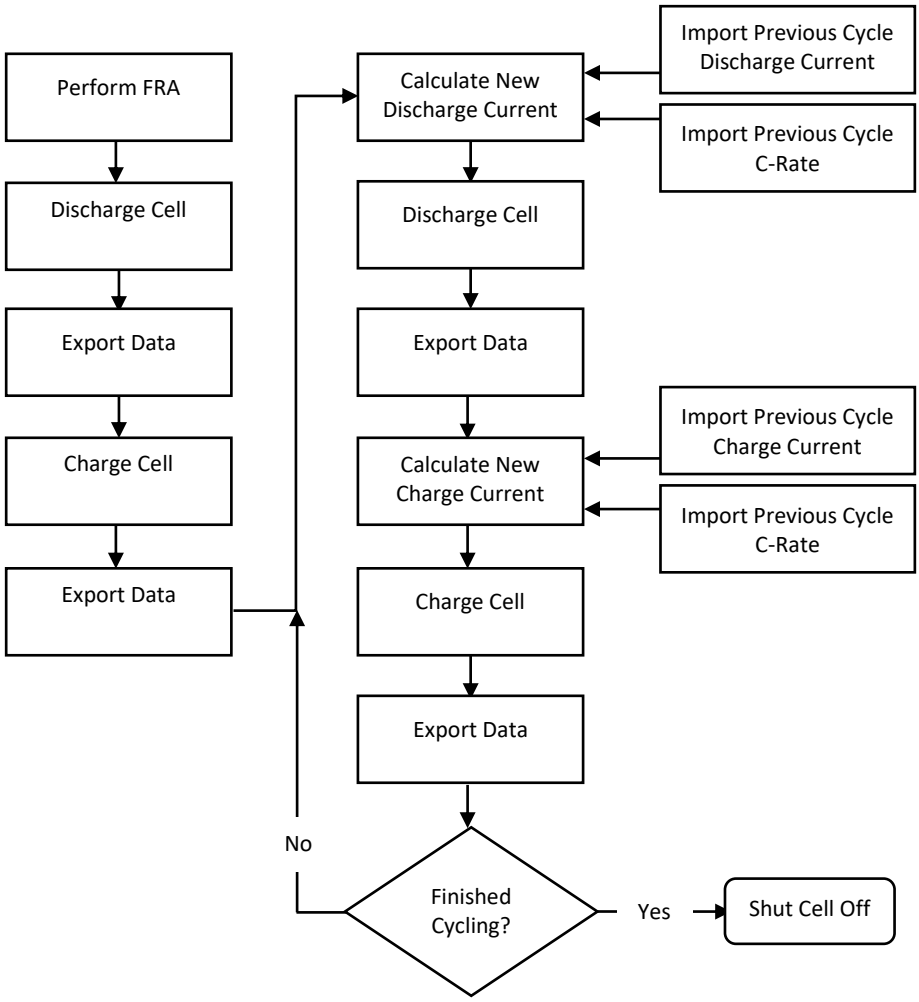

Figure 3-6 – Flow chart representing a dynamic galvanostatic charging procedure to stabilize a cell's charge rate

A calculation is then made to produce a new current to be readily applied in the subsequent discharge or charge. This calculation modifies the existing current using an arbitrary x value which can be altered to affect the size of the current change.

$$Current_{n-1} \times (C - rate_{n-1})^{-x} = Current_n$$

The resultant C-rate and the current that caused it are exported and saved on each cycle, ready to be imported and used in the next cycle. The same calculation occurs for both the discharge and charge current. Once the desired number of charge/ discharge cycles have been carried out, the test finishes.

The specific capacity, coulombic efficiency, and specific energy of the cell are calculated from the data by using Eq. 3-1, Eq. 3-3, and Eq. 3-4 below respectively.

$$Specific\ Capacity\ (mAhg^{-1}) = \frac{Current\ (A) \times\ Time\ (hrs)}{Weight\ (g)} \times 1000 \quad \text{Eq. 3-1}$$

$$Specific\ Capacitance\ (Fg^{-1}) = \frac{Charge}{\text{Potential Range} \times \text{Weight}} \quad \text{Eq. 3-2}$$

The specific capacity uses current and time values as well as the weight of the active cathode material. This will include the weight of the intercalated anions, believed to be $AlCl_4^-$.

The coulombic efficiency can be worked out to inform how much of the charge is being returned after it has been put into the battery.

$$Coulombic\ Efficiency\ (\%) = \frac{Discharge\ capacity}{Charge\ capacity} \times 100 \quad \text{Eq. 3-3}$$

Specific energy is the power that is contained within the battery per unit mass, given in $Whkg^{-1}$. The average potential of the cell on discharge is used.

$$\begin{aligned} &Specific\ Energy\ (Whkg^{-1}) \\ &\quad = Average\ Potential\ (V) \\ &\quad \times Specific\ Capacity\ (Ahkg^{-1}) \end{aligned} \quad \text{Eq. 3-4}$$

3.5.1 Cyclic Voltammetry

Cyclic voltammograms (CV) were used periodically throughout testing to examine the electrochemical behaviour exhibited by the cell during both charging and discharging. The CVs were carried out at multiple scan rates between 10 mVs^{-1} and 100 mVs^{-1} within a potential range of 0.2-2.4 V. The different scan speeds provide a quick glance into the cell's redox chemistry, or a slower, more defined look at the reactions and their intensity.

3.5.2 Impedance

Electrochemical Impedance Spectroscopy (EIS) was used to check the impedance of the cell at different potentials and correspondingly provide data associated with the changes in resistances through the cell. Once fitted, values related to how different reactions during charging and discharging affect the resistance are calculated. The frequency range used was between 1×10^5 Hz and 1 Hz. ZSimpWin EIS software was used for circuit fitting. The equations used below to calculate the diffusion parameters assume a planar electrode.

$$B = \sqrt{\tau} \qquad \textit{Eq. 3-5}$$

$$Y_o = \frac{1}{\sqrt{2}\,\sigma_T} \qquad \textit{Eq. 3-6}$$

$$D = \left(\frac{dE}{dx}\frac{V_m}{nF\sigma}\right)^2 \qquad \textit{Eq. 3-7}$$

$$V_m = \frac{M}{\rho} \qquad \textit{Eq. 3-8}$$

$$\delta = B\sqrt{D} \qquad \textit{Eq. 3-9}$$

Where τ is the time constant, σ is the Warburg coefficient, V_m is the molar volume calculated from the molar mass M and density ρ. The differential of the cell potential with respect to the state of charge $\frac{dE}{dx}$ is gained from a discharge curve, D is the diffusion coefficient and δ is the diffusion length.

3.6 Characterisation

3.6.1 X-Ray Diffraction

XRD was carried out using powder X-ray diffraction by way of a PANalytical X'Pert Pro MPD. The samples were irradiated with Cu Kα X-ray radiation ($\lambda_{average}$ = 1.5418 Å), scanned over a range of 5-100° in 2θ. Analysis of the air sensitive samples was carried out in an airtight sample holder pictured in Figure 3-7. The aluminium sample holder resembles a standard XRD powder sample stage built to the same dimensions. In addition, a 3D printed dome was fabricated using grey poly(methyl methacrylate) to a thickness of 0.5 mm and sanded smooth. The dome slots down over an O-ring to form the airtight seal. Ex situ samples on top of a glassy carbon disc can be slotted into a well within the metal, as deep as the glassy carbon is thick, so that the sample sits flush with the top of the aluminium stage as is required for XRD analysis.

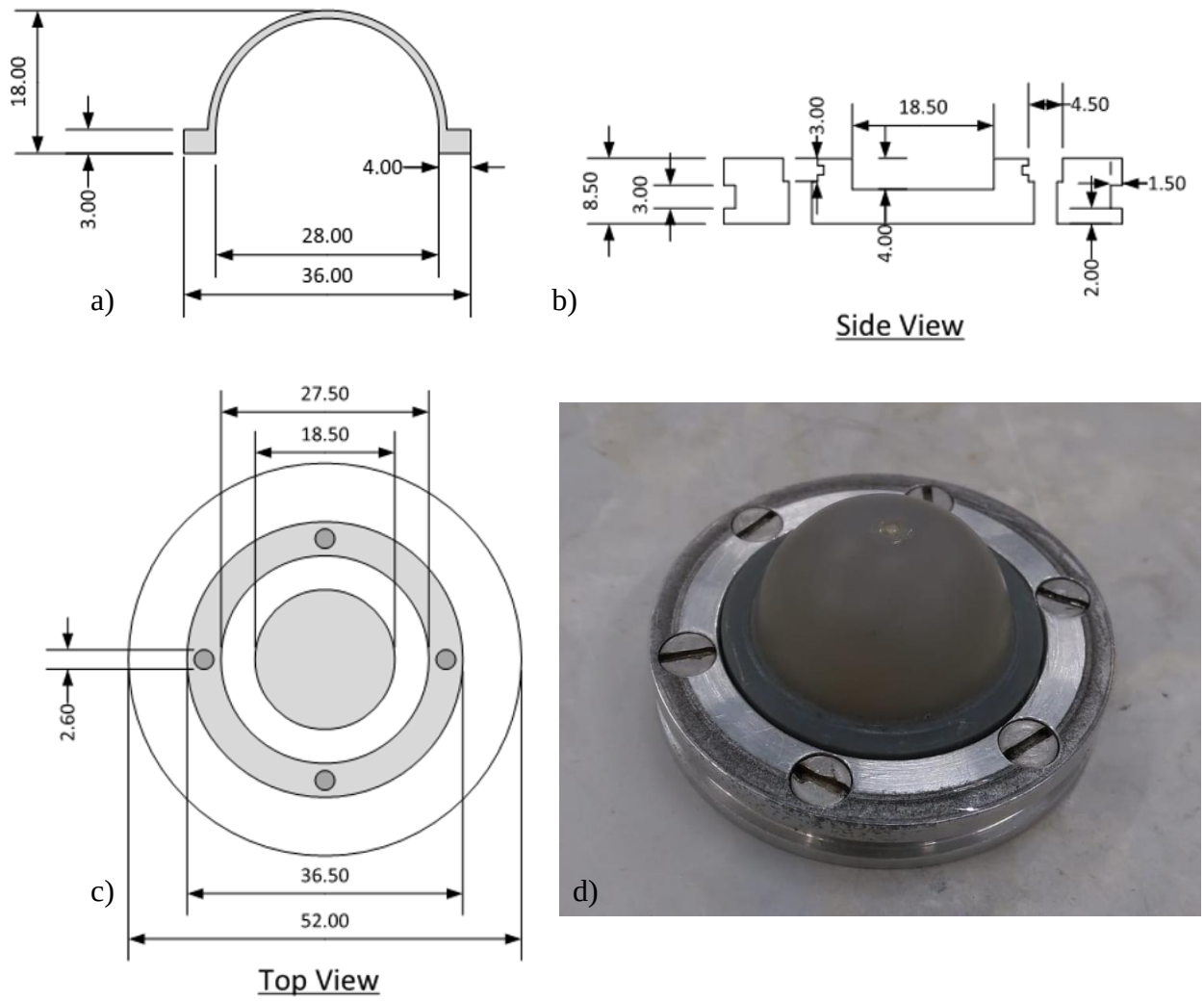

Figure 3-7 – a) profile of poly(methyl methacrylate) dome, b) profile view and c) top view of aluminium XRD sample holder base, d) photo of assembled airtight XRD sample holder

d-spacing was calculated using Bragg's law as in Eq. 3-10. Using Zhang's method, the stage number n, the repeat distance c, and the intercalant gallery height d_i can be worked out using Eq. 3-11 and Eq. 3-12 [80]. Where θ_{00n} and $\theta_{00(n+1)}$ are the θ angles of the split peaks at around 2θ 27°.

$$\lambda = 2d_{hkl}Sin\theta \qquad \textit{Eq. 3-10}$$

$$n = \frac{1}{\left(\frac{Sin\theta_{00(n+1)}}{Sin\theta_{00n}}\right)-1} \qquad \textit{Eq. 3-11}$$

$$c = n \times d_{00n} = (n-1) \times 3.35 + d_i \qquad \textit{Eq. 3-12}$$

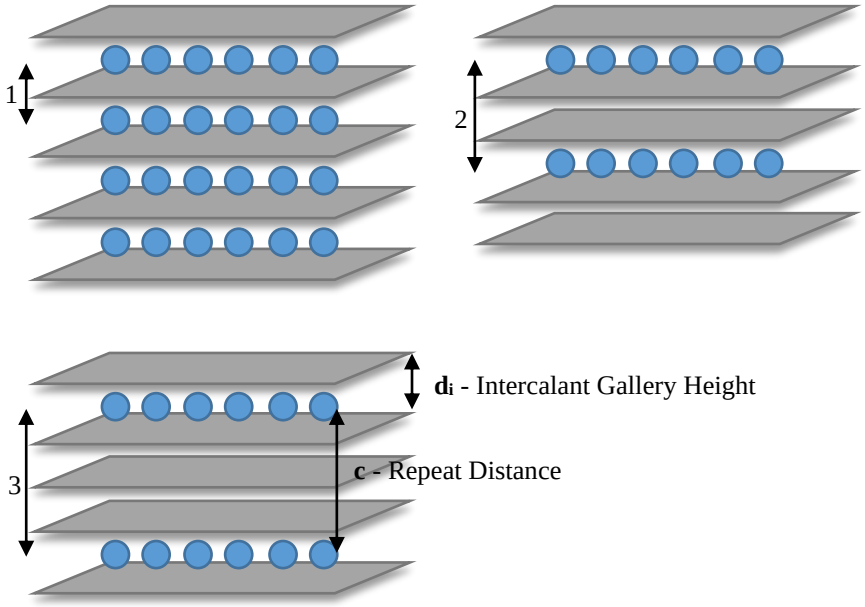

Figure 3-8 – Staging mechanism of intercalants into graphite layers depicting the stage number of intercalation 'n', the intercalant gallery height 'd_i' between host layers, and the repeat distance 'c' of the distance between intercalated layers

Interplanar spacing of crystal structures were calculated using Eq. 3-13, Eq. 3-14, and Eq. 3-15 below where h, k, l represent the miller indices of the chosen facet, and a, b, c are the distances to be found in Angstroms.

Cubic $$d_{hkl}^2 = \frac{1}{(h^2+k^2+l^2)a^{\star 2}} \quad \text{where} \quad a^\star = b^\star = c^\star = \frac{1}{a}$$ *Eq. 3-13*

Hexagonal $$d_{hkl}^2 = \frac{1}{(h^2+k^2+hk)a^{\star 2}+l^2c^{\star 2}} \quad \text{where } a^\star = b^\star = \frac{2}{a\sqrt{3}} \quad c^\star = \frac{1}{c}$$ *Eq. 3-14*

Orthorhombic $$d_{hkl}^2 = \frac{1}{(h^2a^{\star 2}+k^2b^{\star 2}+l^2c^{\star 2})} \quad \text{where } a^\star = \frac{1}{a} \quad b^\star = \frac{1}{b} \quad c^\star = \frac{1}{c}$$ *Eq. 3-15*

3.6.2 Raman

Raman was conducted using an external argon laser (514 nm) on graphite and rGO samples both charged to 0.8 V and 2.2 V vs Al/Al^{3+} for analysis. The accumulation time was 10 seconds with 3 accumulations averaged for each spectrum. Peaks were deconvoluted using Origin Pro software.

3.6.3 Mass Spectrometry

A Hidden Analytical residual gas analyser was used to conduct mass spectrometry tests on 1:1.3 Emic/$AlCl_3$ electrolyte during degradation studies. Scans were run from mass 1 to 300 to capture the full scope of the electrolyte mass and fragments generated.

3.6.4 Scanning Tunnelling Microscopy

The STM microscope is located inside of an MBraun glovebox fitted with a large granite slab that dampens most if not all the vibrations given off by the glove box as well as vibrations created within the immediate vicinity. This allows for STM to be run without any vibrational interference from the glovebox; the equipment uses a fine needle-like tip that records movements of less than a micron, any external interfering movement will severely affect the experimental results.

The scanning tip consists of a small piece of platinum/ iridium wire which is coated in an insulating wax leaving only the tip uncovered. The insulating wax limits the conductivity of the wire to the tip for the microscope to function correctly. Once a tip has been manually inserted into the microscope, a settling period is observed. An uncertain amount of drift will be present for a few hours after insertion which is evident from images of a constantly changing STM position. This is potentially caused by temperature changes of the wire or the weight of itself causing bends in the wire to be straightened.

An assembled cell was needed to check and calibrate the setup with a few CVs run to activate the cell. The acidic electrolyte attacked the platinum/ iridium tip and possibly the Apiezon wax coating causing an erratic current. The electrolyte was deemed too corrosive for the metallic tip, so the potential of the tip was altered to counter the changing current. Once stable, CVs were run between 1-1.9 V vs Al/Al^{3+} while STM were recorded. The onset of intercalation brought the surface too close to the tip causing noise in the imagery and occasional crashing of the tip into the surface.

Analysis was performed using WSxM 4.0 Beta 9.3 software [81].

Chapter 4. Study of Imidazolium Electrolyte for Suitability in Electrochemical Cells

4.1 Introduction

This study was carried out to investigate the effect of the electrolyte composition and the anode material on the reaction mechanisms and charging and discharging characteristics on the aluminium cell. As the electrolyte potential window plays an important role in the electrochemical stability and the electrochemical potential range of a cell, revealing which interactions play a part on increasing or decreasing this window would be highly important. A series of questions are thus addressed in this work. What is the limiting factor to achieve a larger cell capacity? How does the electrolyte ratio effect, either aid or hinder cell performance? Most importantly, finding out what reactions occur during anodic or cathodic degradation of the cell, especially as there is some uncertainty regarding specific reaction schemes within the literature.

4.2 Electrolyte Potential Window

The electrolyte being investigated is ethyl-methylimidazolium chloride (Emic) / $AlCl_3$ and in order to utilise this electrolyte to its full potential in battery technology, the electrochemical stability window of the upper and lower limits of degradation of the electrolyte need to first be identified.

A three-electrode cell with dual platinum electrodes and an Ag/AgCl reference electrode, with a standard electrode potential of 0.23 V vs SHE, were used to reveal these limits. The catalytic nature of platinum will reveal the smallest of reactions, and the removal of an aluminium source from the electrodes will limit the aluminium plating and stripping ability within the cell. The reactions that remain will be the oxidation and reduction of the electrolyte as well as any extra reactions present due to contaminants/ unknown species. The accuracy of the AgCl reference was determined using ferrocene.

4.2.1 Imidazolium Chloride / Propylene Carbonate

4.2.1.1 Oxidation Stability

The investigation into Emic combined with $AlCl_3$, its electrochemistry, as well as its stability as an electrolyte begins with the testing in the absence of aluminium metal and therefore in the absence of aluminium chloride. Emic/ $AlCl_3$ forms a eutectic mix from the two individual salts which lower the melting point to form an ionic liquid at room temperature, therefore in the absence of one of

them, a solvent is required and so solid imidazolium chloride salt was dissolved in propylene carbonate (PC) at room temperature. Cyclic voltammetry was run on the platinum electrodes, pushing the limits until degradation of the imidazolium and chloride ions could be observed.

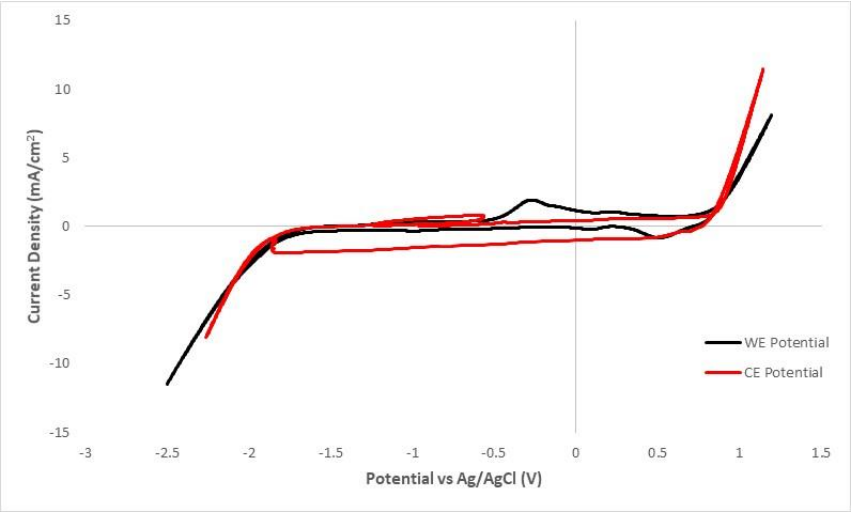

Figure 4-1 – CV of Platinum WE & CE cell, Emic/ PC electrolyte, WE scanned from -2.5 to 1.2 V at 20 mVs^{-1}

Figure 4-1 shows the voltammogram from -2.5 V to 1.2 V vs Ag/AgCl. The Emic/PC electrolyte provides a clear cell stability window of 2.6 V. The two main reactions expected here are the reduction of the imidazolium ion and the oxidation of the chloride ion, both degradation reactions which negatively affect the electrolyte. The stability window of PC is larger than these reactions, occurring between around -2.4 V to +2.15 V vs Ag/AgCl [82, 83] and is therefore not affected by the scan range used.

The onset of the oxidation reaction at +0.8 V vs Ag/AgCl is expected to be the oxidation of chloride ions into chlorine gas. The standard redox potential for chlorine evolution as seen in Eq. 4-1 is 1.36 V vs SHE or 1.14 V vs Ag/AgCl.

$$2Cl^- \leftrightarrow Cl_2 + 2e^- \qquad 1.36 \text{ V vs SHE} \qquad \textit{Eq. 4-1}$$

This indicates a potential shift of just over 300 mV in the negative direction from the standard redox or around 200 mV from certain literature observations [84]. While a possible explanation would be due to ionic concentration changes as would be predicted by Le Chatelier's principle/ Nernst equation; in any chemical system the favoured reaction is the one that has the most reactant

available in order to restore chemical equilibrium between reactant and product. Due to the makeup of the electrolyte consisting equally as much of Cl^- ions as $Emim^+$, a large concentration gradient of Cl^- to Cl_2 occurs upon fabrication of the electrolyte. The Nernst equation, relating ionic concentration to potential, states that an order of magnitude difference in ionic concentration would provide a potential shift of 59/n mV, where n is the number of electrons in the process. For the 2-electron process of chloride oxidation in Eq. 4-1, this would become 28 mV per order of magnitude. This is unlikely as at least 10 orders of magnitude increase in the chloride concentration from 1M would be required to display a shift in oxidation peak down to 0.8 V vs Ag/AgCl under standard conditions. Such a large shift in redox potential could possibly be explained by the solvation of the chloride ions within PC i.e. change of solvent effect, allowing for an easier oxidation reaction. A different explanation is that a trichloride oxidation reaction could be happening which could lead to chlorine formation through an equilibrium reaction [85]. These reactions, Eq. 4-2 and Eq. 4-3 are written below. The potential of the trichloride oxidation in Eq. 4-2 has been given by different researchers at potentials ranging from 0.23-1.6 V vs Ag/Ag^+ [84, 85], with the former taking place in the presence of gold chloride, indicating that the solvent as well as the coordination with metals can shift the redox potential quite drastically.

$$3Cl^- \leftrightarrow Cl_3^- + 2e^- \qquad 0.23 - 1.6 \text{ V vs } Ag/Ag^+ \qquad \textit{Eq. 4-2}$$

$$Cl_3^- \rightarrow \frac{3}{2}Cl_2 + e^- \qquad 0.89 \text{ V vs } Ag/Ag^+ \qquad \textit{Eq. 4-3}$$

The onset of Cl^- to Cl_2 oxidation on a glassy carbon electrode in $[C_4mim][BF_4]$ and $[C_4mim][Ntf_2]$ occurs at around 0.7 V and 1.0 V vs Ag/Ag+ respectively [84, 86], differing from that seen in Figure 4-1 by at least 100 mV. When oxidised at a gold electrode, The oxidation potential shifts to 1.55 V with a trichloride reaction as seen in Eq. 4-2 occurring around 1.05 V [86] This implies that in the absence of gold, the intermediate Cl_3^- ion does not form, and Cl_2 evolution as in Eq. 4-1. takes place when using a glassy carbon electrode. Other studies [85], similarly using platinum working electrodes display a singular oxidation peak at just over 1.5 V vs Ag wire that is attributed to chloride oxidation. Peak fitting and estimation led to the conclusion that the Cl^- ion was mainly oxidising to Cl_3^- as in Eq. 4-2 rather than Cl_2, as no gas bubbles were observed on the Pt electrode.

$$Cl_2 + Cl^- \leftrightarrow Cl_3^- \qquad \textit{Eq. 4-4}$$

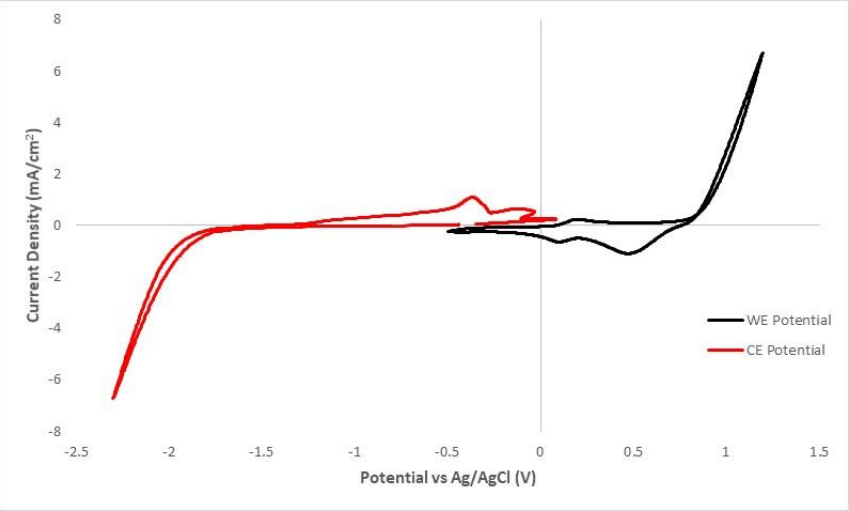

Figure 4-2 – CV of Platinum WE & CE cell, Emic /PC electrolyte, WE scanned from -0.5 to 1.2 V at 20 mVs^{-1}

Limiting the potential range of the WE, focussing on the oxidation degradation reaction in Figure 4-2 shows a moderate reduction at 0.5 V. Similarly, no gas bubbles were seen here leading to the conclusion that Cl^- ions oxidise to Cl_2 but remains solvated within the electrolyte forming Cl_3^- as seen in the equilibrium reaction in Eq. 4-4. Figure 4-3 shows an increasing reduction peak at 0.3-0.8 V with decreasing scan rate. This is counter intuitive, as peak size tends to get larger as the scan rate increases, as demonstrated from the Randles-Sevcik equation below:

$$i_p = 2.69 \times 10^5 n^{\frac{3}{2}} A D^{\frac{1}{2}} C v^{\frac{1}{2}} \qquad \textit{Eq. 4-5}$$

$$i_p \, \alpha \, v^{\frac{1}{2}} \qquad \textit{Eq. 4-6}$$

Where i_p represents peak current and v represents scan rate. This occurs due to the increased voltage applied resulting in a larger concentration gradient of the species which in turn allows for the smaller diffusion layer and an increase in current. If the reaction is kinetically limited, then the peak potential will shift in the positive direction as the scan rate increases. This can be explained by slower scan rates resulting in larger oxidation product formation for the same scan window, which will result in larger concentration in solution of these products and consequently larger reduction current. In other words, the concentration term 'C' of reactive species in Eq. 4-5 is not

constant and depends on the charge passed during the oxidation reaction, and the increase in C due to slower scan rate outweighs the decrease in the value of the square root of scan rate term.

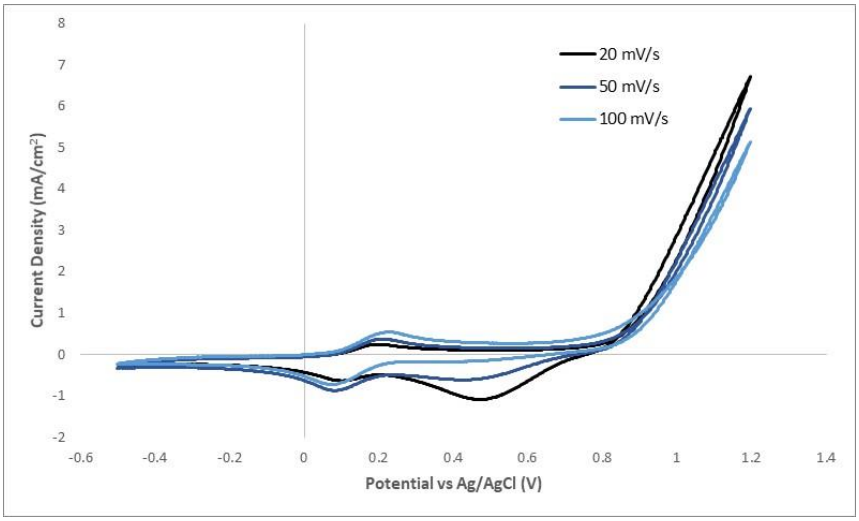

Figure 4-3 – CV of Platinum WE, Emic /PC electrolyte, scanned from -0.5 to 1.2 V at 100, 50, & 2 0mVs^{-1}

An estimate of the Cl_2 evolution or other Cl- oxidation product concentration in the electrolyte from Figure 4-3 using the Randles-Sevcik equation can be made to be roughly 6000 ppm at 20 mVs^{-1} although due to the equation applying to aqueous solutions, this is only an estimate and cannot accurately conclude chlorine levels. The approximation can be used to directly compare to chlorine estimating the levels of impurity to be in the 100s of ppm, although without knowing the molecular makeup and therefore the diffusion coefficient, this estimation has a much lower level of accuracy.

4.2.1.2 Reduction Stability

A clear reduction of $Emim^+$ begins around -1.8 V in Figure 4-1. Reports on this reduction reaction observe the $Emim^+$ reduction in the region of -2.3 V to -2.0 V, with the potential shifting a few hundred millivolts due to the different solvents used with $Emim^+$ [87]. More specifically, it is believed that the imidazolium cation is reduced with a single electron at -2.28 V vs SCE as in Eq. 4-7 losing a hydrogen atom and forming a carbene. Literature confirms the formation of an imidazolium radical, yet the oxidation peak detected at -0.2 V is labelled as the result of carbene oxidation that only appears after reduction of the imidazolium cation [88]. This reveals that the radical formed must decompose to release hydrogen and form a carbene.

Based on the principle of solvents affecting the reduction potential, a slightly larger shift in reduction to -1.8 V vs Ag/AgCl due to the combination of PC and Emic is not inconceivable and is taken as being the observed reaction. This is due to no other reduction reactions being expected within this electrolyte and scan range. The reduction reaction features the addition of a single electron and forming a carbene; the corresponding oxidation reaction, seen in Figure 4-1 and Figure 4-4 is believed to be the oxidation of the Emim carbene structure.

$$Emim^{+} + e^{-} \rightarrow 1, ethly, 3, methylimidazol, 2, ylidene + \frac{1}{2}H_2 \qquad \textit{Eq. 4-7}$$

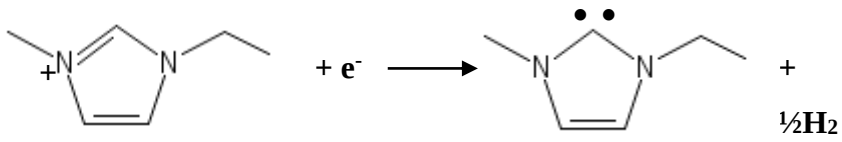

The Emim degradation reactions are demonstrated further in Figure 4-4, with a shortened range to exclude the oxidation of chloride at the working electrode, showing no immediate reversable oxidation peak following the reduction at -1.8 V. This single electron reduction is therefore deemed irreversible. The broad oxidation -0.3 V in Figure 4-1, now seen more clearly in Figure 4-4 as two separate peaks at -0.3 V and -0.15 V, are the oxidation of products from the $Emim^{+}$ reduction. The peaks are in keeping with literature; the reduction of $Emim^{+}$ at around -2.2 V vs Ag wire resulted in oxidation peaks at -0.65 V and -0.45 V. The coulometric data suggested that the $Emim^{+}$ reduction is a one electron process [87] though the identity of the molecules causing them was not determined. Removal of tetrabutylammonium perchlorate (TBAP) from the electrolyte allowed for a positive shift in the potentials: $Emim^{+}$ reduction at -2.0 V, oxidation peaks at -0.2 V and 0.0 V. As for $Emim^{+}$ cations, dimerization between two Emim molecules at the point of H^{+} loss has been confirmed via IR spectra at -2.4 V vs Ag/AgCl [89] generating hydrogen as a bi-product. This occurs during $Emim^{+}$ reduction and does not take place during a separate oxidation.

Gorodetsky et al. did not see a second oxidation peak and concluded that the formation of a carbene matched with their results [88]. The peaks in Figure 4-4 have no associated reduction peaks meaning that they are also irreversible.

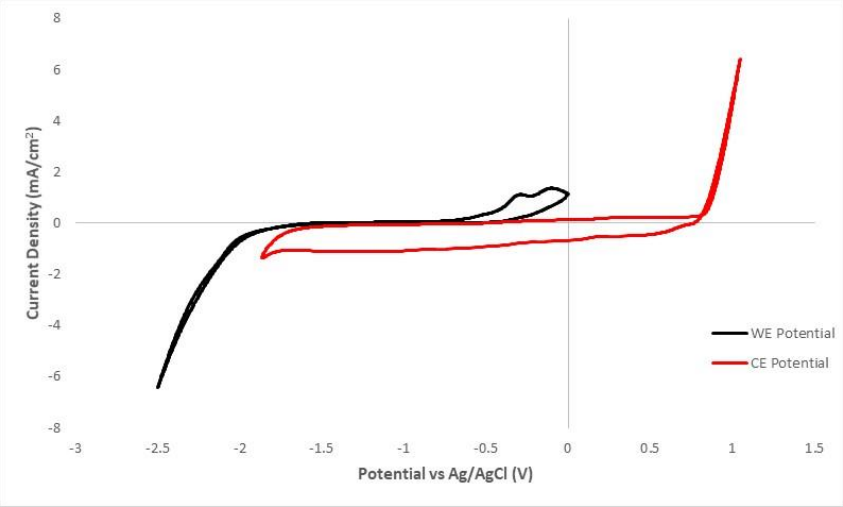

Figure 4-4 – CV of Platinum WE & CE cell, Emic /PC electrolyte, WE scanned from -2.5 to 0 V at 20 mVs^{-1}

To investigate further whether this dual oxidation was caused by anything other than the products of the imidazolium reduction, the scan range was shortened to avoid the $Emim^+$ reduction at -1.8 V. Figure 4-5 shows that the current from the two oxidation peaks between -0.5-0 V has decreased by a factor of 10 as the reduction current of $Emim^+$ also decreased by an order of magnitude by limiting the cathodic limit to -1.8 V in agreement with the discussion above.

4.2.1.3 Effect of Impurities

The extension of the scan range in the positive direction of the working electrode revealed a highly reversible reaction with a low current density at around 0.2 V vs Ag/AgCl. This redox, which is also slightly visible in Figure 4-1, could be caused by impurities present in the PC solvent. The current produced from this redox reaction is skewed towards oxidation with half-wave potential located at around 0.15 $mAcm^{-2}$ instead of 0 A. This is accompanied by the reduction of imidazolium at the counter electrode, resulting in more of the imidazolium carbene from Eq. 4-7 being formed. The increase of this imidazolium in turn has led to a greater oxidation of its products at the counter electrode as the beginnings of a larger peak can be seen.

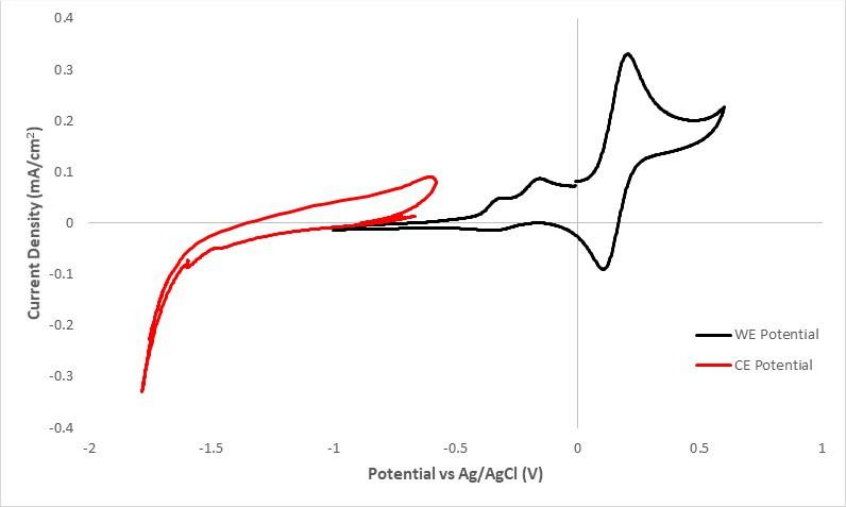

Figure 4-5 – CV of Platinum WE & CE cell, Emic /PC electrolyte, scanned from -1 to 0.6 V at 20 mVs^{-1}

4.2.2 Imidazolium Chloride / Aluminium Chloride 1:1

An electrolyte ratio of 1:1 is created with aluminium chloride ($AlCl_3$) and imidazolium chloride via the substitution of the solvent propylene carbonate for $AlCl_3$ salt. The two salts together form a eutectic mix that allows for an ionic liquid at room temperature. To check how the addition of $AlCl_3$ affects the potential stability window of the electrolyte, the same dual platinum electrode setup is used as before, and the new limits are identified.

4.2.2.1 Reduction Stability

From both Figure 4-6 and Figure 4-7 below, it is clear that the lower potential limit at which the reduction of the $Emim^+$ cation takes place begins around -1.7 V vs Ag/AgCl, similar to observations in section 4.2.1.2 in the absence of $AlCl_3$. However, the resulting oxidation peak of the $Emim^+$ reduction products, previously seen at -0.3 V in Figure 4-1 has decreased substantially at the WE due to the applied potential limiting the extent of $Emim^+$ reduction thus reducing the amount of the reduction products formed. This oxidation may be inhibited by the addition of $AlCl_3$. to the electrolyte and the resulting chloride oxidation products.

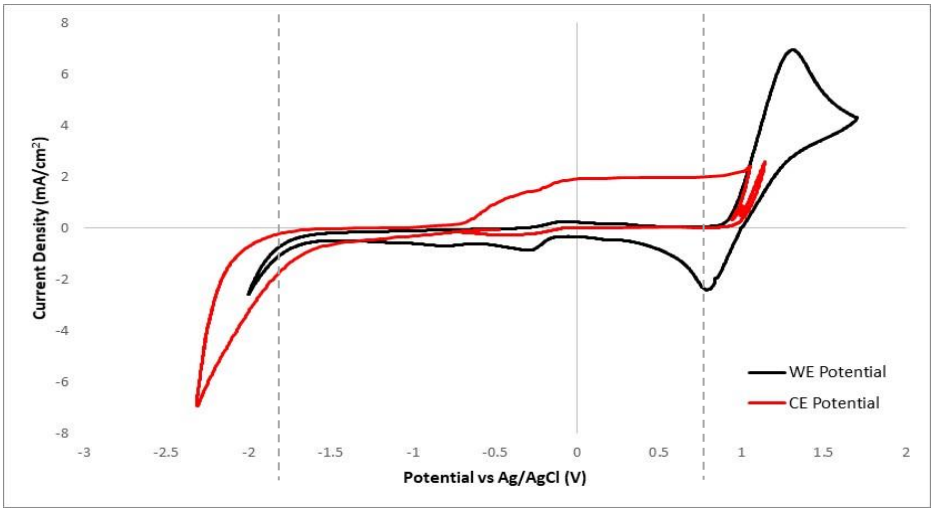

Figure 4-6 – CV of Platinum WE & CE cell, Emic/$AlCl_3$ 1:1 electrolyte, scanned from -2 to 1.8 V at 20 mVs^{-1}

4.2.2.2 Oxidation stability

The upper electrolyte limit from the oxidation reaction, begins at around 0.9 V vs Ag/AgCl. This reaction has shifted 100 mV in the positive direction from Emic/PC. The cause of this is explained by the complexing of Cl^- to $AlCl_4^-$ making it more difficult to oxidise. Carlin et al. reports the Cl^- oxidation reaction taking place at 2.7 V vs Al/Al^{3+}, equating to 0.8 V vs Ag/AgCl, when using a 1:1.1 ratio of Emic/$AlCl_3$ [90]. Although this is a different, acidic electrolyte composition than the current neutral 1:1 test, the oxidation of Cl^- from $AlCl_4^-$ seen in Figure 4-6 is in line with literature values and is closer toward the standard Cl^- oxidation potential.

$$4AlCl_4^- \rightarrow 2Al_2Cl_7^- + Cl_2 + 2e^- \qquad \textit{Eq. 4-8}$$

The mass transport limitation beyond 1.35 V in Figure 4-6 during the $AlCl_4^-$ oxidation and the proposed reaction Eq. 4-8 suggests that the evolution of chlorine from $AlCl_4^-$ is not as efficient as with EmimCl/PC, requiring 16 chlorine atoms to generate a single chlorine gas molecule. The main product from this reaction scheme is the large aluminium complex. The reaction appears to be more reversible than that seen in Figure 4-3 in the absence of $AlCl_3$ which suggests that different redox reactions are taking place in the presence and absence of $AlCl_3$. Comparing Figure 4-6 with Figure 4-3 regarding the reversibility of the chloride redox, the reductions occur at 0.8 V and 0.5 V vs Ag/AgCl respectively. This demonstrates the varying degrees of electron transfer and therefore the reversibility between the two systems: the high reversibility from a narrow peak-to-peak separation

in Figure 4-6 and the wider separation, and therefore slower and more irreversible redox in Figure 4-3.

The reduction peak current in Figure 4-6 is almost double that of Figure 4-3. While this might be explained by larger oxidation window (0.9-1.8 V compared to 0.8-1.2 V) leading to a larger concentration of oxidation products in electrolyte, the difference in reversibility of the reaction suggests that the reduction products are different. The larger oxidation charge in comparison to reduction charge suggests that a small amount of chlorine gas evolved, or other soluble oxidation by-products are being reduced back into the electrolyte. It is noted as well that no gas bubbles were seen leaving the electrodes. However, this is not surprising considering that the oxidation current is relatively small at 1.37 mA equating to a Cl_2 flowrate of 7.1 $x10^{-9}$ $mols^{-1}$. Mass spectrometry was therefore used to detect any Cl_2 gas produced as discussed later in section 4.2.3.1. Due to the $AlCl_4^-$ forming $Al_2Cl_7^-$ upon degradation, it can be seen on the reverse scan around -0.2 V that a small amount of aluminium plating and stripping is taking place. This can only take place in the presence of larger chloroaluminate ions as will be discussed later.

Figure 4-6 also shows the accompanying reduction reaction at the counter electrode to the chloride oxidation at the working electrode. This reaction is the degradation reduction of $Emim^+$ below -1.6 V as discussed above and reinforces the view that a degradation reaction involving chloride oxidation is taking place at the working electrode, as these two reactions mark the overall degradation of the electrolyte. Interestingly, the reduction at 0.8 V at the working electrode triggers the reverse oxidation reaction at 0.9 V at the counter electrode. This was not seen in Figure 4-2 and confirms that the redox species involving chloride ions around 0.9 V is different in the presence of $AlCl_4^-$ as the concentration of Cl^- diminishes. The potential of both the working and counter electrodes are visible in Figure 4-7 which depicts each electrode potential and the cell potential with respect to time. It can be seen that the oxidation of $Emim^+$ reduction products occurring at the CE around -0.5 V is not large or fast enough to support the Cl_2 reduction rate at the working electrode, hence the CE moves to a higher potential to the oxidation of $AlCl_4^-$. The two separate peaks seen at the counter electrode at 0.9 V and 1.0 V are the same $AlCl_4^-$ reaction.

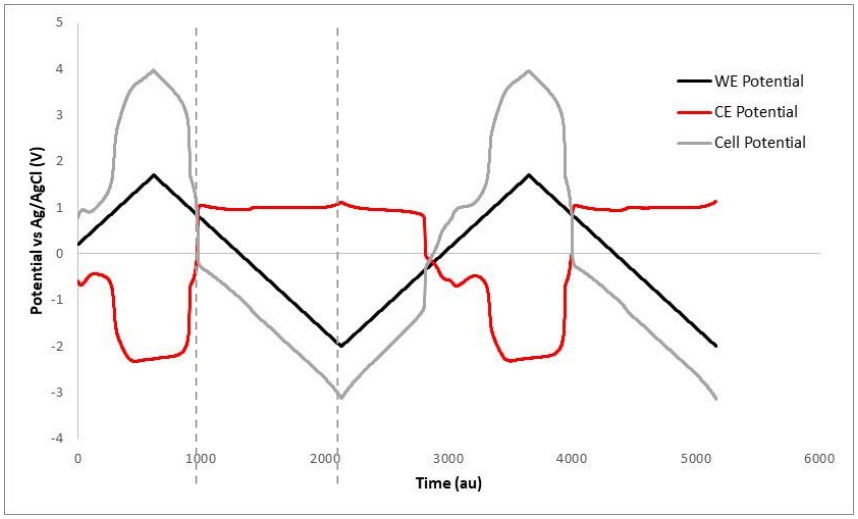

Figure 4-7 – Linear sweep voltammetry of Platinum WE, CE, & full cell potentials, Emic/$AlCl_3$ 1:1 electrolyte, scanned from -2 to 1.8 V at 20 mVs^{-1} (Potential vs Time)

4.2.3 Imidazolium Chloride / Aluminium Chloride 1:1.3

Due to the enhanced charging properties of increased electrolyte content of $AlCl_3$, testing was carried out on a 1:1.3 ratio of Emic:$AlCl_3$ deemed the most suitable from the literature review. The addition of 0.3 moles $AlCl_3$ to a 1:1 molar ratio electrolyte gives us a 1:1.3 ratio of Emic/$AlCl_3$ or in other words the formation of mixture of $AlCl_4^-$ and $Al_2Cl_7^-$ ions in the electrolyte. The same cell setup is used as with previous tests. An additional aluminium wire reference was used in the cell and measured against an Ag/AgCl reference electrode to show how the change in aluminium ion concentrations within the electrolyte during the redox reactions would affect the anode potential and attempt to estimate the amount of concentration change using Nernst equation.

Figure 4-8a shows the potential change recorded in an aluminium reference in the 1:1.3 electrolyte as function of the working electrode current. Eq. 4-10, for the reduction of $Al_2Cl_7^-$ in Emic/$AlCl_3$ can be seen below. The half wave potential of this reaction at operating conditions is indicated by the potential of the aluminium reference electrode at zero current. For the 1:1.3 electrolyte, at equilibrium this was around -0.2 V vs Ag/AgCl and not the predicted standard value of -1.67 V vs SHE for Al/Al^{3+} redox. The deviation can be explained by the different chemical nature of Al^{3+} due to the coordination of Cl^- ions around the aluminium ion [91]. Compared to the 1:1 electrolyte ratio where the primary anion is $AlCl_4^-$, in the 1:1.3 ratio the presence of a higher concentration of $Al_2Cl_7^-$ enables the rapid plating reaction of Al as shown in Eq. 4-10.

$$AlCl_3 + AlCl_4^- \rightarrow Al_2Cl_7^-$$ *Eq. 4-9*

$$4Al_2Cl_7^- + 3e^- \leftrightarrow Al + 7AlCl_4^-$$ *Eq. 4-10*

$$3_nC[AlCl_4] + 3e^- \leftrightarrow 3_nC[\,] + 3AlCl_4^-$$ *Eq. 4-11*

$$Al + 7AlCl_4^- + 3_nC[AlCl_4] \leftrightarrow 3_nC[\,] + 3AlCl_4^- + 4Al_2Cl_7^-$$ *Eq. 4-12*

Observing the Nernst equation and Le Chatelier's principle of equilibrium, the mechanism by which the potential change occurs is clear; from Eq. 4-10 and Eq. 4-14, as the forward reduction reaction happens, more $AlCl_4^-$ is formed, causing the equilibrium to shift in the reverse direction in turn causing $Al_2Cl_7^-$ production to be more favourable. The Nernst equation predicts that when the concentration of $AlCl_4^-$ is increased, the equilibrium potential of the redox reaction in Eq. 4-10 of Al striping and plating shifts negatively. Oppositely, as $Al_2Cl_7^-$ concentration is increased the equilibrium potential shifts towards higher potentials.

For a cell with a carbon positive electrode and Aluminium negative electrode, the full cell equilibrium cell voltage equation is given in Eq. 4-12. The equilibrium and Nernst equation dictate in Eq. 4-13 that the potential will move in opposition to the $Al_2Cl_7^-$ half-cell as the aluminium and therefore the Al stripping/ plating reactions are at the counter electrode.

At the anode:

$$E_a = E_a^\Theta + \frac{RT}{nF}\ln\left(\frac{[Al_2Cl_7^-]^4}{[AlCl_4^-]^7}\right)$$ *Eq. 4-13*

At the cathode:

$$E_c = E_c^\Theta + \frac{RT}{nF}\ln\left(\frac{[AlCl_4^-]^3}{1}\right)$$ *Eq. 4-14*

$$E_{cell} = E_{cell}^\Theta + \frac{RT}{nF}\ln\left(\frac{[AlCl_4^-]^3[Al_2Cl_7^-]^4}{[AlCl_4^-]^7}\right)$$ *Eq. 4-15*

Figure 4-8 displays a 4-electrode cell with AgCl and Al wire references consisting of platinum electrodes, one plated with aluminium. When charging the cell, the working electrode undergoes aluminium stripping, creating more $Al_2Cl_7^-$ from the reaction as seen in Eq. 4-10. In Figure 4-8a the aluminium wire reference electrode, which is situated closer to the working than the counter electrode, responds with an increase in potential in line with the Nernst prediction. In theory the Al reference should not change potential in a symmetrical cell as the reactions occurring at each electrode would cancel the effects of each other out. However, in practice the local environment around the electrodes are slow to equilibrate with the bulk electrolyte. A limiting current can be seen at the WE, showing the lack of available aluminium ions required to further the reactions. This confirms that the cell's limiting factor is the concentration of $Al_2Cl_7^-$ present in the solution.

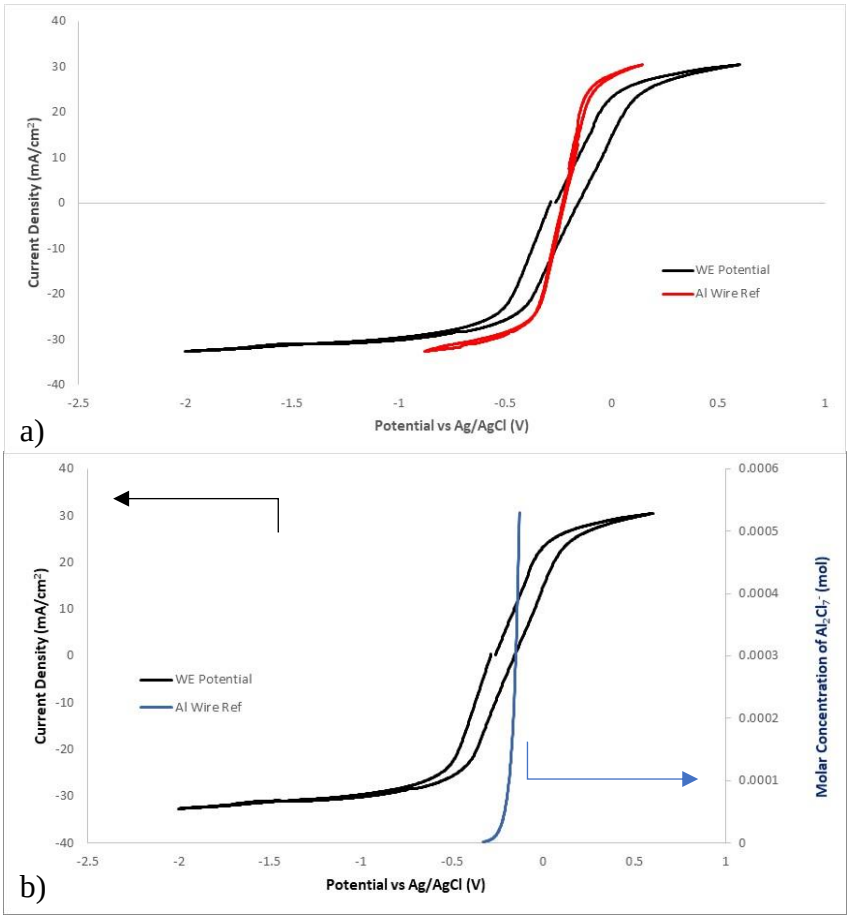

Figure 4-8 – CVs of Platinum WE & Al wire REF, Emic/$AlCl_3$ 1:1.3 electrolyte, scanned from -2 to 0.6 V at 20 mVs^{-1}, including (a) Al REF potential shift vs current density (b) Al REF potential shift vs $Al_2Cl_7^-$ molar concentration

An estimate of the $Al_2Cl_7^-$ molar concentration can be seen in Figure 4-8b as an expression of Eq. 4-13 in relation to the changing potential of the Al reference. Comparing the current density obtained in Figure 4-8a for Al stripping and plating to that applied usually to cell, the range would

be substantially smaller by at least an order of magnitude, and the ionic concentrations would not have the opportunity to reach such extremes as intercalation into a graphite electrode is rate and capacity limiting, and finite compared to the relatively rapid aluminium plating and stripping. Figure 4-8b therefore only displays a smaller potential range of a couple hundred millivolts to approximate the changes of the molar concentration in an asymmetric cell. The concentration gradient of the ionic species in the electrolyte causes the potential of the aluminium reference electrode in Figure 4-8a to continue positively shifting, as the concentration of $AlCl_4^-$ ions in the local electrode environment is severely depleted causing a limiting current. On the reverse scan, although the oxidation reaction continues to occur until the current becomes negative, the exponential nature of the concentration gradient causes the aluminium reference potential to reverse as the reaction intensity decreases.

The kinetics of the stripping and plating are very fast as indicated by the rapid change in ionic concentration within the electrolyte. The ionic resistance encountered through the large inter-electrode distance, causes the decrease of j-V curve slope of the two electrode measurements between the symmetrical electrodes in comparison to that of mass transport effects of concentration of $AlCl_4^-$ and $Al_2Cl_7^-$ in electrolyte captured by the pseudo Al reference as can be seen in Figure 4-8a.

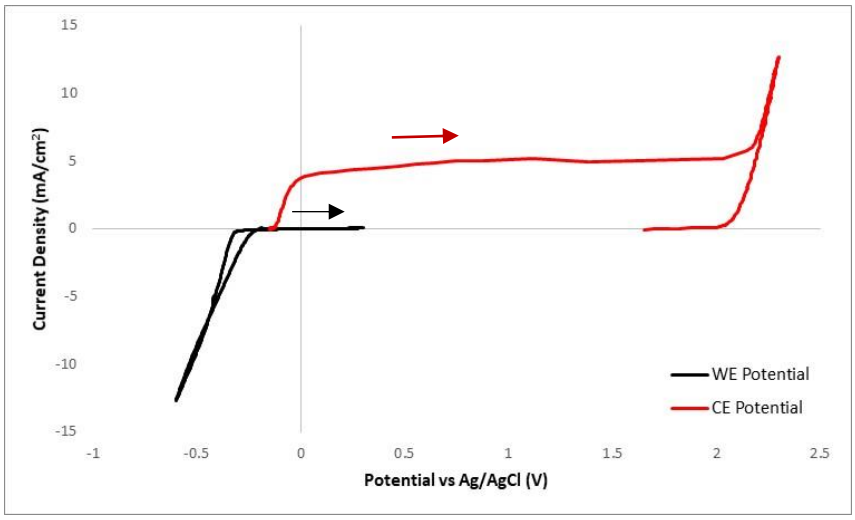

Figure 4-9 – CV of Platinum WE & CE cell, Emic/$AlCl_3$ 1:1.3 electrolyte, scanned from -0.6 to 0.3 V at 20 mVs^{-1} starting at -0.2 V, 1st cycle

When initially charging and discharging the cell, another limiting factor presents itself. Figure 4-9 shows the 1st scan of a symmetrical platinum cell. As the scan sweeps positive, from -0.2 V, no aluminium stripping takes place at the working electrode and likewise no reaction takes place at

the counter electrode. This happens because there is no aluminium to strip from the platinum working electrode, and the absence of a reaction at one electrode means nothing will occur at the other. During the negative sweep, plating occurs at the working electrode at -0.3 V. This is strange as the counter electrode is also platinum and cannot donate aluminium ions via stripping to replenish that which is plated onto the working electrode. Therefore, aluminium can be plated directly from the electrolyte without an aluminium counter, however in order to do so, $AlCl_4^-$ oxidation must occur at the counter electrode in order to balance the system and provide a source of electrons for the working electrode. This oxidation is occurring at 2.0 V vs Ag/AgCl, much higher than previously seen in the 1:1 ratio. This is due to the combination of chloride ions into even larger complexes than the 1:1 which makes it more difficult to oxidise, requiring an even larger potential, in this case shifting from 1-2 V.

$$6Al_2Cl_7^- \rightarrow 4Al_3Cl_{10}^- + Cl_2 + 2e^- \qquad \textit{Eq. 4-16}$$

Figure 4-10 shows the continuation of aluminium plating and stripping in the 2nd voltammetric scan. As the plating current at the working electrode gets too large, subsequently causing the current at the counter to match, the aluminium from the counter electrode is fully stripped. This leads to more aluminium complex oxidation taking place to further draw aluminium from the electrolyte and produce electrons. Wang et al. suggest larger aluminium complexes form in acidic melts when the potential is pushed to the anodic limit as in Eq. 4-16 [92]. The lack of observable gas bubbles from the cell doesn't necessarily go against the idea of Cl_2 evolution as depicted in Eq. 4-16 due to the relatively low current applied. However, there is no reduction current seen on the reverse scan from 2 to 1.5 V. A corresponding reduction reaction still occurs around 1 V as can be seen in Figure 4-10 on the reverse scan indicating it is the same reduction reaction occurring as in the neutral 1:1 electrolyte. Figure 4-10 is an example of how side reactions progress within the electrolyte; degradation of electrolytes take place when the current gets too high distorting the coulombic efficiency of the cell.

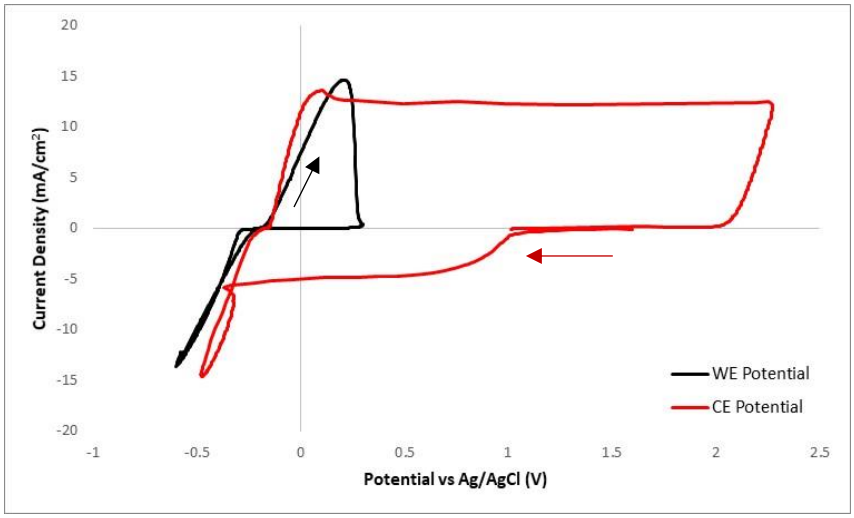

Figure 4-10 – CV of Platinum WE & CE cell, Emic/$AlCl_3$ 1:1.3 electrolyte, scanned from -0.6 to 0.3 V at 20 mVs^{-1} 2nd cycle

Figure 4-11 shows the full potential range of the symmetrical platinum electrode cell in the 1:1.3 electrolyte. Limits have previously been identified for the 1:1 electrolyte but were presumed to be different for a higher $AlCl_3$ concentration. Aluminium plating and stripping can be seen around the unchanged redox potential of -0.2 V vs Ag/AgCl producing large current densities. Pushing the potential further negative to elicit degrading behaviour shows limiting of aluminium plating until the degradation reaction of $Emim^+$ reduction is reached at around -2.5 V vs Ag/AgCl. This triggers the oxidation of chloride species reaction at +2.0 V at the counter electrode. The stability window has significantly increased more than the observed reduction and oxidation of $Emim^+$ and Cl^- in the 1:1 electrolyte. This is mainly caused by an increase of chloride species oxidation onset potential. The cause in observable shift for the reduction potential of $Emim^+$ is due to the aluminium plating becoming the more dominant reaction and the $Emim^+$ reduction can only be seen at very negative potentials beyond range were Al plating limiting current is seen.

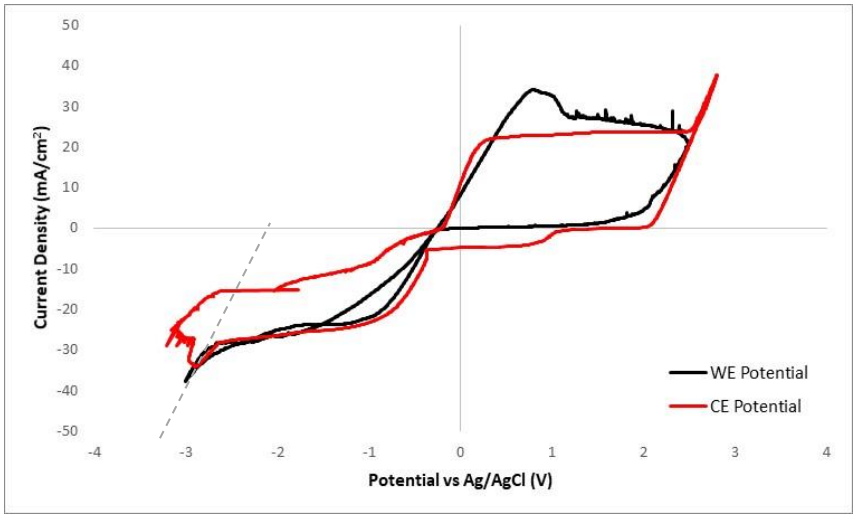

Figure 4-11 – CV of Platinum WE & CE cell, Emic/$AlCl_3$ 1:1.3 electrolyte, scanned from -3 to 2.5 V at 20 mVs^{-1}

Table 4-1 – Summary of redox reactions and their corresponding potentials

Potential (vs Ag/AgCl)	***Redox Reaction***
1.14 V	Standard Cl^- | Cl_2
-1.9 V	Standard Al^{3+} | Al
Emic/PC	
0.8 V	Cl^- | Cl_2
0.5 V	Cl_2 | Cl^-
-1.8 V	$Emim^+$ | Emim
-0.3 V	Emim oxidation
-0.15 V	Emim oxidation
Emic/AlCl3 1:1	
0.9 V	Cl^- | Cl_2
0.8 V	Cl_2 | Cl^-
-1.7 V	$Emim^+$ | Emim
Emic/AlCl3 1:1.3	
-0.2 V	Al | $Al_2Cl_7^-$
2.0 V	Cl^- | Cl_2
1.0 V	Cl_2 | Cl^-
~ -2.0 V	$Emim^+$ | Emim

4.2.3.1 Gas Analysis and Chlorine Evolution Verification

To confirm the evolution of chlorine from the degradation of 1:1.3 Emic/$AlCl_3$, residual gas mass spectrometry was carried out alongside chronoamperometry. Pushing the potential of the electrolyte beyond the predetermined electrochemical window will cause the degradation that is believed to cause chlorine evolution as well as reduction of imidazolium. This test will detect any chlorine as well as any gaseous forms of imidazolium if there are any. From the limits displayed in Figure 4-11, the voltage stability window for Emic/$AlCl_3$ is around 4 V and so the cell potential is incrementally increased up toward this amount.

Peaks from chlorine isotopes ^{35}Cl and ^{37}Cl are visible in Figure 4-12, but no peaks can be seen at masses 70, 72, and 74, which would confirm the presence of chlorine gas. Peaks at mass 36 and 38 are more prominent and appear in the same 3:1 ratio as the two chlorine peaks, representing the two chloride isotopes of HCl, which is present in larger quantities. This would likely be due to the presence of chlorine, and subsequent reaction with water producing HCl. An initial background scan of the nitrogen carrier gas through the electrolyte at zero current revealed roughly 170 ppm of water, which later dropped by 100 ppm as a current was passed through the cell. The HCl only started to form when a current was applied but did so at levels roughly between 100-200 ppm. This implies that the water is reacting with the chlorine gas to form HCl. This could be a fluctuation in H_2O originating from the N_2 carrier gas as an impurity along with the O_2, which stays relatively constant throughout the test.

$$H_2O + Cl_2 \rightarrow 2HCl + \frac{1}{2}O_2 \qquad \textit{Eq. 4-17}$$

The chloride peaks are therefore fragments of the HCl seen. The peak at 32 for oxygen can be taken as fluctuating O_2 present in the carrier gas. The 3:1 peak ratio is consistent as both the volume of product gases increase along with the applied current/potential, as the degradation occurs, confirming that these are degradation products. It is also possible that the reduction of imidazolium ions causing the release of hydrogen, which can also react with chlorine forming HCl as in Eq. 4-18. Another theory on the formation of HCl is the reaction of chlorine gas with an imidazole radical Eq. 4-19, although the certainty as to whether the imidazole radical decomposes releasing hydrogen is debated and the fact that these radicals will be present in solution with a limited amount of dissolve chlorine.

$$\frac{1}{2}H_2 + \frac{1}{2}Cl_2 \rightarrow HCl$$ *Eq. 4-18*

$$Emim_{\circ} + Cl_2 \rightarrow 1, ethyl, 2, chloro, 3, methylimidazole + HCl$$ *Eq. 4-19*

From Figure 4-12b, the inset graph shows the increase in current with respect to the cell voltage and the extent of the degradation reaction occurring at larger potentials. The current, calculated from the HCl flowrate assuming 2 electrons required per mole of HCl, provides a glimpse of the progression of this degradation within the electrolyte. The current reveals that the formation of HCl from both the oxidation and reduction limiting reactions of the cell are responsible for all the applied current at potentials of 2.5 V and higher. The molar flowrate of HCl increases as the voltage across the cell increases. The degradation of the electrolyte appears to start at a cell voltage of 2.4 V, with a 2.0 V WE potential, reaching the height of the degradation at a voltage of 2.7 V as the molar flowrate starts to plateau, lower than the windows of up to 4 V seen in previous figures. This can be explained by in-cell aluminium plating taking place, hence a WE potential difference of 2.0 V against chlorine evolution, while in absence of aluminium electrolyte has 4 V stability between imidazolium reduction and chlorine evolution.

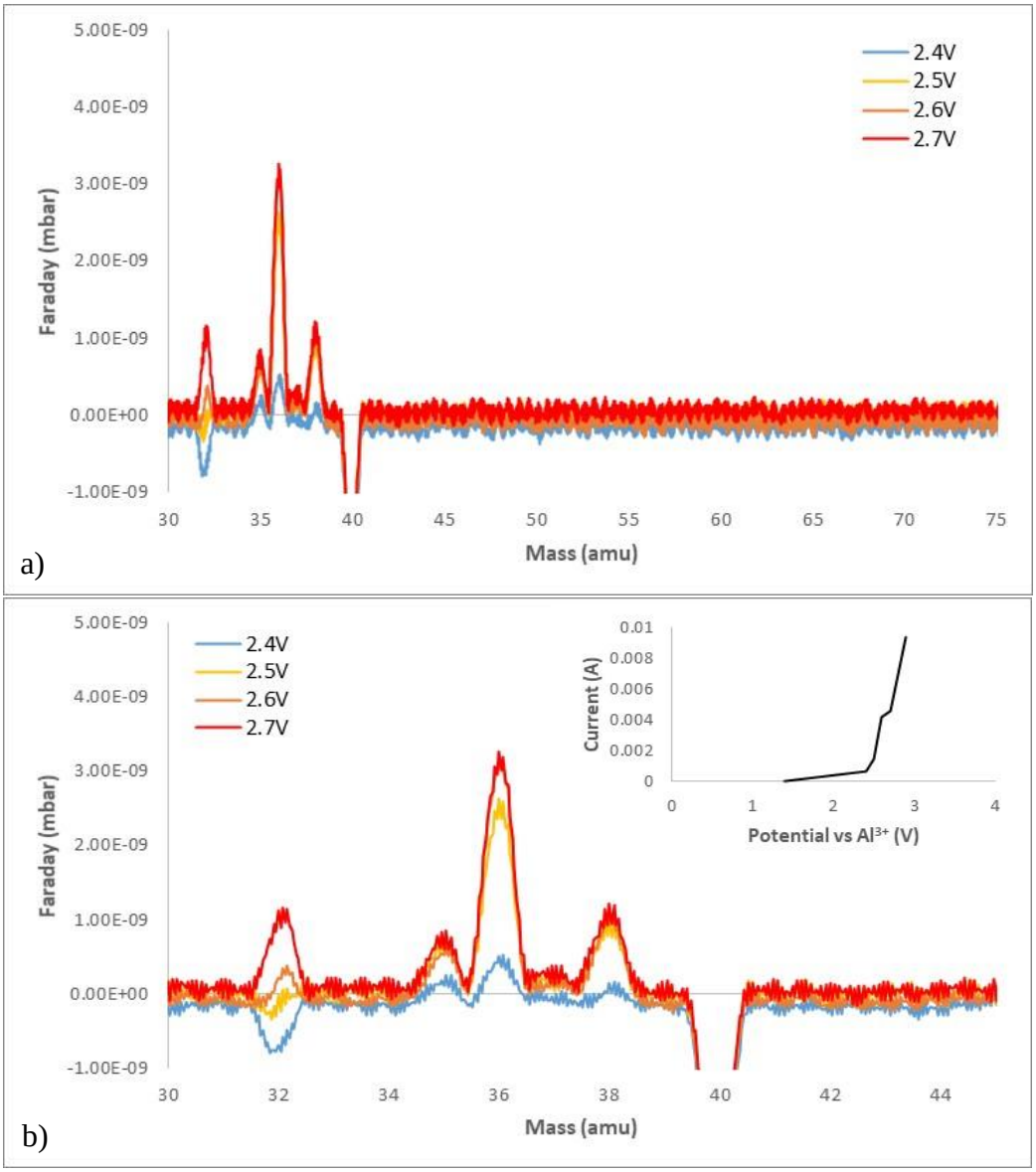

Figure 4-12 - Residual gas analysis spectra of Emic/$AlCl_3$ 1:1.3 electrolyte at various cell voltages (a) mass range 30-75 (b) mass range between 30-45, inset: reaction current against cell voltage

4.3 Aluminium Anode study

To study the effects of stripping and plating aluminium onto different electrode materials in Emic/$AlCl_3$, cells with aluminium counter electrodes were tested around potential of -0.2 V vs Ag/AgCl.

4.3.1 Symmetrical Aluminium Electrodes

4.3.1.1 Electrolyte Ratio Comparison

Beginning with the 1:1 Emic: $AlCl_3$ electrolyte, Figure 4-13 shows an aluminium symmetrical cell. The potential range used was designed to provoke both plating and stripping. From Figure 4-13, it can be seen that aluminium stripping occurs at the working electrode, but no plating takes place as the potential sweeps negative. The only observable reduction is at -2.2 V vs Ag/AgCl at the counter electrode. This is far below the redox for $AlCl_4^-$ and even below the potential for aluminium at -1.9 V vs Ag/AgCl indicating that this is the degradation reaction of imidazolium reduction.

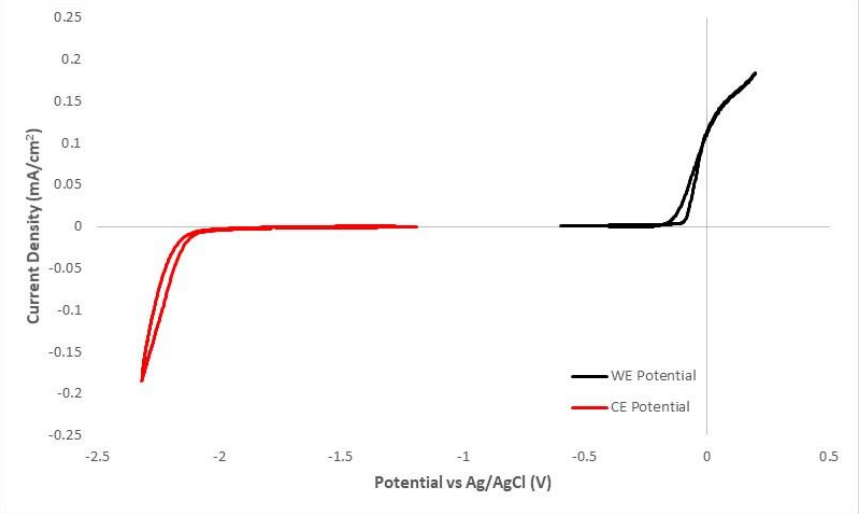

Figure 4-13 – CV of Aluminium WE & CE cell, Emic/$AlCl_3$ 1:1 electrolyte, scanned from -0.6 to 0.2 V at 20 mVs^{-1}

In a neutral electrolyte containing more $AlCl_4^-$ than $Al_2Cl_7^-$ with Al^{3+} fully complexed with Cl^-, the Al/Al^{3+} plating potential shifts further negative (Eq. 4-13) than the cationic reduction potential of the electrolyte due to a very low concentration of $Al_2Cl_7^-$, meaning that plating cannot take place within the electrolyte stability window [91]. An acidic electrolyte with fewer $AlCl_4^-$ ions and more $Al_2Cl_7^-$ ions causes the aluminium plating reaction to shift in the positive direction as the $Al_2Cl_7^-$ ion concentration increases.

An aluminium/ aluminium cell using 1:1.3 Emic/$AlCl_3$ in Figure 4-14 shows reversible reactions of plating and stripping with a lower overpotential from the counter electrode. The larger amount

of $Al_2Cl_7^-$ in the electrolyte has resulted in the plating region to appear with onset potential around -0.2 V. The cell shows a coulombic efficiency of just over 100%. This is explained by experimental error; the stripping potential region of the test was slightly larger than the plating potential region and since both electrodes are a large aluminium source, plating and stripping can continue for a long time regardless of how much was plated or stripped previously. Therefore, a coulombic efficiency cannot be calculated accurately as opposed to when a finite aluminium source is used causing fixed amount of charge/mass in both the plating and stripping regions.

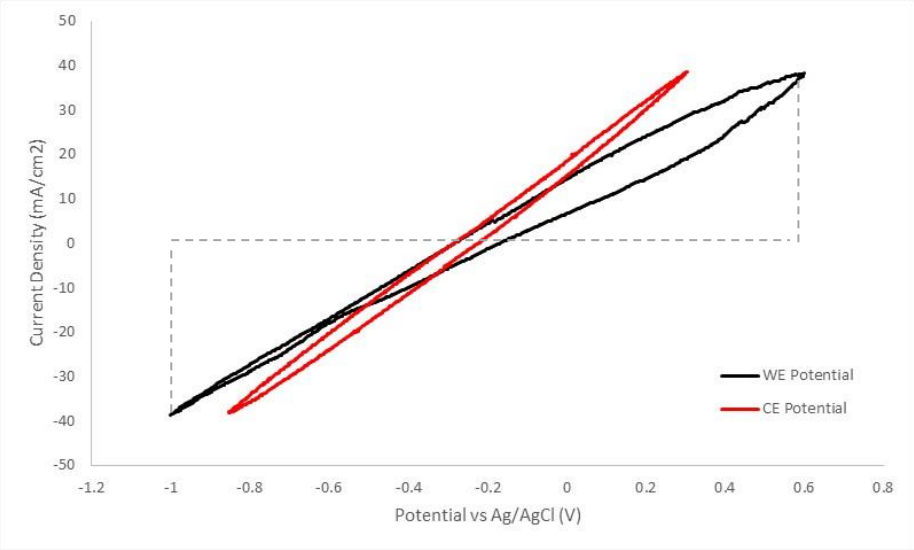

Figure 4-14 – CV of Aluminium WE & CE cell, Emic/$AlCl_3$ 1:1.3 electrolyte, scanned from -1 to 0.6 V at 100 mVs^{-1}

4.3.2 Platinum Working Electrode / Aluminium Counter Electrode

Switching the working electrode for platinum against an aluminium counter in Figure 4-15 and Figure 4-16, the 1st and 2nd voltammetric scans can be seen. Initially scanning positive results in no stripping of the platinum as there is no aluminium to remove however, the main difference when using an aluminium counter electrode with a platinum working electrode is that upon plating the platinum, stripping can occur immediately at the aluminium counter with no limitations due to the practically infinite aluminium source. This is as opposed to the forced degradation reaction involving chloroaluminate oxidation as seen in Figure 4-9. A coulombic efficiency of 96% was obtained from the Figure 4-16 scan.

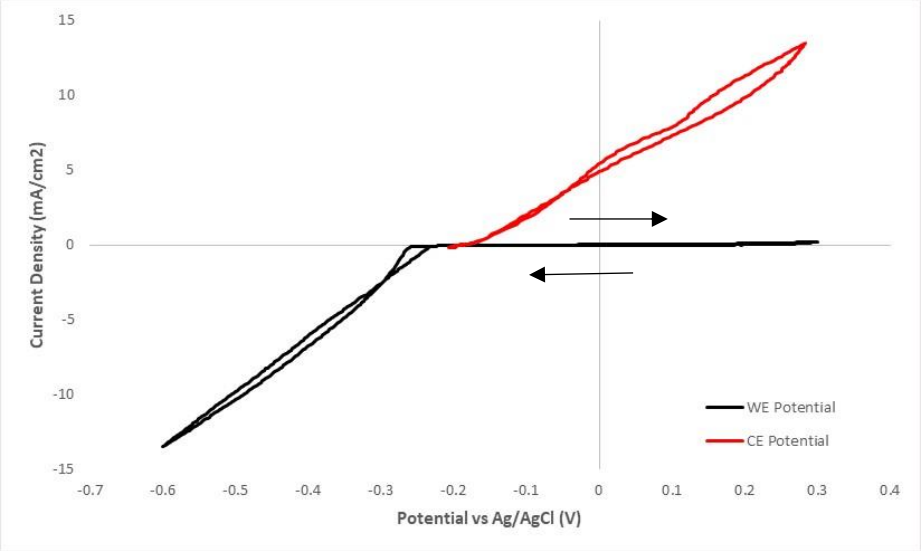

Figure 4-15 – CV of Platinum WE /Aluminium CE cell, Emic/$AlCl_3$ 1:1.3 electrolyte, scanned from -0.6 to 0.3 V at 20 mVs^{-1} 1st scan

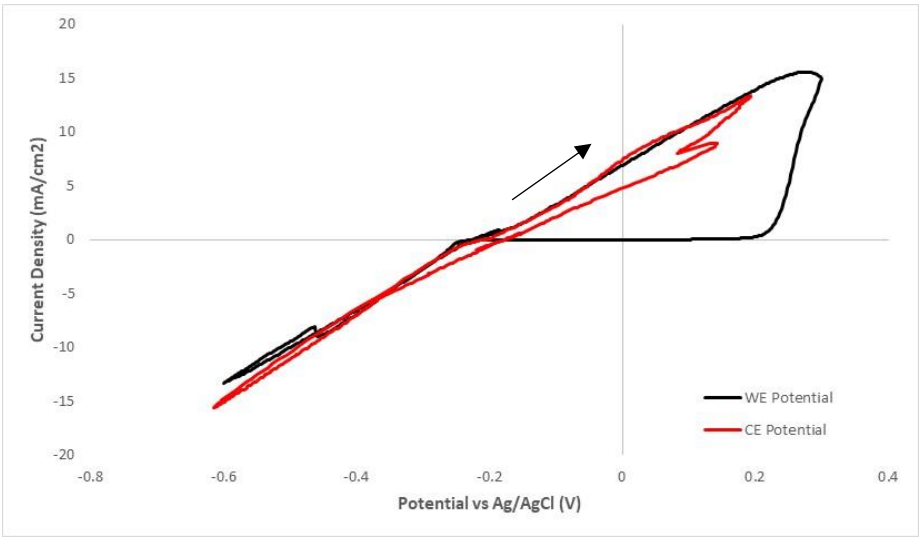

Figure 4-16 – CV of Platinum WE /Aluminium CE cell, Emic/$AlCl_3$ 1:1.3 electrolyte, scanned from -0.6 to 0.3 V at 20 mVs^{-1} 2nd scan

4.3.3 Graphite Working Electrode / Aluminium Counter Electrode

To demonstrate aluminium plating on graphitic materials, two graphite electrodes were compared in different forms. A comparison between a graphite sheet and a reduced graphene oxide powder coating is given; Figure 4-17 and Figure 4-18 show very different voltammograms. This is caused by both differences in surface area and differences in the conductivity of rGO and graphite. Normal plating and stripping are observed when testing the graphite sheet, with limiting currents at both

graphite and aluminium electrodes during plating as well as during stripping due to mass transport of $Al_2Cl_7^-$.

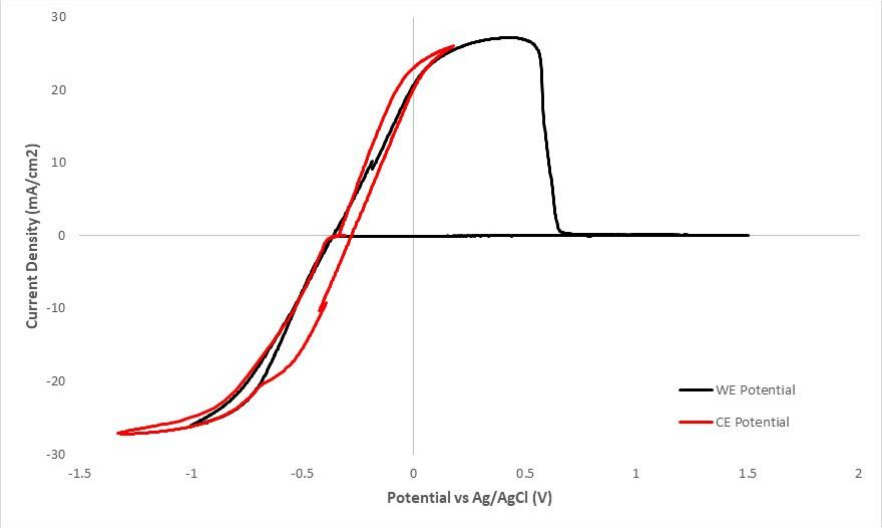

Figure 4-17 – CV of Graphite WE /Aluminium CE cell, Emic/$AlCl_3$ 1:1.3 electrolyte, scanned from -1 to 1.5 V at 50 mVs^{-1}

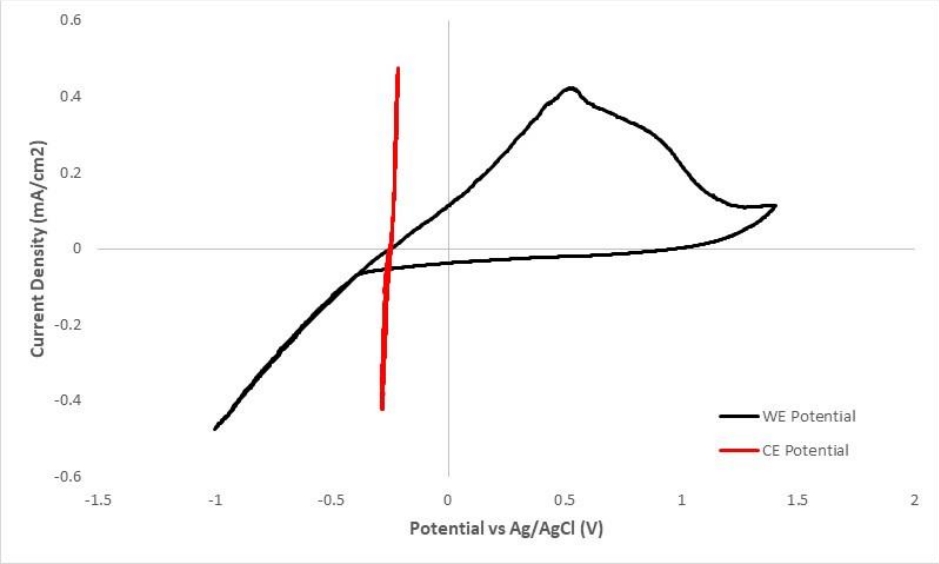

Figure 4-18 – CV of Reduced graphene oxide (rGO) WE /Aluminium CE cell, Emic/$AlCl_3$ 1:1.3 electrolyte, scanned from -1 to 1.5 V at 20 mVs^{-1}

The low current densities of plating and stripping of aluminium on reduced graphene oxide in Figure 4-18 is most likely caused by its powdered form not being conducive to plating and consequently lower active area of electrode. The aluminium counter electrode shows barely any potential change at such low current values. The coulombic efficiencies for the graphite sheet and reduced graphite oxide powder are 92% and 97% respectively, suggesting that coulombic efficiency of stripping and plating is affected by the operating current value. For a cell using a

graphite cathode, aluminium plating doesn't usually occur as the cathode potential is much higher than that required for Al plating, but intercalation will take place at higher potentials >0 V vs Ag/AgCl which will be studied in the next chapter.

4.4 Conclusion

The Emic/PC electrolyte displays a stable potential window of 3 V. In the absence of aluminium chloride, the limiting cathodic reaction is that of reducing $Emim^+$ generating a carbene. The limiting oxidation of chloride ions to chlorine gas can take place without any aluminium present. In a neutral electrolyte, the electrolyte stability window is similar, but the aluminium chloride removes the free chloride ions and the limiting oxidation reaction is caused by the oxidation of chloroaluminate ions releasing chlorine gas. The complexing of the smaller $AlCl_4^-$ anion does not allow for plating of aluminium within the electrolyte stability window, making it unsuitable for battery applications.

More acidic electrolyte ratios generate large concentrations of chloroaluminate ions which degrade at a higher potential than their smaller counterpart by up to 1 V. This increases the window in the positive direction however the ability to plate aluminium in this melt still limits the operating potential window to less than 2.5 V as the plating region shifts positively from a neutral melt up to -0.2 V. The window is further decreased to avoid any degradation to ensure maximum coulombic efficiency of the cell to a safe working voltage of 2.2 V. Degradation was still found to occur regardless of the operating voltage limits, when aluminium plating requires the extraction of aluminium directly from the electrolyte due to the lack of available $Al_2Cl_7^-$ anions, thus showing that the limiting factor in the capacity of chloroaluminate cells is the presence and quantity of the larger $Al_2Cl_7^-$ ion.

Investigation into the efficacy of an aluminium pseudo-reference revealed that a shift of over 1 V takes place during operation of a symmetrical cell and over 100 mV during operation of an asymmetric cell operating at a lower current, as the ratio of chloroaluminate complexes changes in accordance with the Nernst equation. A trade-off is encountered when using a thin separator; the IR losses from ionic transport in electrolyte will decrease as the inter-electrode distance is decreased. However, on the other hand the accompanying decrease in electrolyte volume means the occurrence of rapid change of aluminium species in the electrolyte for a given charge limiting the cells capacity. The ideal cell design would be that of redox flow batteries where the electrolyte can be circulated.

The electrode limiting reaction schemes at each end of the stability window have been debated in literature. Results from this study conclude that the reduction of $Emim^+$ forms a carbene and other reduction products some of which can be partially re-oxidized. Cl_2 gas is produced from the oxidation of chloroaluminate ions. Mass spectrometry showed the release of HCl from the cell as large cell voltages of 2.4 V and above were used. However, no chlorine gas was directly detected but this is believed to be caused by immediate reaction of chlorine gas with humidity traces in the carrier gas forming the detected HCl.

Chapter 5. Characterisation of Positive Electrodes to Investigate Cell Performance

5.1 Introduction

In this chapter the role of a positive electrode on the aluminium-ion battery performance is examined, specifically to look at the suitability of carbon-based electrodes as well as WO_3 and MnO_2. The effect of electrolyte ratios of aluminium chloride in 1-ethyl-3-methylimidazolium chloride will be compared, looking at their charging and therefore support of intercalation. In order to provide insight into chloroaluminate ion intercalation, characterisation of the electrode structure at different states of charge using Raman Spectroscopy, Scanning Tunnelling Microscopy (STM) and X-ray diffraction (XRD) was carried out.

5.2 Effect of Electrolyte Ratio

Both the 1:1 and the 1:1.3 Emic/$AlCl_3$ electrolytes were tested for their ability to enable intercalation in the positive working electrode. This was done using a 3-electrode setup: a working electrode from materials of interest, an aluminium counter electrode to act as an aluminium ion source, and an AgCl reference electrode. A platinum counter electrode was also used in some experiments for comparison.

An internal ferrocene reference was also used to ensure that the reference electrode potentials did not drift significantly due to the corrosivity of the imidazole electrolyte. Ferrocene has a redox potential of 0.45 V vs SHE that equates to around 0.23 V vs Ag/AgCl.

5.2.1 Imidazolium Chloride / Aluminium Chloride 1:1

5.2.1.1 Carbon Black on Glassy Carbon

Figure 5-1 shows the voltammetry of a carbon black working electrode at scan rates of 20, 50, and 100 mVs^{-1} against an Al and a Pt CE. A large redox reaction is seen around 1V which in the presence of a carbon electrode implies that intercalation of aluminium complexes has taken place, and on the reverse scan; de-intercalation has occurred. The half-wave potential of this redox is the same as that of the redox of chloride or chloroaluminate ions at the 1:1 electrolyte anodic limit as seen in the previous chapter, however the peaks here are much broader as the proposed adsorption

reaction continues at higher potentials. The reduction peak is also much larger than that seen in previous chapter and increased with scan rate.

Using multiple scan rates in Figure 5-1 reveals that the reactions are adsorption/desorption controlled processes as the peak current is linearly proportional to the scan rate. The slight shift in the redox peak potential as the scan rate increases indicate that the electron transfer is slow and slightly irreversible or quasi-reversible. The most likely adsorbed/desorbed species is chloroaluminate but adsorption and desorption of chlorine, from chloroaluminate oxidation, is also possible given the high surface area of carbon used.

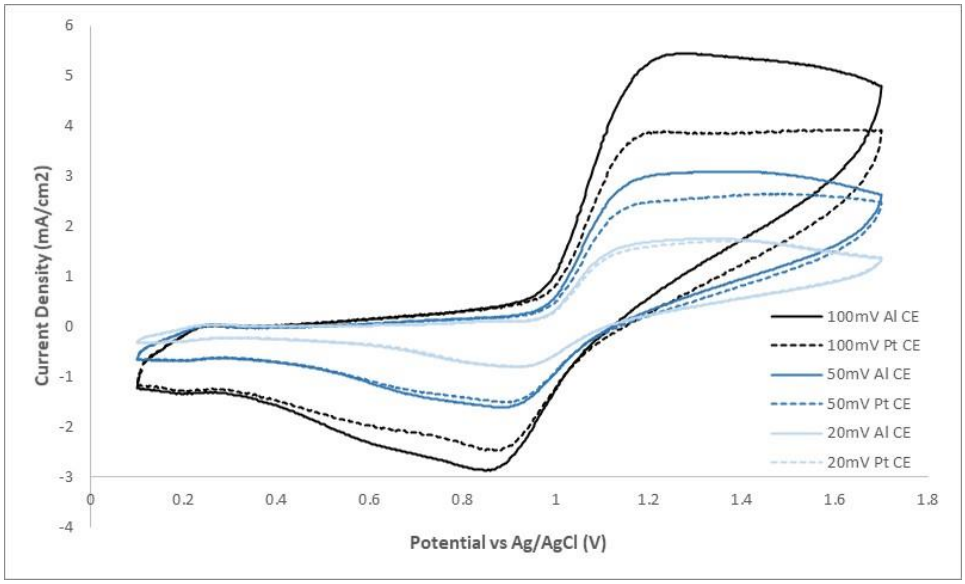

Figure 5-1 – CVs of Carbon Black WE / Aluminium CE (solid) & Platinum CE (dashed) cells, Emic/$AlCl_3$ 1:1 electrolyte, scanned from 0.1 to 1.7 V at 100, 50, & 20 mVs^{-1}

The test was repeated with a platinum counter electrode, as seen by the dashed voltammograms in Figure 5-1, allowing us to see the effect of chloroaluminate adsorption when the main source of aluminium has been taken away. By integrating the anodic and cathodic peaks in Figure 5-1 for Al and Pt CEs, it is interesting to note that the scans were very similar, with coulombic efficiencies of 54% and 61% respectively at 100 mVs^{-1}. Since no Al plating can take place in a 1:1 electrolyte solution as shown previously, the counter electrode must be degrading the electrolyte with the reduction of imidazolium to support adsorption at the working electrode. The oxidation current from 1 to 1.6 V is also likely to be arising from both adsorption of chloroaluminate on carbon black and the chloroaluminate oxidation reaction as seen previously, explaining the low coulombic efficiency seen. The ferrocene reference redox can also be seen around 0.2 V.

5.2.1.2 *Reduced Graphene Oxide on Glassy Carbon*

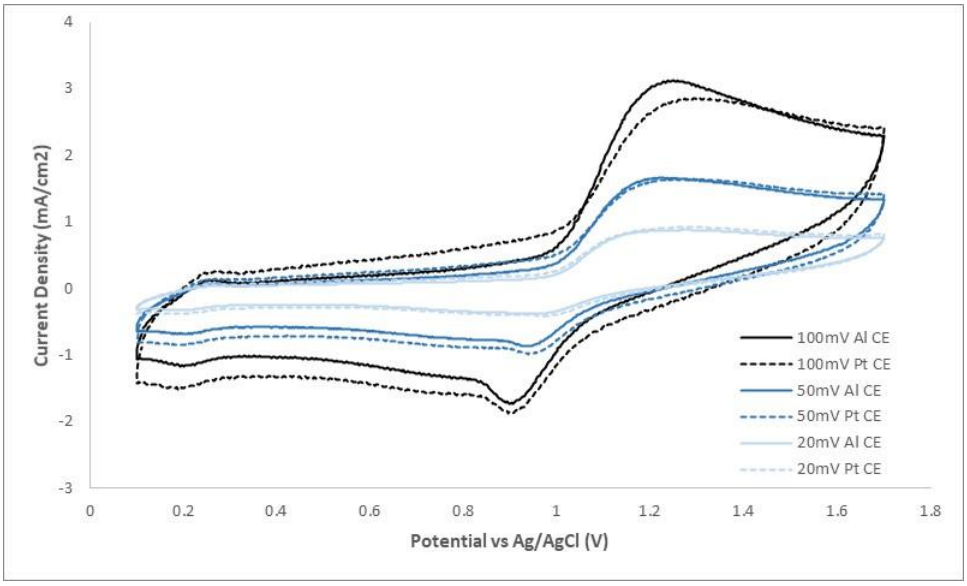

Figure 5-2 – CVs of Reduced graphene oxide WE/ Aluminium CE (solid) & Platinum CE (dashed) cells, Emic/$AlCl_3$ 1:1 electrolyte, scanned from 0.1 to 1.7 V at 100, 50, & 20 mVs^{-1}

Similarly, Figure 5-2 shows cyclic voltammogram of reduced graphene oxide (rGO) in 1:1 Emic/$AlCl_3$ electrolyte with Al and Pt counter electrodes, respectively. It can be seen that the oxidation peak is larger than that of reduction peak with half wave potential also around 1 V. The scan rate shows an almost linear relationship with peak current suggesting the oxidation and reduction reactions seen are adsorption controlled.

The coulombic efficiencies of 60% and 72% at 100 mVs^{-1} are for aluminium and platinum counter electrodes respectively. These values would be lower if the double layer could be accurately removed. The low values of the efficiencies can be explained as above, by oxidation reaction current seen rising from chloroaluminate oxidation to chlorine and possibly adsorption of chloroaluminate on rGO. It has been shown that adsorption and intercalation processes of chloroaluminate of carbon based materials are not 100% reversible [49]. The initial sharp reduction peak at 0.9 V indicates a separate reaction to the broad continuous reduction that follows. Given that the reduction of chlorine gas and other possible oxidation products of chloroaluminate ions take place at the same potential, it is likely that the reaction is taking place simultaneously with possible desorption of adsorbed chloroaluminates from rGO surface. The lower conductivity of rGO compared to carbon could explain why the adsorption/desorption is not as reversible as carbon black or it could be that amounts of adsorbed/desorbed species are lower in comparison and therefore the oxidation/reduction peaks are dominated by $AlCl_4^-$ oxidation and Cl_2 reduction. The

slow desorption between 0.8-0.2 V could be mistaken for the double layer capacitance effect that is also seen around 0.2 V. However, the asymmetric nature of the capacitance on the forward and reverse scans reveals the gradual reduction reaction.

5.2.1.3 Graphite

Figure 5-3 shows cyclic voltammogram of graphite WE with Al CE in 1:1 Emic/$AlCl_3$ electrolyte in a potential window of 0.1-1.6 V vs Ag/AgCl. Oxidation of $AlCl_4^-$ at a graphite electrode occurs at much higher overpotentials than those of rGO and carbon black with an onset potential around 1.2 V. No limiting current is observed before reaching the potential limit of the scan. The corresponding reduction is negligible and is barely visible, beginning around 0.9 V on the reverse scan with coulombic efficiency of about 2% at 100 mVs^{-1}. The small amount of ferrocene present in the electrolyte which is reducing at 0.25 V vs Ag/AgCl is not included in the efficiency calculations. This suggests that as seen in the previous chapter the main reactions taking place here are $AlCl_4^-$ oxidation to chlorine and reduction any soluble chlorine in solution. No adsorption/desorption reactions are taking place in contrast to rGO and carbon black. While the surface area of graphite is lower than carbon black at around <100 m^2g^{-1} to 1000 m^2g^{-1} respectively, which could result in lower adsorption currents, the different nature of carbon also seems to play an important role as will be seen later on. There is also no intercalation and consequently no de-intercalation reactions taking place at the graphite surface because the chloroaluminate oxidation reaction is favoured and any $AlCl_4^-$ intercalated in the graphite will immediately be oxidised to chlorine gas as both reactions take place at same potential range.

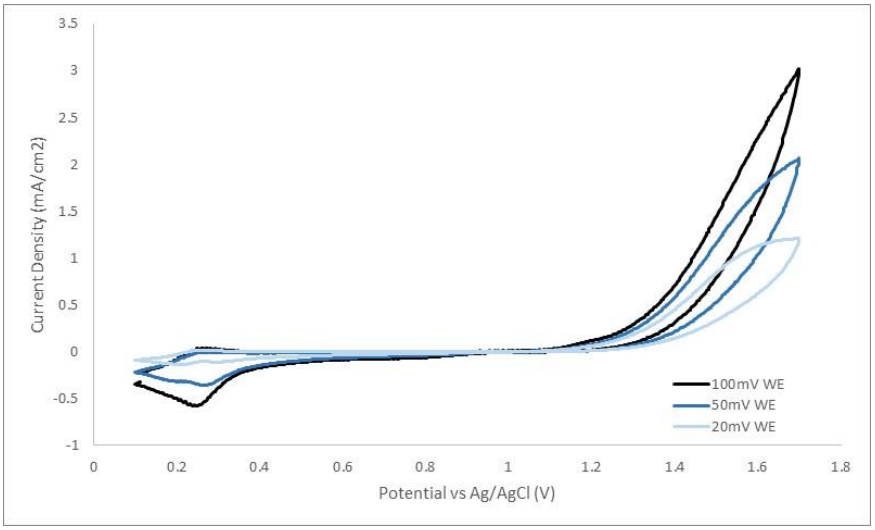

Figure 5-3 – CVs of Graphite WE/ Aluminium CE cell, Emic/$AlCl_3$ 1:1 electrolyte, scanned from 0.1 to 1.7 V at 100, 50, & 20 mVs^{-1}

5.2.1.4 Manganese Dioxide on Glassy Carbon

Figure 5-4 shows cyclic voltammogram of a manganese dioxide electrode WE with Al CE in 1:1 Emic/$AlCl_3$ electrolyte in potential window 0.1-1.7 V vs Ag/AgCl. A sharp oxidation current can be seen with onset potential at 1.1 V vs Ag/AgCl. This is discussed similarly with graphite being caused by oxidation of $AlCl_4^-$ to Cl_2 hence a limited reduction current of dissolved Cl_2 in the electrolyte is seen with a coulombic efficiency of only 12% at 100 mVs^{-1}. The distance between the redox peaks shows a slow electron transfer, much slower than what is expected for a single electron transfer which would present with a theoretical peak to peak separation of 59 mV. Similar to graphite, no adsorption/desorption or intercalation/de-intercalation reactions on MnO_2 surface can be seen in the studied 1:1 electrolyte.

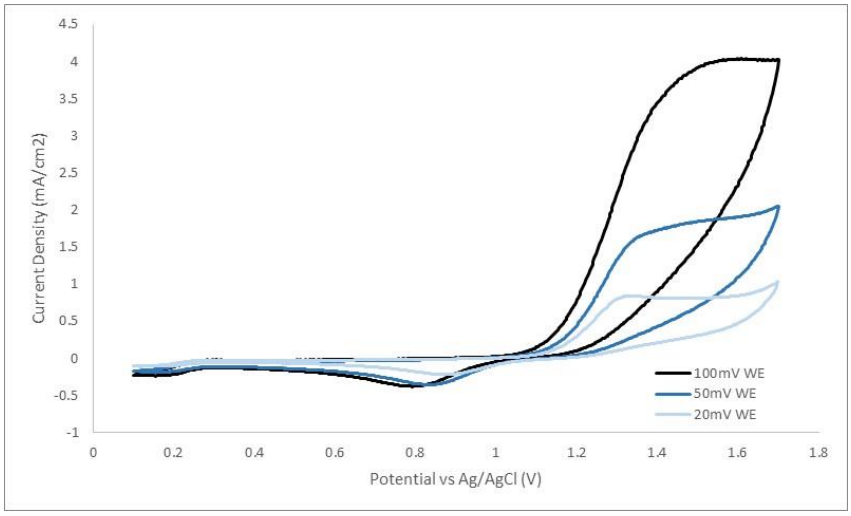

Figure 5-4 - CVs of MnO_2 WE/ Aluminium CE cell, Emic/$AlCl_3$ 1:1 electrolyte, scanned from 0.1 to 1.7 V at 100, 50, & 20 mVs^{-1}

5.2.2 Imidazolium Chloride / Aluminium Chloride 1:1.3

To determine the onset of $AlCl_4^-$ oxidation and the degradation of the 1:1.3 electrolyte, cyclic voltammograms were studied for each cathode material, increasing the potential window systematically from 1.5 V to 2.1 V with 100 mV increments. The onset of oxidation reactions will be observable as will any reduction reactions that result from those oxidation reactions if they are reversible. Any irreversible or quasi-reversible reactions will be considered to be arising from electrolyte degradation reactions.

5.2.2.1 Carbon Black on Glassy Carbon

When using a higher ratio of Emic/$AlCl_3$ than 1:1 this will make the electrolyte more acidic with formation of $Al_2Cl_7^-$ ions (Eq. 4-9). $Al_2Cl_7^-$ supports Al plating at the anode but also increases electrolyte oxidation stability causing the chlorine evolution reaction not to be seen below potentials of 2 V vs. Ag/AgCl. This is expected to play a large role in improving the competitiveness between chlorine evolution and $AlCl_4^-$ adsorption and intercalation reactions. Figure 5-5 and Figure 5-6, show voltammograms of carbon black in 1:1.3 Emic/$AlCl_3$ electrolyte with Al and Pt counter electrodes respectively. Although the observed current densities are lower than those seen in the 1:1 electrolyte, this can be explained by a lower concentration of the adsorbed and oxidised $AlCl_4^-$ ion. With the separation of $AlCl_4^-$ oxidation above 1.8 V from that of adsorption/desorption between 0.5 and 1.8 V, the linear relationship between scan rate and adsorption/desorption peaks confirms that the process seen is adsorption/desorption limited. At around 1.55 V in Figure 5-5 and similarly just below 1.5 V in Figure 5-6, the current drops due to the adsorption of $AlCl_4^-$ no longer taking place as the potential increases, instead the current relies on the oxidation of $AlCl_4^-$, reaching a peak at the potential limit. The coulombic efficiency in the $AlCl_4^-$ adsorption/desorption region is also about 90%. This supports the conclusion above that the low coulombic efficiency seen in 1:1 electrolyte was caused by oxidation and adsorption reactions taking place at same potential range.

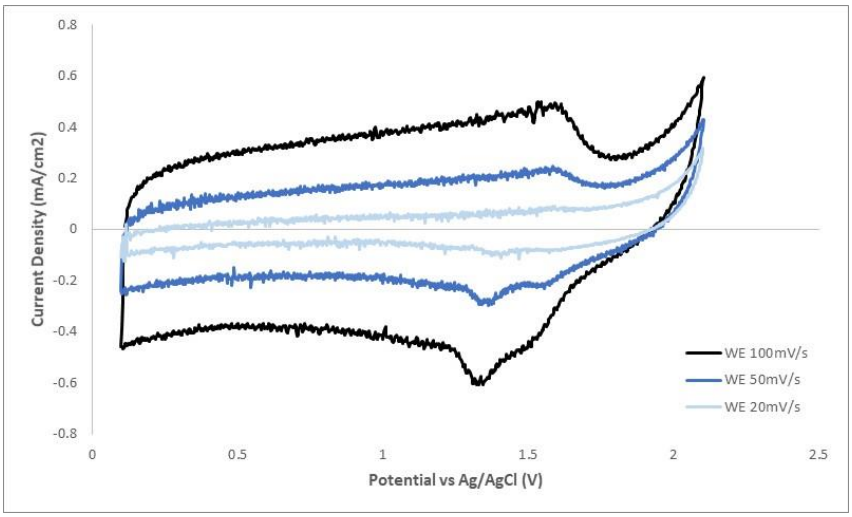

Figure 5-5 – CVs of Carbon Black WE/ Aluminium CE cell, Emic/$AlCl_3$ 1:1.3 electrolyte, scanned from 0.1 to 2.1 V at 100, 50, & 20 mVs^{-1}

In addition to the supercapacitor behaviour of carbon black from the $AlCl_4^-$ adsorption/desorption charge, the flat, low currents in potential range of 0.5 to 0.2 V along with the different scan rates

show the double layer effect, due to the high surface area of carbon black acting more like a capacitor, holding a charge rather than intercalating with a capacitance of 3.37 $x10^{-3}$ Fg^{-1} obtained from 100 mVs^{-1} scan.

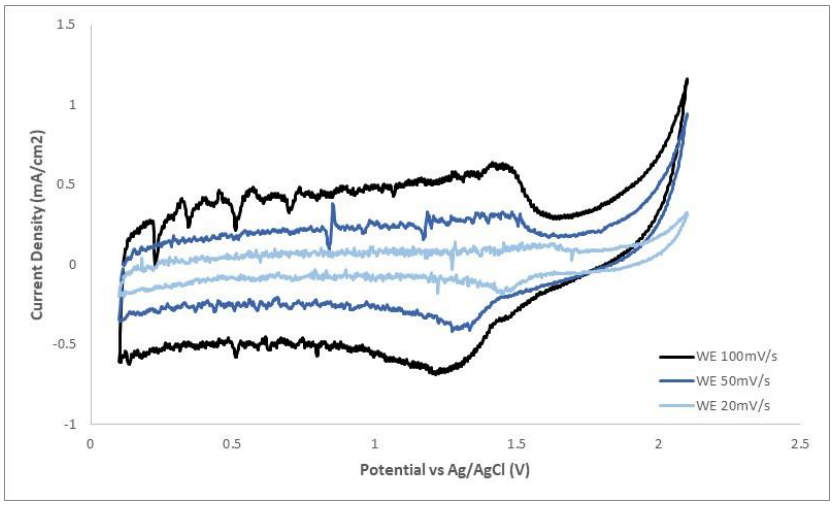

Figure 5-6 – CVs of Carbon Black WE/ Platinum CE cell, Emic/$AlCl_3$ 1:1.3 electrolyte, scanned from 0.1 to 2.1 V at 100, 50, & 20 mVs^{-1} (Noise due to equipment)

The use of a platinum counter electrode in Figure 5-6 has negatively shifted the onset potential of the electrolyte oxidation by around 150 mV. This is because with a platinum counter, Al stripping reaction which consumes $AlCl_4^-$ (Eq. 4-10) is not possible to support desorption of $AlCl_4^-$ from the carbon surface. Instead $Emim^+$ reduction takes place at the Pt counter electrode therefore resulting in an increase in $AlCl_4^-$ concentration in the electrolyte or effectively lowering the 1:1.3 ratio and consequently shifting the $AlCl_4^-$ oxidation potential to lower values. Figure 5-7 shows the same carbon WE/ Al CE cell in 1:1.3 electrolyte but with an incrementally increasing anodic potential limit. The coulombic efficiency of the $AlCl_4^-$ adsorption region between 0.2-1.6 V is 98%. Despite the double layer capacitance present, this shows that the $AlCl_4^-$ adsorption/desorption process is very reversible. The efficiency decreases to 91% as the anodic limit is extended to 2.1 V as chloroaluminate oxidation occurs.

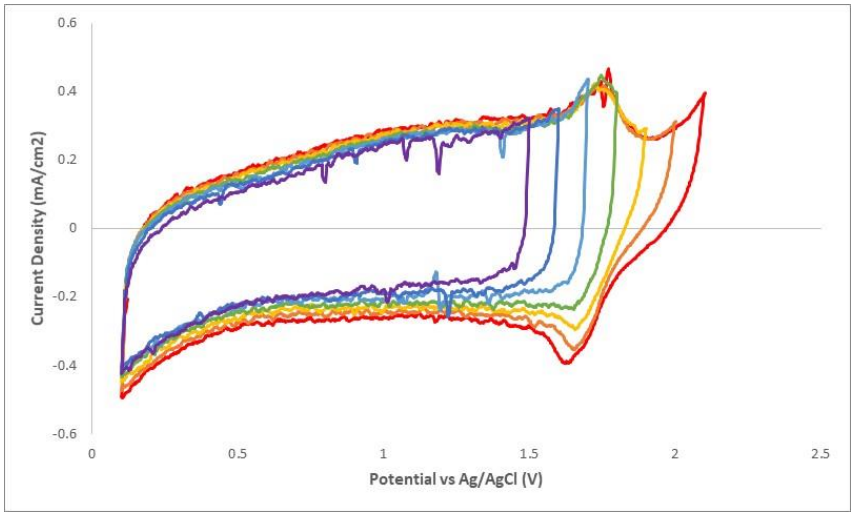

Figure 5-7 - CVs of Carbon Black WE/ Aluminium CE cell, Emic/$AlCl_3$ 1:1.3 electrolyte, scanned from 0.1V to increasing anodic potential limit of 1.5-2.1 V at 50 mVs^{-1}

5.2.2.2 Reduced Graphene Oxide on Glassy Carbon

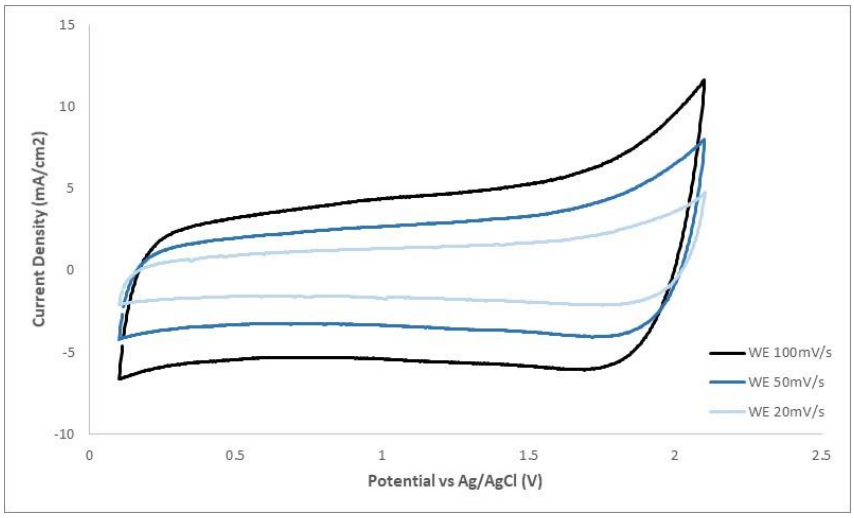

Figure 5-8 – CVs of Reduced graphene oxide WE/ Aluminium CE cell, Emic/$AlCl_3$ 1:1.3 electrolyte, scanned from 0.1 to 2.1 V at 100, 50, & 20 mVs^{-1}

Figure 5-8 shows cyclic voltammogram of a rGO WE with Al CE in 1:1.3 electrolyte. Much higher capacitive currents are observed when using rGO compared to carbon black. The double layer present is almost an order of magnitude higher for a given scan rate giving a capacitance of 4.54 $x10^{-2}$ Fg^{-1}. The double layer capacitance is affected by both the specific surface area of materials and surface nature. BET analysis of rGO gave a surface are of 60 m^2g^{-1}. Since rGO surface is highly oxygenated, this can contribute to the higher double layer capacity seen. It is unclear from the

obtained voltammogram whether adsorption or intercalation has taken place in the rGO due to absence of clear oxidation/reduction peaks. The minor reduction peak seen between 2-1.6 V could be from the reduction of dissolved chlorine formed during the anodic sweep, although it was shown in previous chapter that chlorine evolution was not seen at visible current densities below 2 V in the 1:1.3 electrolyte.

Figure 5-9 shows the same rGO WE, Al CE cell with the anodic potential limit of the rGO WE increased from 1.5-2.1 V in 100 mVs^{-1} steps showing a steady increase in the oxidation reaction. This gradual increase does not fit with the sudden onset of a chloride oxidation peak and could indeed be caused by small amount of $AlCl_4^-$ adsorption or intercalation masked within the double layer current. The shape of the voltammogram is more rectangular and therefore closer to an ideal capacitor. It can then be concluded that limited adsorption or intercalation of $AlCl_4^-$ has taken place on rGO in the 1:1.3 and 1:1 electrolytes.

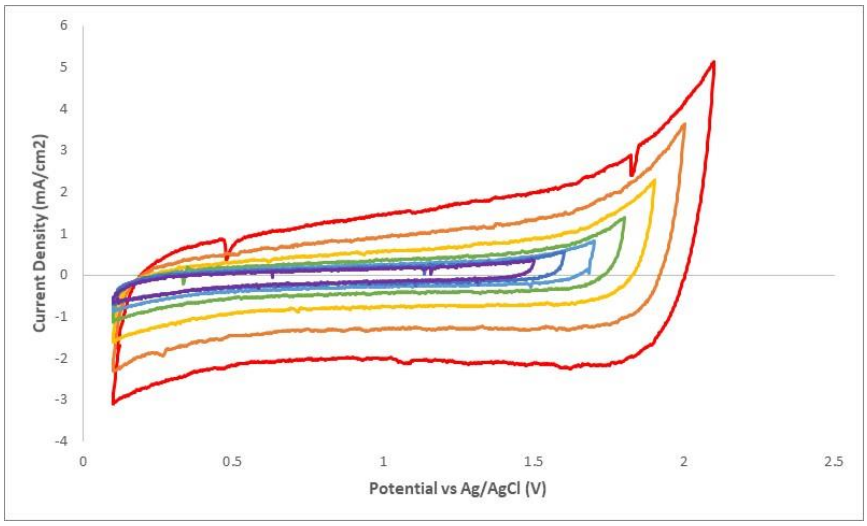

Figure 5-9 - CVs of Reduced Graphene Oxide WE/ Aluminium CE cell, Emic/$AlCl_3$ 1:1.3 electrolyte, scanned from 0.1V to increasing anodic potential limit of 1.5-2.1 V at 50 mVs^{-1}

5.2.2.3 Graphite

Figure 5-10 shows cyclic voltammogram of a graphite WE with Al CE in the 1:1.3 electrolyte in the potential window of 0.1-2 V vs Ag/AgCl. The large size of reduction peak seen suggests that the onset of intercalation is taking place at 1.5 V. The coulombic efficiency is calculated to be 57%. This suggests that either the intercalation reaction is not 100% reversible or that at the studied potential window up to 2 V, chlorine evolution starts to occur at in small quantities.

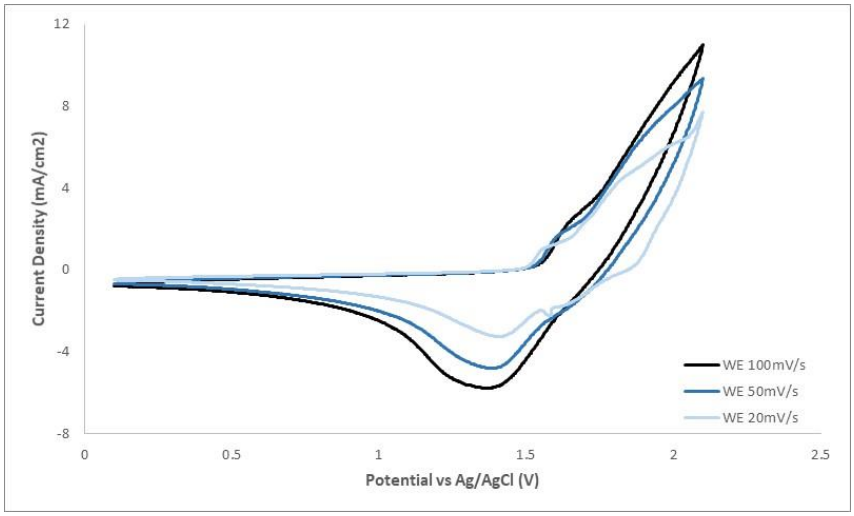

Figure 5-10 – CVs of Graphite WE/ Aluminium CE cell, Emic/$AlCl_3$ 1:1.3 electrolyte, scanned from 0.1 to 2.1 V at 100, 50, & 20 mVs^{-1}

The multiple oxidation peaks seen in Figure 5-10 at 1.5-1.6 V and 1.6-1.8 V at 20 mVs^{-1}, could suggest that two different intercalation reactions are taking place possibly depending on different graphitic sites. No drastic decrease in potential at the counter electrode was observed to indicate imidazolium reduction in response to an oxidation degradation reaction at the working electrode when the WE potential range was 1.5-1.9 V. This supports the argument that this could be caused by multi-stage intercalation [93]. Dong et al. reports of multiple oxidation and reduction peaks during the charging of expanded graphite with the first oxidation peak at around 1.6 V vs $Al/Al_2Cl_7^-$ caused by the adsorption of $AlCl_4^-$ ions upon the graphite electrode, and the second peak due to $AlCl_4^-$ intercalation around 2.3 V [31]. The sharp rise in current above 1.9 V can possibly indicate the start of chlorine evolution reaction from $AlCl_4^-$ oxidation. Figure 5-11 shows 100 mV increments in the anodic potential limit of the graphite WE. This gradual increase of the potential limit in Figure 5-11 shows the gradual growth of the reduction reaction in response to the larger oxidation reaction. The coulombic efficiency steadily decreases from 96% at 1.9 V as the potential limit increases. This could either be due to the increased stage of $AlCl_4^-$ ion intercalation which becomes increasingly difficult to de-intercalate, possibly irreversible, or it could also be caused by the increase of chlorine evolution side reactions, especially above 1.9 V.

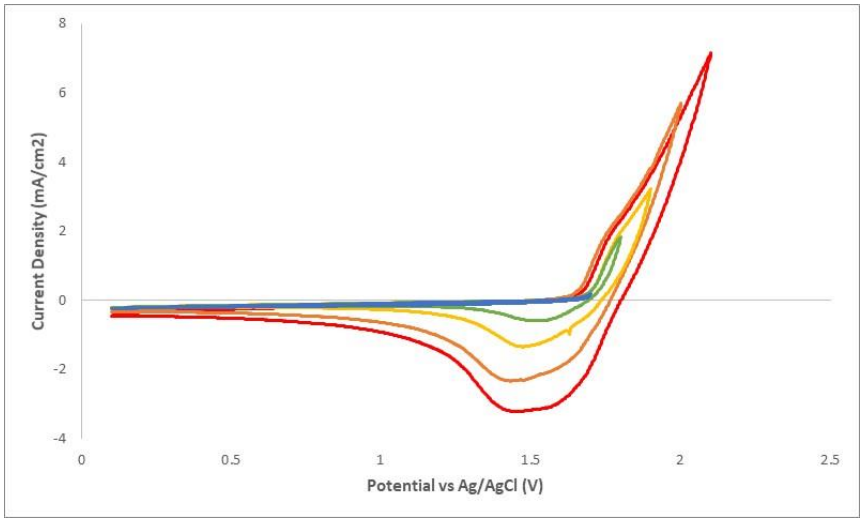

Figure 5-11 – CVs of Graphite WE/ Aluminium CE cell, Emic/$AlCl_3$ 1:1.3 electrolyte, scanned from 0.1V to increasing anodic potential limit of 1.7-2.1 V at 50 mVs^{-1}

5.2.2.4 Tungsten Trioxide on Glassy Carbon

Tungsten (VI) oxide has been successfully used as a working electrode to intercalate Al^{3+} ions in aqueous systems [13, 94] providing stable specific capacities over 200 $mAhg^{-1}$. More recent reports of use in Emic/$AlCl_3$ 1:1.3 electrolyte show intercalation of $AlCl_4^-$ [71] achieving capacities of 68 $mAhg^{-1}$.

Figure 5-12 shows cyclic voltammogram of a WO_3 working electrode with an Al CE in 1:1.3 electrolyte run in a potential window of 0.1-2 V vs Ag/AgCl. Figure 5-13 shows similar voltammogram but with incremental increase of the anodic limit of the scan at 20 mVs^{-1}.

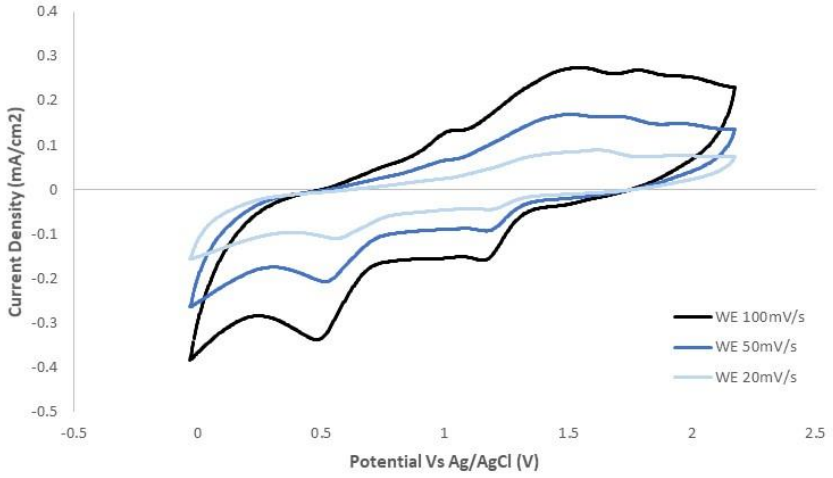

Figure 5-12 – CVs of WO_3 WE/ Aluminium CE cell, Emic/$AlCl_3$ 1:1.3 electrolyte, scanned from 0.1 to 2.1 V at 100, 50, & 20 mVs^{-1}

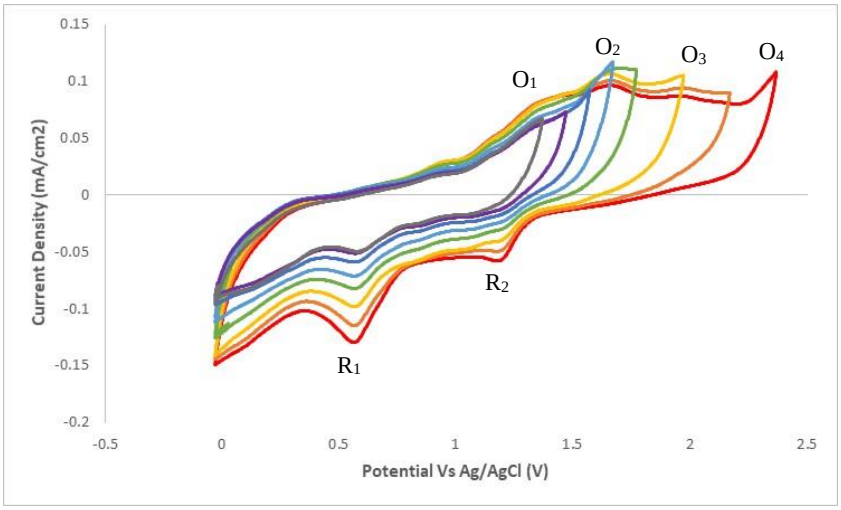

Figure 5-13 – CVs of WO_3 WE/ Aluminium CE cell, Emic/$AlCl_3$ 1:1.3 electrolyte, scanned from 0V to increasing anodic potential limit of 1.4-2.4 V at 20 mVs^{-1}

The multiple redox reactions observed in both Figure 5-12 and Figure 5-13 can be assigned to valence state changes of tungsten redox couples, (O_1/R_1) and (O_2/R_2) in Figure 5-13. These reactions are possibly the redox reactions of W^{5+}/W^{4+} and W^{6+}/W^{5+} respectively, albeit higher than their standard redox potentials. Above 2 V, O_4 in Figure 5-13 depicts a rapid increase in oxidation current which can be assigned to chloride oxidation. The oxidation peak O_3 is irreversible and no direct reduction peak was associated with it, but it can be seen from Figure 5-13 that it resulted in an increase in size of reduction peaks of R_1 and R_2. The larger the potential limit, the greater the reduction current, which would indicate that limited intercalation takes place at higher potentials alongside the degradation reactions leading to greater de-intercalation.

Tungsten trioxide may be a possible host for Al^{3+} or $AlCl_4^-$ intercalation, but not in this case. Negligible intercalation, low current densities, and a specific capacity of 5 $mAhg^{-1}$ make this a poor material choice. This might be caused by a combination of a low surface area of around 60 m^2g^{-1}, a high molecular weight in comparison to carbon, and low electrical conductivity reducing the effectiveness of the material. The use of WO_3 nanorods may be the answer to $AlCl_4^-$ intercalation [71] with evidence to suggest that intercalation takes place in between the ordered WO_3 nanorods in a similar way to that of graphite intercalation, utilising the layered structure of the nanorods. Further testing of tungsten (VI) oxide's potential for battery use will be explored later with XRD.

5.2.2.5 Manganese Dioxide on Glassy Carbon

Figure 5-14 shows cyclic voltammetry of a MnO_2 WE with Al CE in 1:1.3 electrolyte in a potential window of 0.1-2 V vs Ag/AgCl. No significant oxidation or reduction peak can be seen between 1.9 V and 0.15 V. A sharp oxidation current at potentials >2 V vs Ag/AgCl can be assigned to $AlCl_4^-$ oxidation.

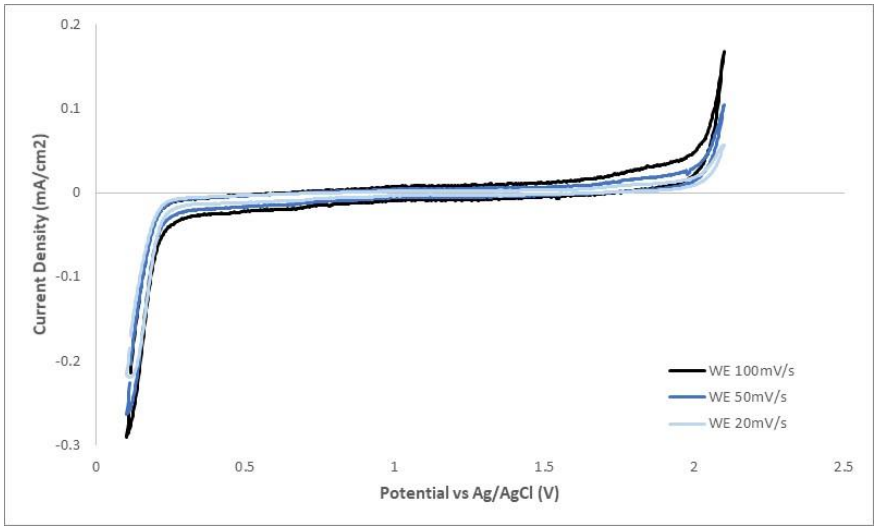

Figure 5-14 – CVs of MnO_2 WE/ Aluminium CE cell, Emic/$AlCl_3$ 1:1.3 electrolyte, scanned from 0.1 to 2.1 V at 100, 50, & 20 mVs^{-1}

Aside from a very small double layer effect of 8.29 $x10^{-5}$ Fg^{-1} at 100 mVs^{-1}, the reduction current at 0.1 V vs Ag/AgCl is anomalous, having not appeared previously with other materials. Therefore, this is most likely to be a reduction of the manganese oxide given that the reduction potential for the change in oxidation state of manganese from Mn^{4+} to Mn^{2+} is around 1.0 V vs Ag/AgCl. Reduction of Mn^{4+} to Mn^+ could also be possible. Newly published literature using δ-MnO_2 as a cathode reported intercalation of $AlCl_4^-$ achieving higher current densities [95]. However, the MnO_2 was composited with carbon, and graphite paper was used as the current collector. As

previously discussed, graphite intercalated $AlCl_4^-$ reversibly and carbon has capacitive qualities, a combination of which are shown in results by Almodovar et al. From this, it can be determined that MnO_2 doesn't offer any reasonable performance to AIBs, or it could be that good performance is due to the phase of MnO_2.

For metal oxides to be doped with an anion, the crystal lattice would need to have available sites. Oxygen ions can be removed from their sites creating oxygen vacancies, which allow for ions to be inserted into the material's structure. The metal ion then oxidises to maintain charge neutrality, written below where 'M' and 'O' represent the metal species and oxygen respectively.

$$M_M^X + yO_O^X + X' \rightarrow M_M^\bullet + (y-1)O_O^X + O_i'' + X_O^\bullet + e'$$

The larger $AlCl_4^-$ anion using the same mechanism would replace an oxygen ion with $AlCl_4^-$. Spinels materials, possessing both tetragonal and octahedral sites in its lattice, could theoretically accept ions into either void space. However, insertion into the crystal structure depends on the size of the ions being introduced and $AlCl_4^-$ is a lot larger at 5.28 Å. Oxygen vacancies have been found to be smaller than the oxygen ion that was present, at 1.16 Å decreased from 1.4 Å [96], meaning that it is not plausible for oxygen vacancies to accommodate the larger $AlCl_4^-$ ion into the lattice.

5.2.2.6 Material Performance Comparison

A direct comparison of the cathode materials studied is shown in Table 5-1 below. It can be seen that the carbonaceous electrodes performed far better than the metal oxides. This is due to the ordered structure and the graphitic layers of carbon-based materials, the higher surface area, and the higher electrical conductivity. From the specific capacity of manganese (IV) oxide, in tandem with the voltammetry above, it is evident that this material does not perform well on its own as an electrode for the purpose of intercalation. Due to these factors, the efficiency of charge due to intercalation from the voltammetric scan if any cannot be reliably calculated. The same can be said of reduced graphene oxide which presents predominantly with a double layer capacitance, meaning any efficiency taken from this CV would be meaningless. The potential limits for both rGO and MnO_2 electrodes are therefore not applicable if no intercalation can be observed. The second metal oxide, tungsten (VI) oxide gave a smaller specific capacity than MnO_2, but a higher efficiency as fewer side reactions skewed the results when the oxidation potential is limited to 1.7 V. Beyond this potential the efficiency decreased due to irreversible oxidation reactions including intercalation. While lower voltages than 1.9 V vs Ag/AgCl can be chosen this would result in significant decrease in capacity and importantly the power density of the battery. The optimum

potential limit chosen to avoid unnecessary side reactions of 1.9 V will undoubtedly limit the cell's overall voltage but in the case of carbon-based materials, the comparatively larger storage capacity due to intercalation can compensate for the lower voltage.

Table 5-1 – Material comparison of specific capacities, coulombic efficiencies from CVs at the optimum cathode potential limit. (*Taken from cell cycling data in section 6.2)*

	Specific Capacity ($mAhg^{-1}$) *	Coulombic Efficiency (%)	Potential Limit (V)
Carbon Black	56	60	1.9
Reduced Graphene Oxide	36	>100	-
Graphite	295	96	1.9
Manganese (IV) Oxide	7.6	-	-
Tungsten (VI) Oxide	4.8	>100	-

While carbon black provides a specific capacity larger than rGO due to differences in atomic structure, graphite has a much larger specific capacity. The coulombic efficiencies for carbon black and graphite are 60% and 96% respectively. As discussed above this is due to intercalation reaction in graphite but adsorption reaction in carbon black. This shows the significant effect of the carbon structure on cathode performance in Al-ion batteries and will be probed further below using XRD, Raman spectroscopy, and STM.

5.3 Effects of Intercalation on Electrode Structure

Initial tests have revealed how carbonaceous materials as well as a few select metal oxides perform as a positive electrode in an aluminium ion battery. The next step is to characterise the electrodes in order to observe why some materials performed well and why some did not. XRD, Raman, and STM have been carried out so that any intercalation can be confirmed through the change in structure of the electrodes.

5.3.1 X-Ray Diffraction

Ex-situ XRD was carried out on graphite and reduced graphene oxide to study the large difference between performance and how the structures either support or hinder $AlCl_4^-$ intercalation. Tungsten (VI) oxide was also chosen to observe the potential structural changes due to intercalants. Pristine, charged, and discharged samples were tested for each material to study the effect of charging on sample structure.

5.3.1.1 Graphite

Figure 5-15 shows the XRD diffraction pattern of graphite at different states of charge at 2θ 10-60° range. From the diffraction pattern of graphite charged to 2.1 V vs Al wire, a distinct change of the 002 plane can be seen. The peak visible in both the pristine and discharged diffraction pattern at 2θ 27° has split into two peaks that have separated in both directions: peaks at 2θ 25.4° and 2θ 28.4°. This splitting indicates both expansion and contraction of the host lattice due to intercalation in between select layers, as d-spacing of the split peaks at 2θ 25.4° and 2θ 28.4° work out to be 3.50 Å and 3.14 Å respectively. The peak at 2θ 25.4° presents with increased width indicating the increase in disorder from a pristine state. The d-spacing of the 002 plane in the pristine sample at 2θ 27° is calculated to be 3.29 Å which is similar to literature values for the interlayer spacing of pristine graphite of 3.35 Å [80]. The peak splitting also correlates to a study by Zhang et al. investigating various states of charge with respect to the intercalant staging [80]. Comparing Figure 5-15 to Zhang's results, the peak splitting closely resembles the initial charging stage at the onset of $AlCl_4^-$ intercalation. Charging to a higher potential at the risk of degrading the electrolyte would increase the level of $AlCl_4^-$ intercalation.

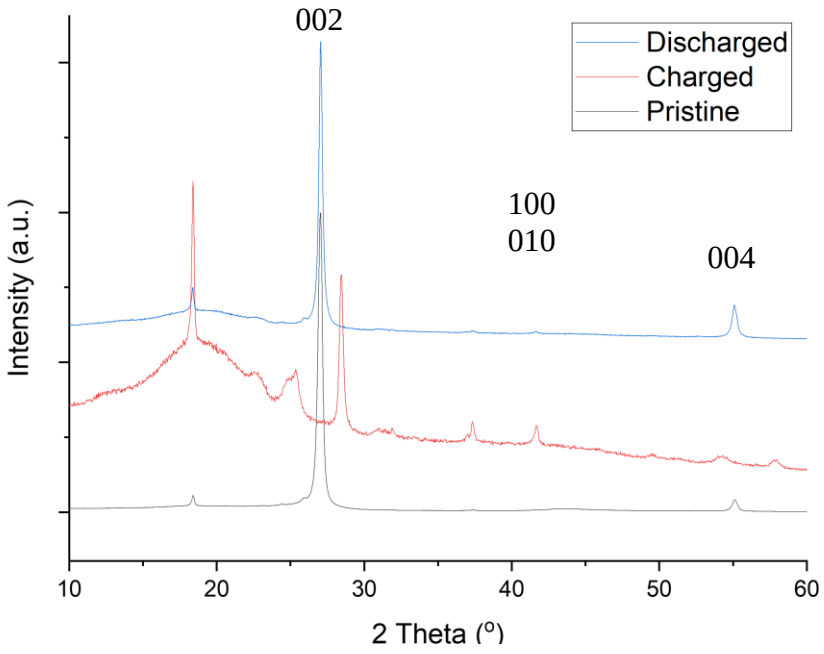

Figure 5-15 - XRD patterns of Graphite at 1.2 V, 2.1 V, and pristine states at 2θ 10-60° range

Using Zhang's method to calculate the intercalation gallery height, a repeat distance of 30.24 Å and an intercalation gallery height of 4.66 Å are calculated. This is smaller than the size of an $AlCl_4^-$ ion at 5.28 Å, yet with a calculated staging of 9, the graphite layers only accommodate one $AlCl_4^-$ ion every 9 graphite layers as the empty layers remain 3.29 Å apart or contract to accommodate the expansion of a single layer. The 8 empty layers plus the intercalant gallery height of 4.66 Å add up to 30.08 Å, very similar to the calculated repeat distance. Increased charging of the cell would result in a higher degree of intercalation but would coincide with $AlCl_4^-$ degradation.

Reduced intensities of the discharged compared to the pristine graphite diffraction pattern reveal some irreversibility in the intercalation as the structure isn't returned to normal after de-intercalation. This is due to the large expansion and contraction of the graphitic layers to house the intercalant. This is in agreement with lower than 100% coulombic efficiency seen above. The lifetime of a battery using a graphite electrode would be severely shortened compared to a lithium-ion battery due to the smaller size of a Li^+ ion compared to the comparably large $AlCl_4^-$.

5.3.1.2 Reduced Graphene oxide

Figure 5-16 shows the XRD diffraction pattern of rGO at different states of charge at 2θ 10-60° range. The 002 plane at 2θ 25° diplays as a broad peak for rGO in Figure 5-16. The peak breadth represents the amorphousness and disorder of the samples structure. The broad 002 plane roughly

gives a d-spacing of 3.55 Å for pristine rGO which is close to the obtained 3.29 Å spacing for pristine graphite considering the breadth of the peak. The charged 002 plane however is not defined enough to calculate d-spacing as the intensity reduces, while the 002 plane returns to an amorphous phase upon discharge. No splitting is seen for the 002 peak confirming no interculataion took place. From the 111 peak at 2θ 37°, d-spacing changes from 2.41 Å – 2.39 Å from pristine to charged as a slight contraction during charge is observed, potentially due to adsorption of $AlCl_4^-$ on the material surface.

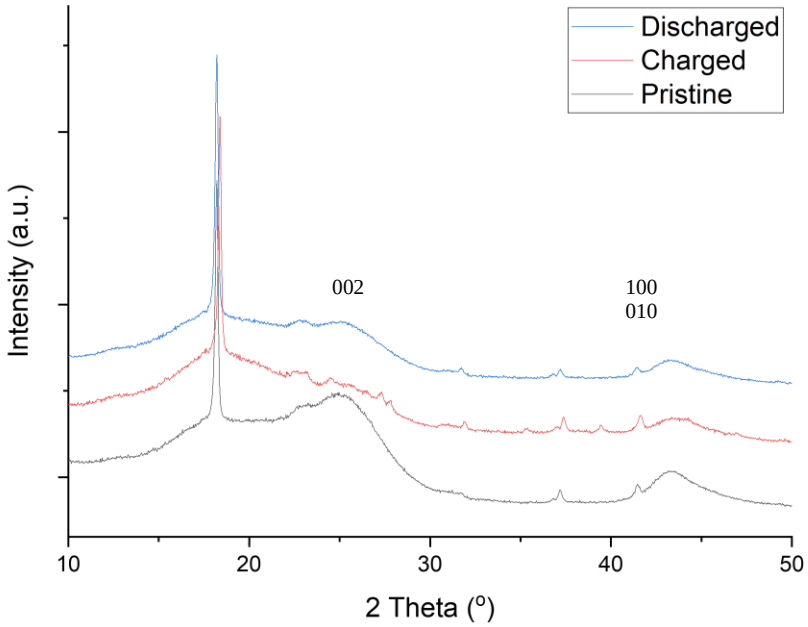

Figure 5-16 - XRD patterns of rGO at 0.5 V, 2.2 V, and pristine states at 2θ 10-50° range

5.3.1.3 Tungsten (VI) Oxide

For WO_3, the XRD diffraction pattern in Figure 5-17 shows a small positive shift in the 2θ angle from pristine to charged states resulting in a d-spacing change of 3.63 Å to 3.59 Å respectively. Upon discharge the spacing increases beyond the original value of 3.63 Å to 3.67 Å. The reduction of WO_3 via cell discharge has inevitably changed the crystal structure and at 2θ 23.5° it can be seen that the 210 plane has disappeared from the discharged diffraction pattern. This along with the suppression of the 200 plane and the growth of the 202 plane at 2θ 33.5° indicate a phase change from β-WO_3 to α-WO_3 [97]. This could mean that the 202 plane is actually the 112 plane in the discharged diffraction pattern. The β-WO_3 structure corrolated to an orthohombic crystal structure

however the discharged diffraction pattern did not fit with standard tetrehedral lattice parameters and so can be concluded that a change in phase to α-WO_3 did not occur. Changes in calculated lattice parameters from pristine to charged did indicate a decreased volume in the unit cell structure. Given the very small capacity of Al^{3+} or $AlCl_4^-$ intercalation as seen in Figure 5-13, it can be determined that there was no reasonable intercalation of $AlCl_4^-$ into WO_3 in this study.

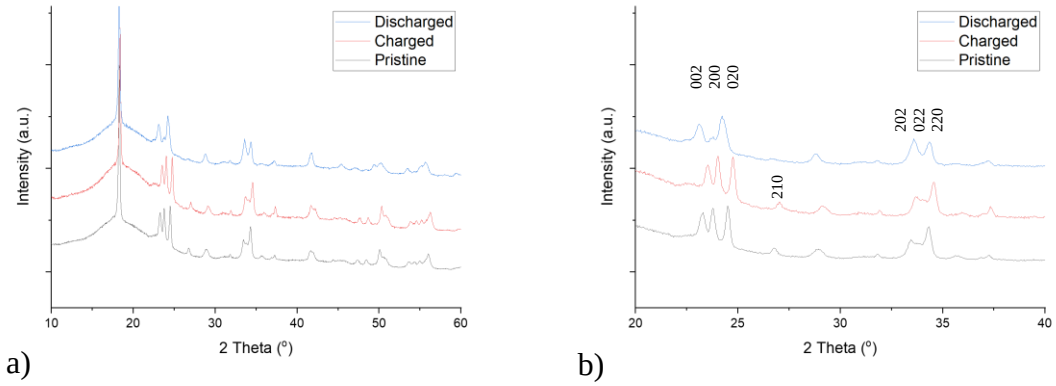

Figure 5-17 - XRD patterns of WO_3 at 0.7 V, 2 V, and pristine states at different x axis scaling a) 2θ 10-60° & b) 2θ 20-40°

5.3.2 Raman Spectroscopy

Raman spectroscopy was carried out on both graphite and reduced graphene oxide to study similarities as well as differences between intercalation ability. A key difference between this and the XRD studies is that the Raman spectroscopy was performed in an open-air environment, without specialist in-situ equipment which means air contamination of residual electrolyte is a factor to consider.

5.3.2.1 Graphite

Figure 5-18 shows the Raman spectra of graphite in its pristine state as well as both charged and discharged states. The obtained graphite spectra is in line with literature [98] with strong D, G, and 2D bands, with a smaller D+D" band around 2460 cm^{-1}. The G peak at 1583 cm^{-1} is the graphitic peak and comes from stretching and vibrating of the C-C bond, specifically the sp2 π bond in carbon systems. A secondary peak from the G band can result in a G', or more commonly named 2D, peak. This occurs at around 2720 cm^{-1}. The D peak around 1355 cm^{-1} is caused by sp2 hybridized forms of the carbon representing disorder due to structural defects as the bonds are out of plane, that is the hexagonal plane of graphene/graphite. The larger the D peak, the more

disordered the carbonaceous material is as the number of sp3 bonds grows. All spectra have been normalised with respect to the G band intensity.

From Figure 5-18, it can be seen that the graphite when charged to 2.2 V vs Al wire displays a significantly larger and broader D peak of higher intensity in comparison to pristine graphite. The broader the D peak, the more amorphous the structure is as many smaller peaks representing several defect states constitute the broader peak resulting from both contraction and expansion of the carbon bonds. Charging the graphite has negatively altered the structure, but not irreversibly as the discharged spectra is almost identical to the pristine spectra.

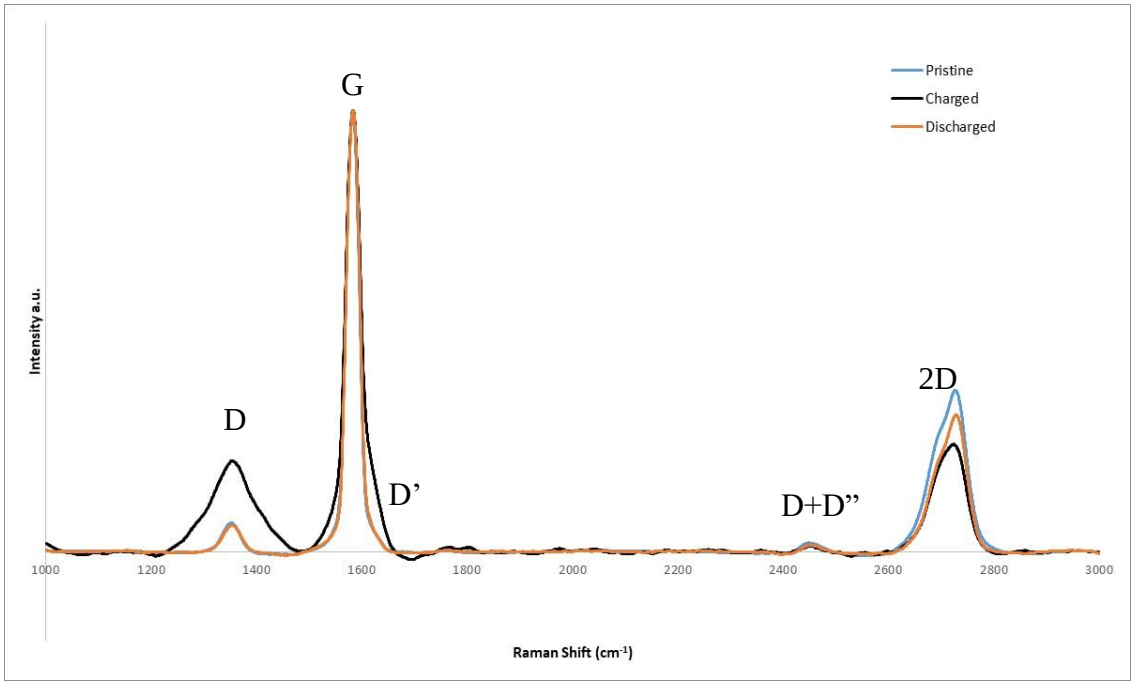

Figure 5-18 – Raman Spectra of Graphite in pristine, charged, and discharged state, 1000-3000 cm^{-1}

A positive shift of the G peak would indicate that intercalation has taken place, the higher the shift the lower the intercalation stage number, with a larger shift revealing larger amount of intercalation i.e. once the energy required to further fill the stage 'n' layer becomes higher than the energy it takes to overcome van der Waals forces in other layers, stage 'n-1' intercalation takes place, up until stage 1 where all layers are filled and ions are inserted between every graphitic layer [48]. The G peak however shows no significant positive shift. However, a positive shift (blueshift) in the D peak shows a slight reversible shift from 1351 cm^{-1} to 1356 cm^{-1} from pristine to charged and back down on discharge; this means the lattice structure is experiencing strain as it is being compressed. This positive shift is due to a changing ratio of disorder within the amorphous D peak. Fitting of the D peak reveals the constituent peaks; Figure 5-19 shows a basic deconvolution of the

D as well as G bands from the charged spectra to illustrate the formation of an amorphous peak from smaller peaks representing both bond strain and contraction. Charging of the graphite therefore increases the level of sp3 bond contraction, brought about by the addition of $AlCl_4$ through insertion.

The I_D/I_G ratio, which is a measure of the sp3/sp2 bonds and therefore a measure of structural defects, is less than 1 in Figure 5-18 for all spectra. The graphitic structure is dominant and shows a good level of order in the pristine graphite as well as the discharged graphite. When charged, the ratio increases substantially to display an increased level of disorder. The D' peak, which can be seen more clearly in Figure 5-19, a deconvoluting of the D and G bands between 1100-1800 cm^{-1}, presenting as a shoulder on the side of the G band at around 1620 cm^{-1}, also corresponds to a level of disorder or impurities within the sp2 bonds and is significantly larger in the charged spectra.

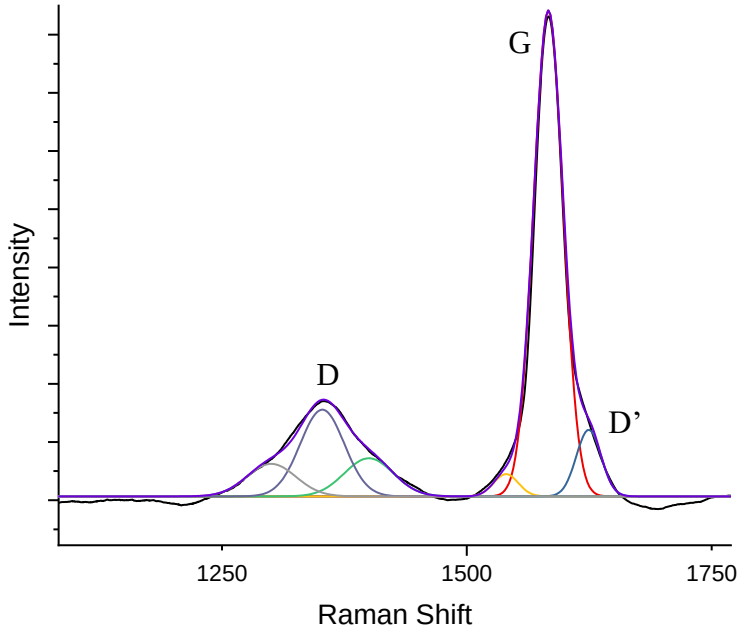

Figure 5-19 – Deconvolution of Raman Spectra of charged Graphite D and G bands at 1100-1800 cm^{-1}

The small D' peak shows similarities with literature regarding G band splitting due to intercalation. Stage 1 fully intercalated graphite displays as a peak at 1634 cm^{-1} after transitioning from pristine graphite at 1583 cm^{-1} with an intermediate peak around 1620 cm^{-1} as the staging mechanism begins [24, 99]. Work carried out by Dimiev et al. demonstrates that the intermediate peak at 1620 cm^{-1} is shown not to appear with great intensity when a 532 nm excitation laser is used as opposed to when a greater laser energy is used [24, 100]. The D' peak, caused by the same defect as lower stage intercalation, also provides a weaker peak at lower laser wavelengths [101] and is the reason for a

reduced intermediate intercalation D' peak in this study due to the use of a 532 nm laser. A laser of higher intensity would reveal more of the intercalation. Therefore, the increased intensity of the charged D' in Figure 5-18 compared to the pristine and discharged spectra points towards chloroaluminate intercalation, supporting previous conclusions from the voltammetry in Figure 5-10 which showed superimposed oxidations from both intercalation and chloroaluminate oxidation. The specific capacity of graphite, explored in greater depth in the following chapter, is 295 $mAhg^{-1}$ which is comparatively larger than the more disordered carbonaceous materials. This higher degree of structural order implies that graphite could more easily accept ions in between its layers when compared to more amorphous carbon structures with fewer ordered layers such as rGO or carbon black powder, as the increased level of defects and lower degree of crystallinity makes it more difficult to accept anionic intercalants [102]. Graphite is allowing almost fully reversible intercalation which provides the large specific capacity, however it is charged to a higher voltage of 2.4 V to elicit high capacities compared to the lower 2.2 V here, to study structural changes due to intercalation.

At around 2700 cm^{-1} the 2D peak, which can be used to distinguish between a single monolayer and multiple layer graphite, is seen in the pristine and discharged samples with a shoulder at a slightly lower shift. This smaller peak represents different interlayer interactions [103].

5.3.2.2 Reduced Graphene Oxide

Compared to the graphite in Figure 5-18, the reduced graphene oxide Raman spectra shown in Figure 5-20, shows a much lower structural quality. The D and G peaks are much broader than in Figure 5-18 and a new peak, a D* peak has emerged at around 1450 cm^{-1} which increases substantially when charging and decreases with a blueshift upon discharge. This new peak has been reported to be due to an additional out-of-plane directional defect linked to the structural bending within graphene monolayers [104].

The G peak shows minimal redshift of $3cm^{-1}$ while a greater decrease in wavenumber is observed in the D peak; a redshift from 1349 to 1341 cm^{-1} indicates tensile strain as the lattice undergoes expansion. A slight positive shift upon discharge relieves some of the tensile stress as the lattice contracts. However, with no shift in the G band and no formation of a secondary D' peak as with graphite, the change in lattice defects is not caused by intercalation within the rGO structure, instead just an increase in amorphousness. This agrees with the XRD results above which did not show any intercalation of $AlCl_4^-$.

For the pristine spectra, the G peak is slightly larger than the D peak making the I_D/I_G ratio just below 1. This ratio increases beyond 1 after charging and discharging have taken place, signifying that the degree of disorder has increased as charging has taken place, and the graphitic structure is weak and/or damaged making the charging quasi-reversible. Intercalation has not taken place, instead the rGO has acted as a capacitor accumulating a charge which is in line with what was seen previously in Figure 5-8 with such a large double layer effect and minimal redox.

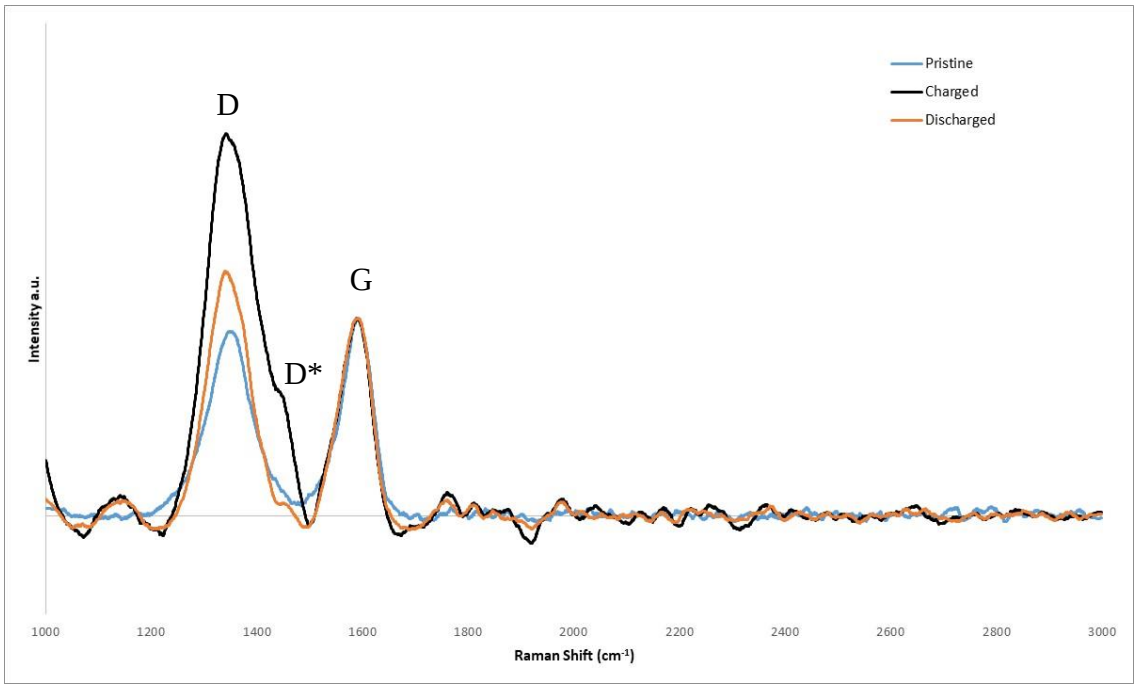

Figure 5-20 – Raman Spectra of reduced graphene oxide in pristine, charged, and discharged state, 1000-3000 cm^{-1}

The absence of a 2D peak or a weak, unobservable peak throughout the spectra is not anomalous and illustrates the disordered and multi-layered nature of the fabricated material which fits more in line with GO than rGO suggesting that the GO sample is not fully reduced [105].

5.3.3 STM

Use of an STM would allow the individual layers of graphite to be observed and their depth measured. Performing STM measurements during a charge discharge cycle will reveal the interlayer spacing required for the intercalated ion. Highly ordered pyrolytic graphite (HOPG) was used for this experiment to ensure adequate interlayer spaces for intercalation to take place and for the layers to be visible on the microscope. Instability of the STM tip in the corrosive electrolyte caused some signal noise but the change in structure due to intercalation is clear.

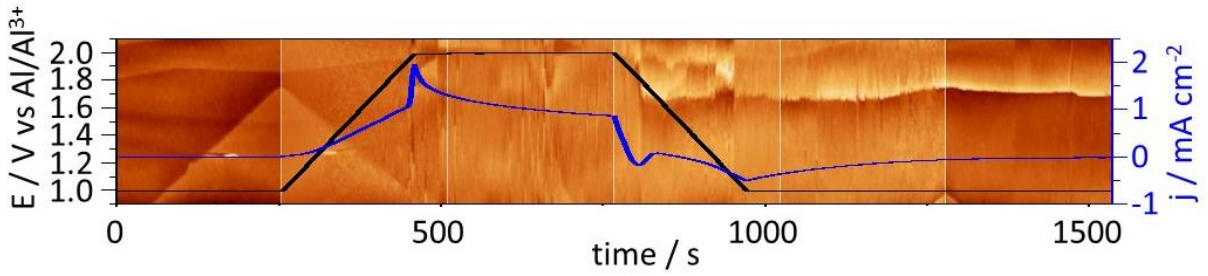

Figure 5-21 – STM images[81] in series w.r.t. time, of HOPG in Emic/$AlCl_3$ electrolyte. CV data gathered in-situ superimposed

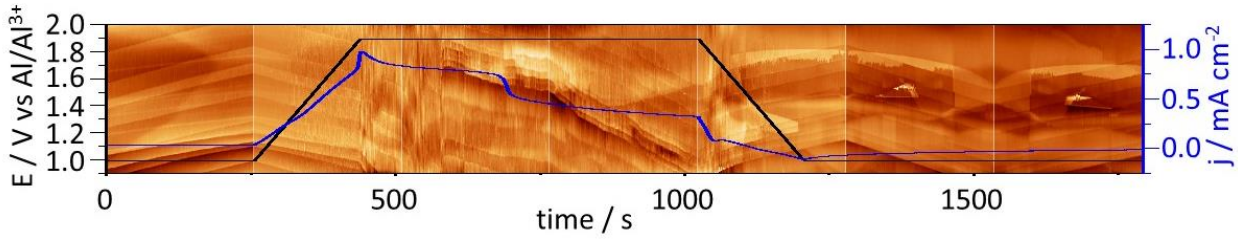

Figure 5-22 - STM images in series w.r.t. time, of HOPG in Bmic/$AlCl_3$ electrolyte. CV data gathered in-situ superimposed

Figure 5-21 shows a time-lapse of STM images during a charge discharge cycle using 1:1.3 Emic/$AlCl_3$ electrolyte, and Figure 5-22 shows the same using 1:1.3 Bmic/$AlCl_3$. The high corrosivity of Emim-Cl affected the STM tip and caused large signal noise making it difficult to discern graphite layers for intercalation analysis (e.g. see comparison between Figure 5-21 and Figure 5-22 at 500-750s). The Bmic/$AlCl_3$ cycle displayed a cleaner signal and held a higher current for a longer period of time before the voltage was decreased. Their similarity in structure should provide reasonably similar intercalation in an aluminium system.

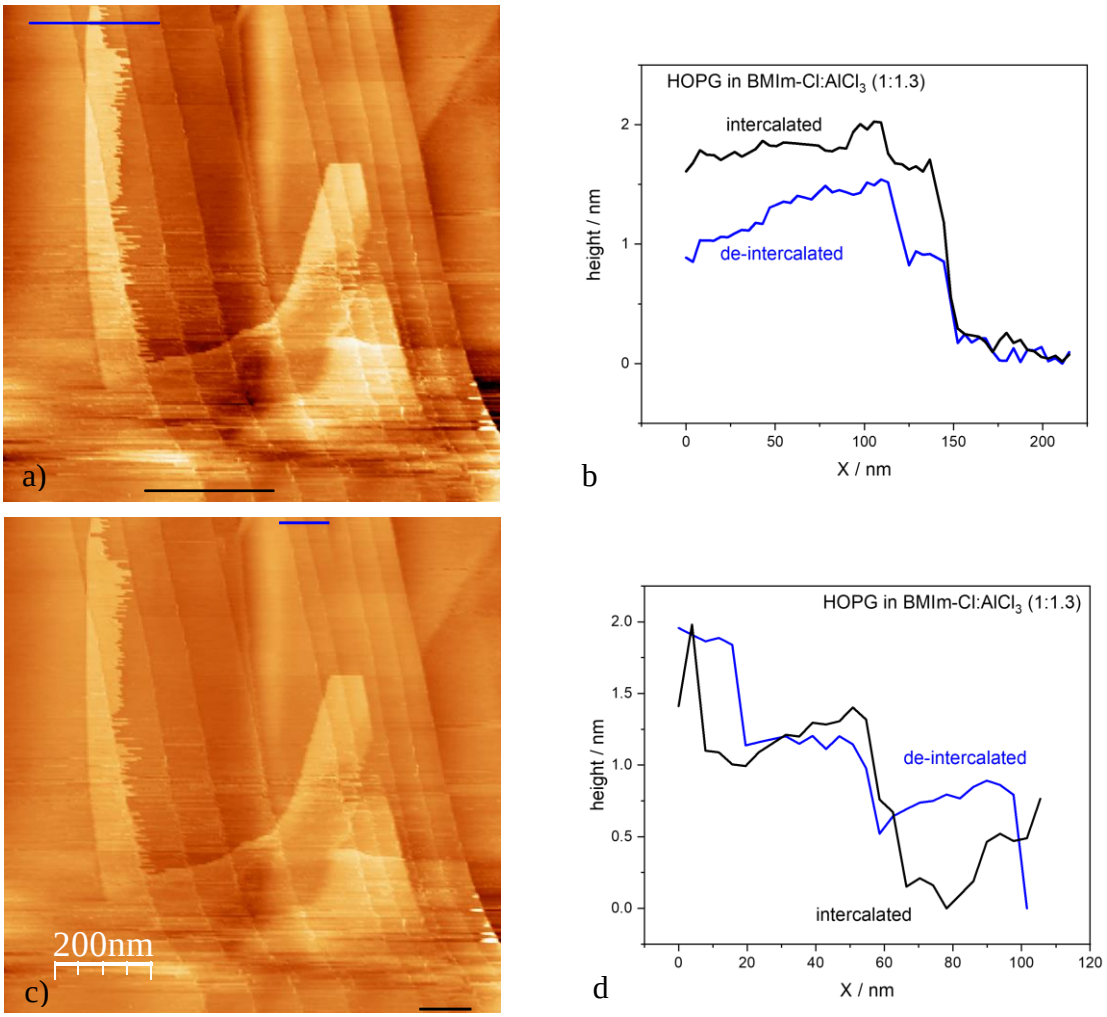

Figure 5-23 – HOPG in Bmim/$AlCl_3$ 1:1.3 electrolyte a) & c) STM image of de-intercalation from the bottom up showcasing multiple graphite layers. b) & d) Comparison of the heights in 'a' & 'c' between intercalated and de-intercalated layers.

As the graphite swells due to the intercalation of the chloroaluminate species, the distance between the surface and the tip decreases, leading to an increased voltage of the piezo crystals that control the height of the cell stage. The tip will crash into the surface and will likely be damaged if the distance decreases too much. As the surface warps during the period of intercalation, the tip can get encumbered by graphite flakes which affect the quality of the images being captured meaning that for parts of the intercalation, it is very difficult to see exactly what is happening. This kind of disturbance is visible in Figure 5-22 during the 3rd and 4th images where the potential is held at the upper limit of 1.9 V.

Figure 5-23b shows the height difference between de-intercalated and an intercalated state of graphite. Literature provides the size of an $AlCl_4$ molecule to be 5.28 Å [48] and a standard interlayer spacing of pristine graphite to be 3.35 Å [80], close to the obtained value of 3.29 Å from

XRD. This intercalation distance, taken from the same graphite layers is around 0.5-0.75 nm or 5-7 Å which is in keeping with the literature values for $AlCl_4$. This can also be seen in Figure 5-23d as the intercalated 'step' is much larger in size than the de-intercalated state, with the interlayer spacing increasing by about 5 Å. Thus, it can be concluded that the onset of intercalation has taken place, but due to attempts to limit the potential for a clear STM image, this has resulted in a larger intercalation staging and reduced intercalation similar to that observed in XRD where limited charging was carried out to prevent electrolyte degradation. Higher charging would therefore be needed to reach a fully intercalated stage 1 GIC.

5.4 Conclusion

Voltammetry was run on carbon black, rGO, graphite, and MnO_2 using 1:1 Emim/$AlCl_3$ electrolyte. The CVs of both carbon black and reduced graphite oxide showed quasi-reversible adsorption as well as chloroaluminate redox occurring at 1 V vs Ag/AgCl. The efficiencies were 54% and 60% respectively. The low values are influenced by the large chloroaluminate oxidation which overlaps the adsorption and has a low reversibility. Graphite, which is highly ordered by nature, did not show evidence of adsorption or intercalation of $AlCl_4$ in the 1:1 electrolyte within the same potential window as chloroaluminate reactions was dominant. Manganese (IV) oxide similarly showed no evidence of intercalation of $AlCl_4^-$ in the 1:1 electrolyte.

When using 1:1.3 electrolyte, which allowed for a larger potential window by increasing the onset potential required for chloroaluminate oxidation to 2 V vs Ag/AgCl, graphite exhibited clear intercalation of $AlCl_4$ with a coulombic efficiency of 96%. Carbon black displayed large double layer effects and adsorption of $AlCl_4$ before oxidation of chloroaluminate ions took place. In the case of rGO the adsorption of $AlCl_4$ couldn't be strongly confirmed. Limiting the oxidation potential for both to 1.9 V vs Ag/AgCl decreases the extent of side reactions which increases the coulombic efficiency. MnO_2 and WO_3 displayed very low current densities, and limited intercalation ability in WO_3 and no intercalation in MnO_2 sample. WO_3 did show multiple redox reactions as its oxidation state changed but beyond the oxidation potential of 1.9 V, $AlCl_4^-$ oxidation occurred.

Raman spectroscopy revealed changes in the D' peak for graphite upon charge suggesting that intercalation has taken place. It is believed that this peak results from splitting of the G peak, indicative of intercalant staging within the graphitic layers. However, absence of a greater shift in

the G peak could suggest that a higher wavelength laser is required to capture the full extent of intercalant staging. A more intense and broader D peak upon charge results from both contraction and expansion of the carbon bonds, which would benefit from further study to determine whether intercalation or deposition of $AlCl_4^-$ is the cause of this increased disorder. Raman spectra of charged rGO only showed an increase in disorder resulting in an I_D/I_G ratio above 1 with no evidence of intercalation.

XRD of graphite revealed the onset of intercalation when charged to 2.1 V vs Ag/AgCl with an intercalant staging of 9 and calculated intercalant gallery height of 4.66 Å. While this is less than the size of an $AlCl_4^-$ ion at 5.28 Å, it is believed that contraction of other layers allows for increased expansion of the intercalant layer to allow the insertion of $AlCl_4^-$. Charging further would increase the intercalation but increases the risk of electrolyte degradation as chloroaluminate ions are oxidised. Reduced graphene oxide didn't show signs of intercalation from XRD measurements, but instead partially irreversible phase changes. WO_3 showed small changes and contraction of volume on charging, however since the amount of change is small and the amount of intercalated charge is small too, results were inconclusive. However, literature suggests that it is Al^{3+} (and not $AlCl_4^-$) that is intercalated in WO_3 in aqueous solutions. The highly ordered nature of graphite is the most suitable for intercalation of larger ions, however even graphite showed irreversibility as the structure did not return to its original form upon discharge due to the stresses and strains imposed.

The corrosivity of Emic/$AlCl_3$ electrolyte hindered STM causing distorted results. Bmic/$AlCl_3$ prepared in the same ratio, acting as a substitute for the purpose of intercalation, showed intercalation of the $AlCl_4^-$ ion into a few graphite layers through increased height proportional to the size of $AlCl_4^-$. Large amounts of disorder of the graphitic layers upon intercalation and de-intercalation are also observed, confirming what was seen from the D bands of the Raman spectra. The expansion of only select layers indicates a lower stage of intercalation and that higher charging would be needed to reach stage 1.

Chapter 6. Investigation of Full Cell using different electrode materials

6.1 Introduction

An investigation into the use of different positive electrodes within an electrochemical cell will allow for a direct comparison of how various electrode materials affect battery performance. Running voltammetric and charge/discharge tests will provide results on key performance indicators such as specific capacity, specific energy, and estimated life of battery. This is particularly important as it has shown previously, concentration of $AlCl_4^-$ and $Al_2Cl_7^-$ in the electrolyte affects Al-ion battery capacity, anode and cathode equilibrium potentials (Eq. 4-13 and Eq. 4-14), and the oxidative stability window of the electrolyte. Therefore, tests using standard battery separators with small electrolyte volume setup (as opposed to large volume glass cells tested in Chapter 4 and Chapter 5) will result in large changes of concentrations of $AlCl_4^-$ and $Al_2Cl_7^-$ concentrations on charge/discharge, giving a holistic view of the cell in conditions that more closely resemble the real world in terms of size, capacity, stability and resistances encountered, as well as interactions between the anode, electrolyte, and cathode. The electrode materials tested were not composited and are unassisted by added conductive elements e.g. carbon to metal oxides. In-situ reference electrode coupled with impedance spectroscopy was used to be able to separate anode, cathode, and IR losses in the cell. As shown in chapter 4.2.3 the Al wire acts as reference electrode with the redox couple being Al, $AlCl_4^-/Al_2Cl_7^-$ with potential value equal to -0.2 V vs Ag/AgCl in 1:1.3 electrolyte. The reference potential is sensitive to $AlCl_4^-$ and $Al_2Cl_7^-$ concentration changes in the electrolyte (Eq. 4-13) and therefore such effects will be inherently captured by the measurements. Circuit fitting of impedance spectra was also attempted to obtain an estimate of diffusion coefficients of active ions.

6.2 Electrode Materials

6.2.1 Carbon-Based Batteries

6.2.1.1 Battery using Carbon Black Cathode

Figure 6-1 shows polarisation data of carbon black positive electrode in a battery setup using a 0.65 mm thick glass fibre separator and an aluminium disc negative electrode.

Voltammetry of carbon black, as seen in the previous chapter, resembles ideal capacitor behaviour (rectangular shape response). In comparison to half measurements in the previous chapter, IR effect on the voltammogram, typically seen by the slope of the current in the voltammogram, is minimal

in this cell setup due to the small distance between the anode and cathode, and importantly between the cathode and Al reference electrode which was embedded in the separator. The voltammetry at various scan rates shows that the carbon black cell is following capacitive behaviour with double layer current proportional to the scan rate. There is a small oxidation shoulder beyond 1.5 V and the small corresponding reduction peak at 1.9-1.7 V indicates a small amount of adsorption of $AlCl_4^-$ is taking place at high potentials, supporting the conclusion from the previous chapter. The shoulder seen could also be caused by $AlCl_4^-$ oxidation and soluble Cl_2 reduction but as discussed below it is unlikely. While it was shown that the oxidation onset in 1:1.3 electrolyte was 2 V vs Ag/AgCl or 2.2 V vs Al reference electrode, as discussed above due to a net increase of $AlCl_4^-$ concentration in the electrolyte on battery charging, the onset potential of $AlCl_4^-$ will decrease below 2.2 V vs Al wire as reported in chapter 4.2.3. However, given the small current observed it is highly unlikely this will cause negative shift of 0.5 V equating to over 10 orders of magnitude increase in $AlCl_4^-$. The coulombic efficiency obtained was just over 100% confirming no side reaction. This can be explained by the relatively low current capacity obtained contributing to +/- 3% error in coulombic efficiency calculation and is in line with the predominantly capacitive current observed (double layer) which is reversible.

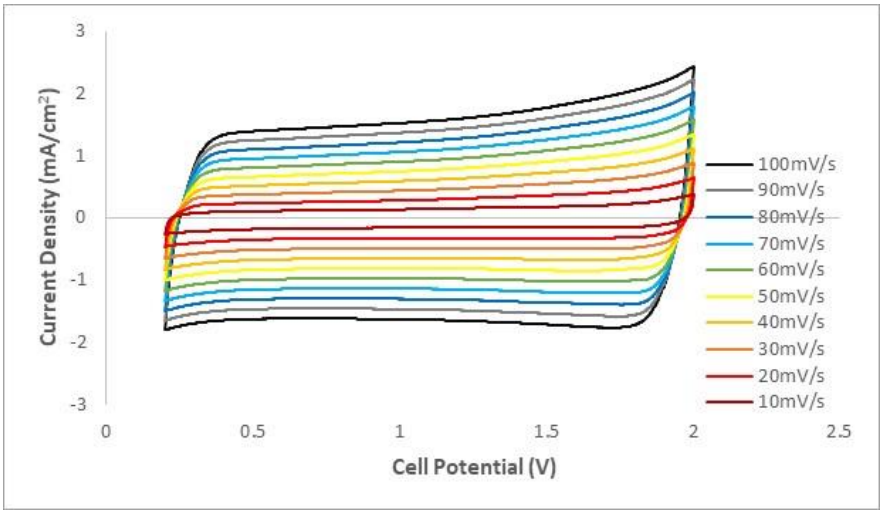

Figure 6-1 – CVs of Carbon black / Al battery, scanned between 0.2 - 2 V at different scan rates

Error! Reference source not found. shows the electrical impedance spectra of carbon black WE/ Al CE battery in Emic/$AlCl_3$ 1:1.3 electrolyte at 1 V and 2 V. The spectra were fitted using a Randles circuit with the addition of inductance to account for high frequency inductance behaviour of the test wires and finite space diffusion, T element to account for intercalation or electro-adsorption of $AlCl_4^-$ in finite length e.g. graphite particles, as seen in Figure 6-2. The initial resistor

for electrolyte solution resistance is followed by an inductance 'L' element. A constant phase element 'Q' has taken the place of the capacitor for the non-uniform electrode surface and following the charge transfer resistance is diffusion T element.

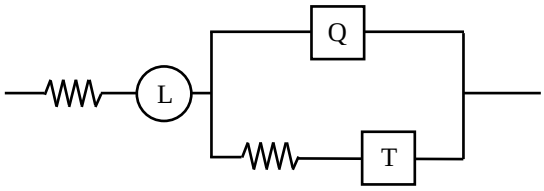

Figure 6-2 - Modified Randles Circuit featuring an inductance element and a constant phase element, used to fit battery impedance data

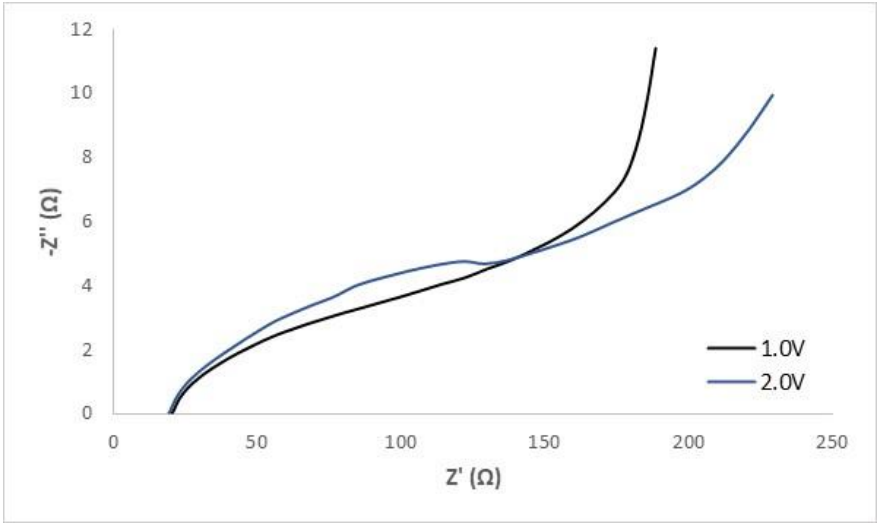

Figure 6-3 – EIS spectra of Carbon black / Aluminium battery, Emic/$AlCl_3$ 1:1.3 electrolyte, at 1 V and 2 V

Table 6-1 - Circuit fitting values from carbon black battery impedance data

Carbon Black		
	1.0 V	***2.0 V***
R_{Sol} (Ωcm^2)	13.97	13.35
R_{CT} (Ωcm^2)	61.3	88.3
D ($cm^2 s^{-1}$)	1.55×10^{-12}	1.12×10^{-12}
$\boldsymbol{\delta}$ (cm)	2.21×10^{-6}	2.22×10^{-6}

From fitting the modified Randles circuit, resistance, and diffusion values in Table 6-1 have been obtained and calculated for carbon black electrode.

The value of R_{CT} at 1 V suggests that some faradaic reaction is taking place on the carbon black surface (e.g. electro-adsorption) even at 1 V and that the current seen is not just non-faradaic double layer charging current. The increase in charge transfer resistance from the electrode potential increase from 1-2 V suggests that the surface is becoming increasingly saturated with adsorbed species making any further electro-adsorption more difficult. The very low value of diffusion coefficient suggests that the limiting diffusion process is not that of $AlCl_4^-$ diffusion in solution but in solid ie. the carbon surface interface. The equivalent diffusion length is also very low at around 22 nm and doesn't change with cell voltage suggesting the process is surface limited.

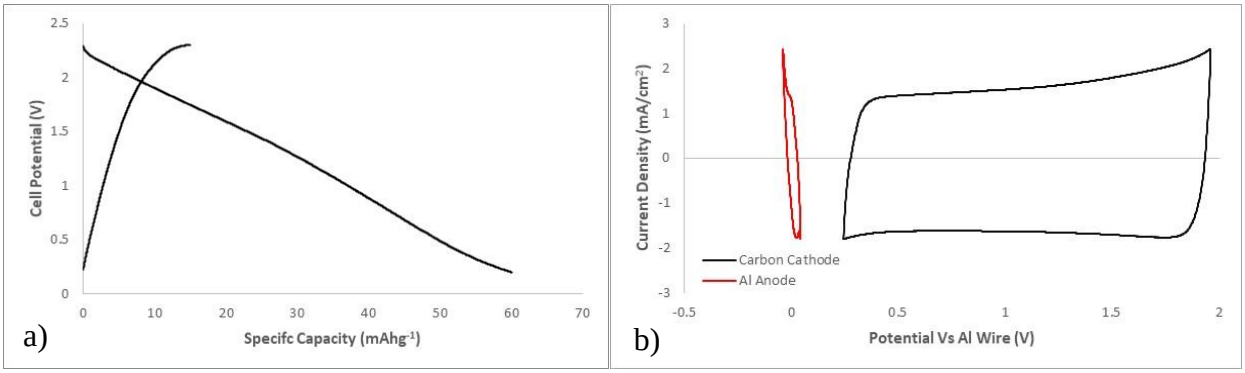

Figure 6-4 – Carbon black/ Al battery Emic/$AlCl_3$ 1:1.3 charged between 0.2-2.3 V a) Charge/ discharge profile, discharge C rate 1.2 b) cathode and anode polarisation data vs Al wire at 100 mVs^{-1}

Figure 6-4 shows the charge/ discharge profile and separate anode/ cathode scans for a carbon black WE/ Al CE battery. The carbon black cell achieved specific capacities of 56.1 $mAhg^{-1}$ with a capacity degradation rate of 0.17 $mAhg^{-1}$ per cycle. The capacity is caused by electro-adsorption and double layer surface processes as mentioned above which explains the low capacity decay rate. Capacities for activated carbon have been reported at 117 $mAhg^{-1}$ with coulombic efficiencies of 74% [54]. Efficiencies observed here for carbon black in Figure 6-4a show the charge to discharge ratio high above 100%. The charge/ discharge cycles were heavily distorted with a rapid charge and slow discharge, overwhelmed by additional side reactions as the cell experienced high voltages of 2.3 V. The anode potential scan in Figure 6-4b demonstrates how the anode potential remains close to 0 V vs Al wire, becoming more negative as the electrolyte composition changes i.e. a decrease in $AlCl_4^-$, as the cathode approaches higher potentials adsorbing more $AlCl_4^-$ and eventually oxidising it at greater potentials.

6.2.1.2 *Battery using Graphite Cathode*

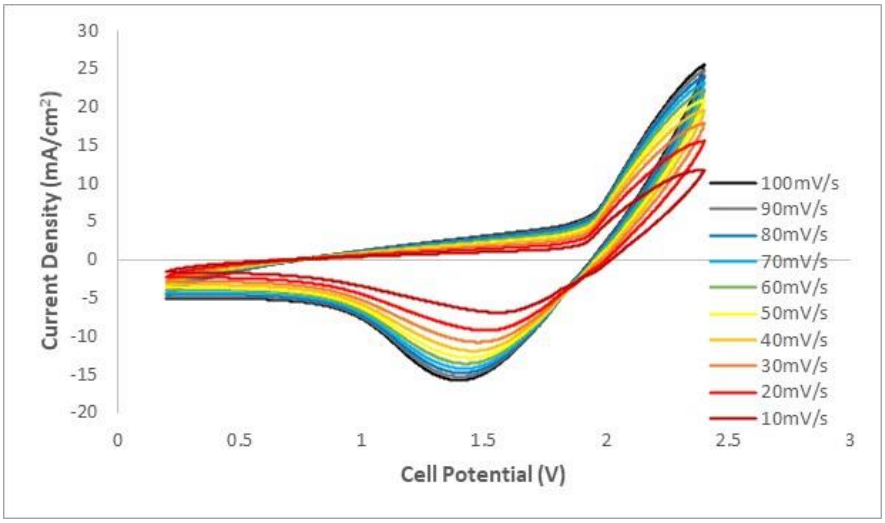

Figure 6-5 – CVs of Graphite / Aluminium battery, scanned between 0.2 - 2.4 V at different scan rates

Figure 6-5 shows polarisation data of graphite positive electrode vs Al disc negative electrode in a battery setup using a 0.65 mm thick glass fibre separator.

The response seen of graphite cathode is in agreement with previous results on half-cell tests. The intercalation current displayed a limiting current behaviour, as a peak began to form towards end of the anodic limit of the scan. The values of the peak current varied linearly with the square root of the scan rate suggesting that the intercalation is diffusion controlled which is reasonable considering the larger size of intercalated ion ($AlCl_4^-$). The voltammogram has not significantly changed when compared to the half-cell data in the previous chapter; onset potential of $AlCl_4^-$ intercalation in graphite was reported to be 1.6 V vs Ag/AgCl in the previous chapter which agrees well with the 1.9 V value vs Al, $AlCl_4^-/Al_2Cl_7^-$ reported here. The coulombic efficiency obtained here was 95% in line with previous chapter results of 96% and literature values of 90-98% [52, 54]. This supports that the lower than 100% value is caused by some irreversibility in the intercalation process as seen in characterisation results in the previous chapter, and not $AlCl_4^-$ oxidation.

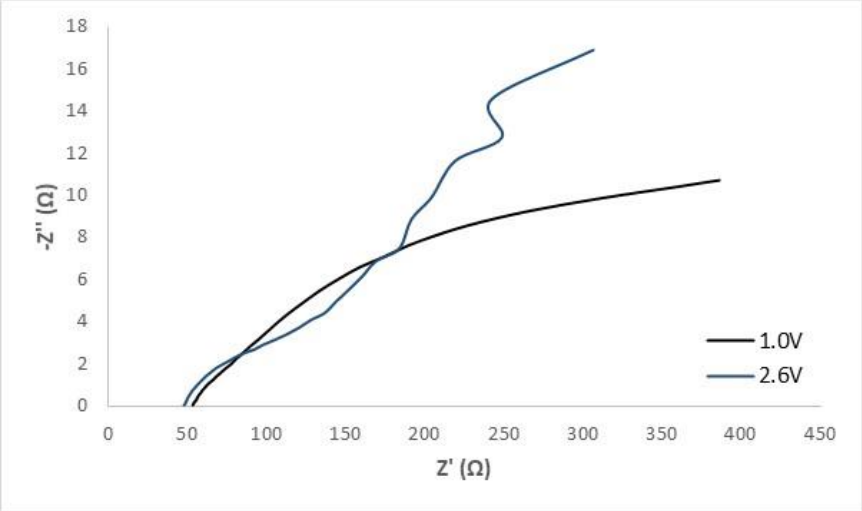

Figure 6-6 – EIS spectra of Graphite / Aluminium battery, Emic/$AlCl_3$ 1:1.3 electrolyte, at 1 V and 2.6 V

Figure 6-6 shows the impedance spectra of the graphite/ aluminium battery at 1 V and 2.6 V. From fitting the modified Randles circuit, resistance, and diffusion values in Table 6-2 have been obtained and calculated for the graphite battery. The value of R_{CT} at 1 V > 350 Ωcm^2 suggests that no significant faradaic reaction is taking place on graphite surface. The value decreases significantly at 2.6 V by over two orders of magnitude and is lower than that seen on carbon black despite the significant higher specific surface area of carbon black to graphite at 1000 m^2g^{-1} to <100 m^2g^{-1} respectively. The value of diffusion coefficient of 5 $x10^{-11}$ cm^2s^{-1} is order of magnitude higher than that obtained for the carbon black interface but is still very low suggesting that the limiting diffusion process is not that of $AlCl_4^-$ diffusion in solution but in solid i.e. inside the graphite materials. The equivalent diffusion length of 376 nm, an order of magnitude larger than that in carbon black suggests that the process is not constrained to graphite surface but also through bulk i.e. intercalation.

Table 6-2 - Circuit fitting values from graphite impedance data

Graphite		
	1.0 V	***2.6 V***
R_{Sol} (Ωcm^2))	36.4	33.6
R_{CT} (Ωcm^2)	368.3	35.9
D (cm^2s^{-1})	6.56 $x10^{-12}$	5.14 $x10^{-11}$
$\boldsymbol{\delta}$ (cm)	1.05 $x10^{-5}$	3.76 $x10^{-5}$

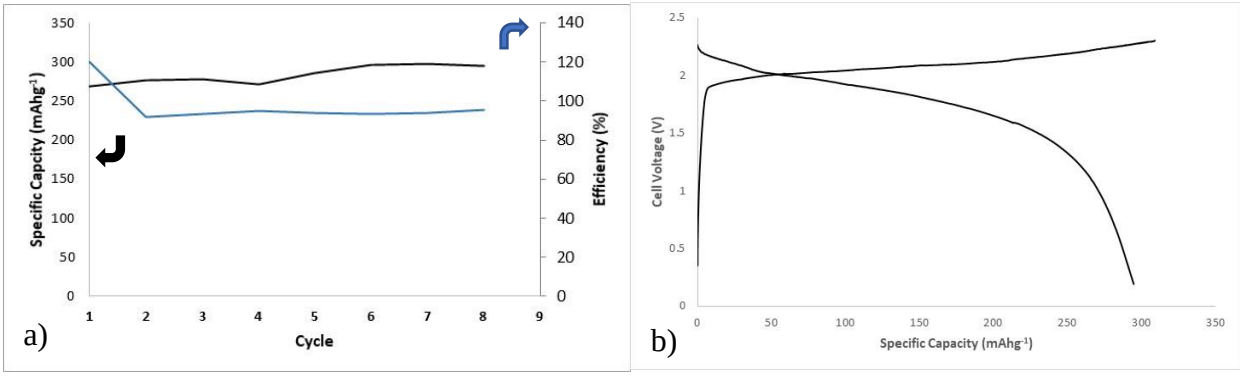

Figure 6-7 – Graphite / Aluminium battery Emic/$AlCl_3$ 1:1.3 charged between 0.2 - 2.4 V a) Discharge specific capacity and coulombic efficiency cycling data b) Charge/ discharge profile, discharge at C rate 0.7

Figure 6-7a show the capacity and efficiency cycling data for the graphite/ aluminium battery charged from 0.2-2.4 V. The graphite battery revealed the largest specific capacity of the carbon-based positive electrode batteries, at 294.8 $mAhg^{-1}$ at 200 mAg^{-1} with an efficiency at 95%. A specific energy of 500 $Whkg^{-1}$ was also achieved. Specific capacities of various graphite materials from literature range from 59-110 $mAhg^{-1}$ [52-54, 106], with composite materials achieving much higher. The theoretical specific capacity for graphite intercalation compounds (GIC) involving $AlCl_4^-$ ions is calculated to be 69.8 $mAhg^{-1}$ based on the literature value of 32 mols of carbon required to intercalate 1 mol of $AlCl_4^-$ [47]. Given the achieved specific capacity of 294.8 $mAhg^{-1}$ is 4.2 times larger than the theoretical capacity of 69.8 $mAhg^{-1}$, this signifies that the GIC is composed of 7.6 mols of carbon per $AlCl_4^-$, 4.2 times less than the reported 32. Large capacity values compared to literature values for graphene of over 150 $mAhg^{-1}$ in which exfoliation took place via $AlCl_4^-$ intercalation, putting stress on the graphitic layers [107]. The exfoliated nature of the graphite has caused increased flexibility of the graphitic layers allowing it to experience the intercalation of $AlCl_4^-$ relatively easily and with reduced capacity fade. The increased capacity could also be due to an increased volume of electrolyte within the cell which corresponds to an increased capacity due to the higher concentration and availability of $AlCl_4^-$ ions as discussed in chapter 4.2.3.

Repeated intercalation/ de-intercalation of chloroaluminate ions into the graphite layers results in an increasing capacity initially over 8 cycles. This can be explained by either irreversible expansion of graphite layer on intercalation or increase of surface area of the materials from cracking caused by the tensile strain (see section 5.3). The capacity will likely decrease over longer-term cycling after this extended activation period.

In Figure 6-7b showing the charge/ discharge profile of the graphite battery, the cell voltage decreased slowly on discharge and then suddenly drops at around 1.8 V as the battery ran out of charge. The reverse is seen when charging with the slope change happening around 1.95 V. In contrast, both rGO and carbon black show a gradual drop in cell voltage on discharge and an increase on charge over the entire studied voltage window in Figure 6-11b and Figure 6-4a respectively.

6.2.1.3 Battery using rGO Cathode

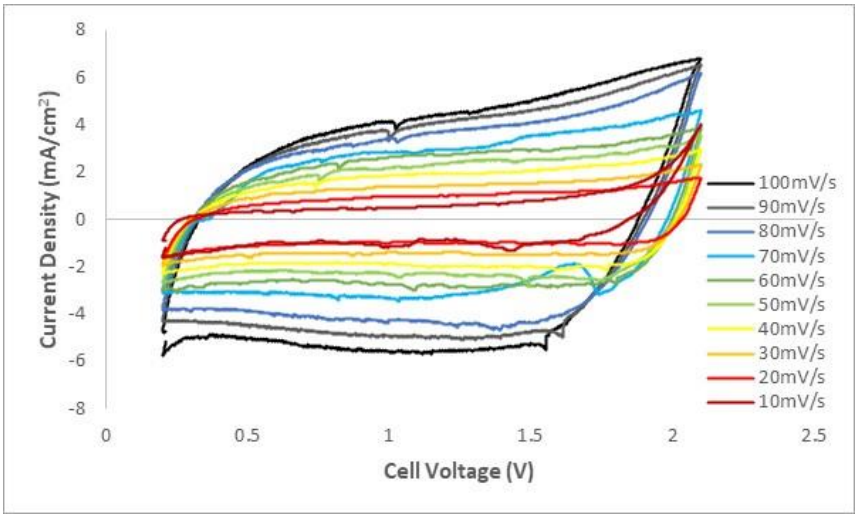

Figure 6-8 – CVs of rGO/ Aluminium battery, scanned between 0.2 - 2.1 V at different scan rates

Figure 6-8 shows the polarisation data of rGO positive electrode vs aluminium disc negative electrode in a battery setup using a 0.65 mm thick separator. Reduced graphene oxide behaves slightly differently to graphite and carbon black. It was shown in the previous chapter that there might be evidence of $AlCl_4^-$ adsorption but the extent or charge was so low it couldn't be confirmed with high confidence. The coulombic efficiency obtained was 89% which suggests that the adsorption process is not fully reversible or that some side reactions might occur (rGO oxidation for example).

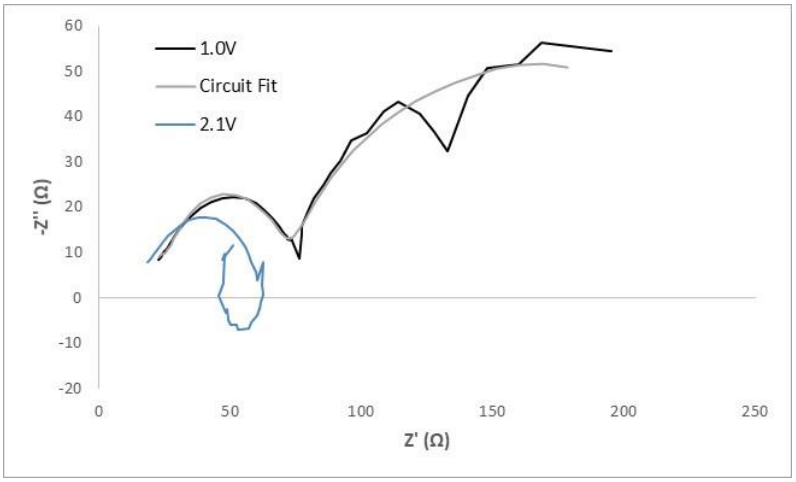

Figure 6-9 – EIS spectra of rGO / Aluminium battery, Emic/$AlCl_3$ 1:1.3 electrolyte, at 1 V and 2.1 V, with added circuit fitting

Figure 6-9 shows impedance spectra of rGO at 1 and 2.1 V vs Al, $AlCl_4^-/Al_2Cl_7^-$ in 1:1.3 electrolyte. An inductance behaviour at low frequencies can be seen that is usually assigned to slow (electro)adsorption processes at the electrode surface. This is seen as a negative loop on the spectra in the 2.1 V data. At 1 V, the spectra appears to consist of multiple time constants. While first time constant is represented by double layer/charge transfer time constant, the second could be caused by finite length diffusion e.g. solution diffusion in highly porous materials which can be represented by an 'O' element. This is most likely due to the high surface area and porosity of the rGO. The circuit fitted to rGO at 1V is shown in Figure 6-10.

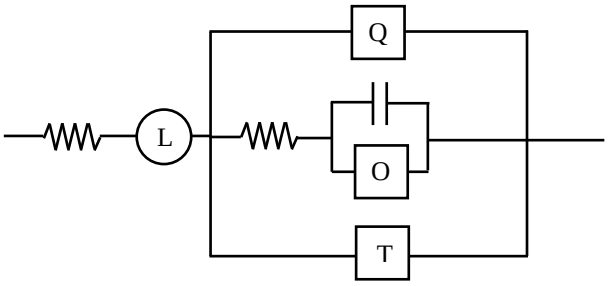

Figure 6-10 – Modified Randles circuit for multiple time constants featuring an 'O' diffusion element

The relatively low value of charge transfer resistance both at 1 and 2.1 V suggests that the process involves electron transfer (Faradaic current) even at low voltages. This is similar to what was seen in the case of carbon black i.e. electro-adsorption of $AlCl_4^-$ on rGO surface in addition to double layer charging (non-Faradaic). The diffusion coefficient obtained from the T element was significantly low in order of 10^{-15} cm^2s^{-1}. This value is very low even for diffusion in solids and could suggest significant diffusion barrier at interface. This is also consistent with the very low value of diffusion length obtained of 5.6 Å, around the size of an $AlCl_4^-$ ion, suggesting adsorption

is taking place at the very top surface/interface of rGO. The diffusion coefficient and length could not be fitted reliably at 2.1 V since no mass transport signature (slope between 45º and 90º) could be seen at low frequencies and instead the process seems to be limited by slow adsorption (low frequency inductance behaviour).

Table 6-3 - Circuit fitting values from rGO impedance data

rGO		
	1.0 V	***2.1 V***
R_{Sol} (Ωcm^2)	5.89	10.1
R_{CT} (Ωcm^2)	77.42	34.6
D ($cm^2 s^{-1}$)	1.99×10^{-15}	-
$\boldsymbol{\delta}$ (cm)	5.63×10^{-10}	-

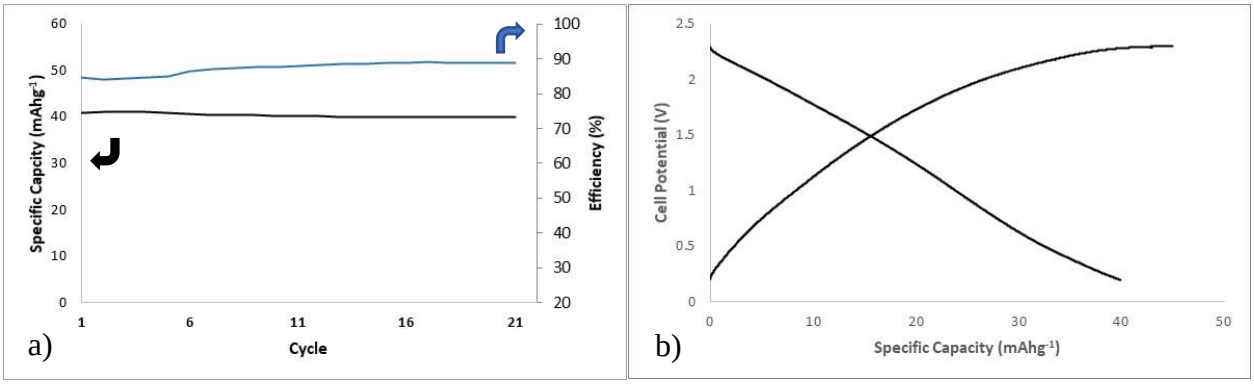

Figure 6-11 – rGO / Aluminium battery, Emic/$AlCl_3$ 1:1.3 charged between 0.2 - 2.3 V a) Discharge specific capacity and coulombic efficiency cycling data b) Charge/ discharge profile, discharge at C rate 1.8

Figure 6-11 shows cycling data and charge/ discharge profiles for the rGO WE/ Al CE battery charged between 0.2-2.3 V. rGO displays a specific capacity of 35.6 $mAhg^{-1}$ however this is due to the adsorption and capacitive double layer processes as discussed above. The coulombic efficiency of rGO stood at 89%, above literature values of 81%, however this was alongside a specific capacity of 148 $mAhg^{-1}$ [108], far higher than observed in this test.

Similar to carbon black, the increase of adsorbates capacity of rGO from repetitive adsorption/desorption could be caused by surface cleaning of other adsorbed impurities. Repeated cycling however results in capacity loss, as seen above. Both the intercalation and adsorption reactions are not fully reversible, resulting in large changes to the structure and at very high voltages, degradation side reactions take place. Without intercalation, the degradation rate of rGO

is substantially smaller than graphite at 0.05 $mAhg^{-1}$ per cycle and similar to carbon black, as ions stay closer to the electrode surface leaving the material structure relatively intact.

6.2.2 Hybrid Al-Li Battery

For this hybrid battery, the electrochemical redox reactions are reversible aluminium deposition/stripping at the anode and lithium intercalation/de-intercalation at the cathode

In principle, lithium salt is not needed in this new hybrid battery, since the lithium ion extracted from the $LiNi_{0.8}Mn_{.01}Co_{0.1}O_2$ cathode during the charge process will sustain the necessary electrochemical reaction in the following cycles as shown below. A similar process was confirmed on an Al|$LiFePO_4$ coin cell using the pure acidic ionic liquid Emic:$AlCl_3$ (1:1.1) [64].

At Anode: *Eq. 6-1*

$$Al + 3LiAlCl_4 + 4Emim\ AlCl_4 \leftrightarrow 4Emim\ Al_2Cl_7 + 3Li^+ + 3e^-$$

At Cathode: *Eq. 6-2*

$$3Ni_{0.8}Mn_{0.1}Co_{0.1}O_2 + 3Li^+ + 3e^- \leftrightarrow 3LiNi_{0.8}Mn_{0.1}Co_{0.1}O_2$$

Figure 6-12 shows polarisation data of the NMC positive electrode vs an aluminium disc negative electrode in a battery setup using a 0.65 mm thick separator, and specific capacity and coulombic efficiency cycling data. A sharp reduction current on NMC can be seen around 0.3 V vs Al, $AlCl_4^-$ /$Al_2Cl_7^-$ at slow scans e.g. 10 mVs^{-1}. The reaction is quite reversible and on reversal of sweep sharp anodic current could be seen ending with a peak and then decaying back to capacitive current. Increasing the scan rate results in a decrease in reduction current seen below 0.2 V and an increase in the double layer capacitive current, and consequently a decrease in the anodic oxidation current in the subsequent scan. The reduction stability of NMC and the electrolyte in the potential range around 0.2 V vs Al, $AlCl_4^-$/$Al_2Cl_7^-$ suggests that the most likely reaction is Al plating. The reason the Al plating is seen above 0 V vs Al, $AlCl_4^-$/$Al_2Cl_7^-$ is the concentration gradient of Li^+ and Al_2Cl_7 and $AlCl_4$ between the anode and cathode particularly with thicker separator with higher concentration of Li^+ and Al_2Cl_7 and lower concentration of $AlCl_4$ at cathode side of the cell in comparison to anode side as per reactions *Eq. 6-1* and *Eq. 6-2*. This will result in a shift of Al plating potential towards more positive values at the cathode in comparison to the anode. The fast

reversibility of the reaction (Al stripping on reverse) is consistent with Al stripping and plating. The decrease in current with an increase in scan rate is also consistent as a lower concentration gradient of the ions discussed above will occur with increased scan rate, thus reducing the positive shift of Al plating potential at the cathode and subsequently the plating current for the same lower scan limit. The oxidation current seen at voltages above 1.6 to 2.4 V vs Al, $AlCl_4^-/Al_2Cl_7^-$ is also consistent with Li intercalation in the NMC with a de-intercalation reduction peak seen between 1.6-0.6 V. Specific discharge capacity of NMC has been reported at 200 $mAhg^{-1}$ with a coulombic efficiency of 83% [109], whereas a specific capacity of 57.7 $mAhg^{-1}$ is achieved in this study with a lower efficiency of 59% degrading at a rate of 1.1 $mAhg^{-1}$ per cycle. The lower coulombic efficiency could be caused from the beginning of $AlCl_4^-$ oxidation reaction occurring towards the positive potential limit of the scan >2.2 V. The lower than expected capacity seen can easily be explained by lower Li^+ concentration in the electrolyte. The capacity reported for NMC is usually higher in electrolytes containing at least 1M Li^+ salt. In the tested hybrid battery, since no Lithium salt was added, the Li^+ in solution is obtained from de-intercalation of NMC. Given the small amount of NMC used in the electrode and the relatively large volume of electrolyte this will result in a very low Li^+ concentration in the electrolyte. This means that the majority of the lithium in the NMC will be extracted which is known to result in rapid capacity decay of the NMC due to collapse of the NMC structure. On re-intercalation it is not possible to re-insert all the lithium from solution as the concentration is low and will continue to go lower as intercalation proceeds unlike in a traditional Li-ion battery where it remains constant around 1M.

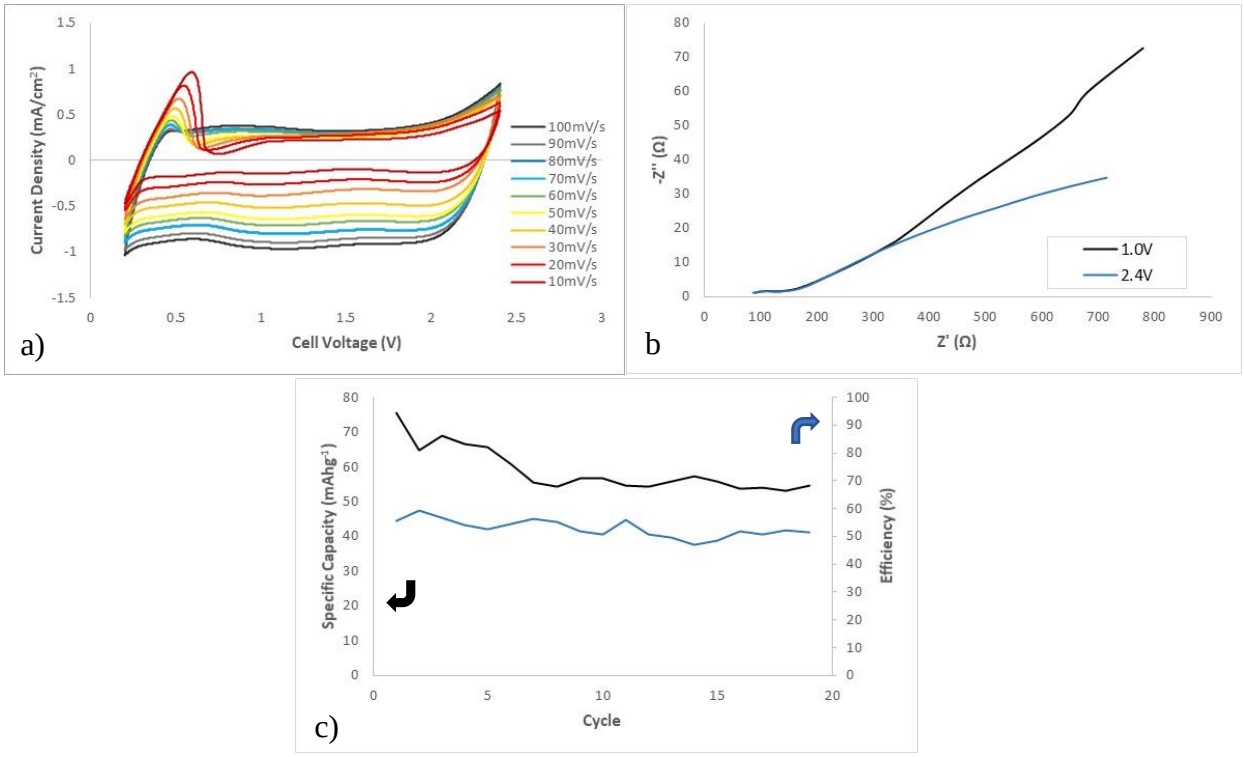

Figure 6-12 – a) CVs at different scan rates, b) impedance spectra and c) discharge specific capacity and efficiency cycling data of NMC / Al Emic/$AlCl_3$ 1:1.3 battery cycled between 0.2-2.4 V

Figure 6-12b Shows impedance spectra at 1V and 2.4V of the NMC battery. EIS data in Table 6-4 shows an increase is diffusivity and diffusion length from fitting impedance data at 1 and 2.4 V vs Al, $AlCl_4^-/Al_2Cl_7^-$. At 1 V no significant diffusion/intercalation is taking place with very low diffusion coefficient and diffusion length. At 2.4 V the diffusion coefficient obtained is relatively fast in the order of 10^{-8} cm^2s^{-1} which is consistent with rapid diffusion of small Li^+ ions in NMC. The diffusion length obtained around 4µm is also consistent with average particle radius of NMC particles used.

Table 6-4 – Circuit fitting values from NMC impedance data

NMC		
	1.0 V	***2.4 V***
R_{Sol} (Ωcm^2)	25.7	50.2
R_{CT} (Ωcm^2)	90.2	46.8
D (cm^2s^{-1})	9.23 x10^{-11}	1.21 x10^{-8}
$\boldsymbol{\delta}$(cm)	5.66 x10^{-6}	4.3 x10^{-4}

Hybrid Al-Li batteries are a very interesting and promising area of research which will benefit from more in-depth study and evolution to further increase the reversibility and capacity by utilising Li salt in electrolyte.

Table 6-5 – Battery performance summary

Electrode	Spec. Cap. ($mAhg^{-1}$)	Spec. Energy ($Whkg^{-1}$)	Coulombic Efficiency (%)	Degradation Rate ($mAhg^{-1}cycle^{-1}$)
Graphite	294.8	500.5	95	-3.19 (over 8 cycles)
NMC	57.7	41.7	59	1.10
Carbon Black	56.1	64.4	-	0.174
rGO	35.6	43.1	89	0.047
Co_3O_4	8.43	4.2	88	0.39
MnO_2	7.64	13.1	-	-
WO_3	4.83	3.7	89	0.024
$CoAl_2O_4$	1.07	0.9	16	0.025
$NiCo_2O_4$	0.443	0.3	89	0.037

6.3 Conclusion

From this study it can be seen that carbonaceous materials outperform all others due to their layered structure and conductive nature. Intercalation into graphite allowed for a large specific capacity of 295 $mAhg^{-1}$ and a specific energy of 500 $Whkg^{-1}$. This is directly due to the exfoliated graphite's intercalation ability which resulted in a GIC consisting of 7.6 mols of carbon for every mole of chloroaluminate, far below reported molar ratios, which allows for a higher charge density. Carbon black and reduced graphene oxide perform well with specific capacities 56.1 and 35.6 $mAhg^{-1}$ respectively, although this is caused by the high surface area of these materials resulting in electro-adsorption and double layer capacitance. The adsorption properties of reduced graphene oxide were slow resulting in impedance spectra displaying an inductance loop at low frequencies. All carbon electrodes achieved coulombic efficiencies above 89%, however the ≈100% for carbon black is not accurate due to the capacities measured.

The use of lithium NMC cathode with an aluminium anode to form a hybrid lithium-aluminium cell resulted in a specific capacity of 58 $mAhg^{-1}$, greater than both carbon black and rGO, albeit at the cost of coulombic efficiency of only 59% due to lack of Li salt in electrolyte. The capacity and

stability could be further improved to utilise NMC 200 $mAhg^{-1}$ intercalation capacity of Li^{+} if Li salt was added to the electrolyte. However, while cell voltage will remain at least 1.4 V lower than that of Li-ion batteries it would replace less abundant, more expensive Li (in graphite) anodes with Al anodes.

Limiting factors for the cells include the resistance from the separator which could be reduced along with a reduction in the thickness of the separator. However, this means that the overall volume of the electrolyte will also have to be reduced; a lower electrolyte volume leads to fewer available charge transfer ions and therefore a reduced cell capacity.

In the future compositing materials with activated carbon should allow for the electrodes to overcome any inherent resistance and increase key performance results such as intercalation ability and specific capacity without causing large double layer capacitances, as witnessed with carbon black and reduced graphene oxide.

Chapter 7. Conclusion and Future Work

7.1 Conclusion

This project aimed to understand the working mechanism and potential limits of the electrolyte: 1-ethyl-3-methylimidazolium chloride/ aluminium chloride for Al-ion batteries. Via voltammetric scans, the oxidation of the neutral 1:1 melt started at 0.9 V vs Ag/AgCl and resulted in the oxidation of $AlCl_4^-$ ions into chlorine gas. The electrolyte reduction reaction started at -1.7 V vs Ag/AgCl and is believed to produce a carbene. With the further addition of $AlCl_3$ the electrolyte, the melt becomes acidic e.g. 1-ethly-3-methylimidazolium chloride/ aluminium chloride 1:1.3 forming $Al_2Cl_7^-$ and increasing the oxidation potential to 2 V vs Ag/AgCl. Mass spectrometry of this electrolyte showed that HCl was released due to instantaneous reaction of chlorine gas with humidity traces in the carrier gas.

The presence of $AlCl_4^-$ alone within the electrolyte inhibits the plating of aluminium which require $Al_2Cl_7^-$ ion. In the 1:1.3 acidic melt electrolyte, Al striping and plating on an aluminium metal anode was very rapid and reversible with an overpotential of up to 0.6 V at a current density of 40 $mAcm^{-2}$.

The operating voltage of the 1:1.3 electrolyte cell is realistically limited to less than 2.5 V between the aluminium plating voltage at around -0.2 V and the onset of degradation at 2 V vs Ag/AgCl. It was shown that an aluminium pseudo-reference experiences a shift in its potential vs Ag/AgCl in accordance with the Nernst equation during operation as the ratio of chloroaluminate complexes ($AlCl_4^-/Al_2Cl_7^-$) changes within the electrolyte on charging/discharging. This results in a concentration gradient of these ions in the cell impacting the anode and cathode potentials, and reactions. In other words, the 1-ethyl-3-methylimidazolium chloride/ aluminium chloride electrolyte in Al-ion batteries affects the capacity of the battery as it contains active ingredients in a similar way to redox flow batteries.

From this study, it can be noted that a balance is encountered when using a smaller cell with a lower volume of electrolyte; a decrease in inter-electrode distancing result in lower IR losses in the cell, however the limited electrolyte volume will limit the cells capacity significantly due to the limited amount of $AlCl_4^-$ and $Al_2Cl_7^-$ available. The ideal cell design would be that of redox flow batteries: a thin separator to allow low IR losses (higher power density) and a circulating external electrolyte reservoir to minimise concentration gradient in the cell and improve capacity (higher energy density).

Cathode material studies showed that using 1:1 Emim/ $AlCl_3$ electrolyte, both carbon black and reduced graphite oxide demonstrated quasi-reversible electro-adsorption in addition to double layer charging/discharging. However, low coulombic efficiencies were obtained due to chloroaluminate oxidation from 1 V vs Ag/AgCl. Graphite also did not perform well with 1:1 electrolyte due to the chloroaluminate oxidation competing with the intercalation reaction at same potential window starting around 1 V vs Ag/AgCl. When using 1:1.3 acidic electrolyte, graphite exhibited greater performance as the oxidation stability window of the electrolyte increased beyond 2 V vs Ag/AgCl, allowing for $AlCl_4^-$ intercalation with a coulombic efficiency of 96%.

Through full-cell testing, carbon-based materials outperformed all other cathode materials studied due to layered structure which enabled intercalation, and high electrical conductivity in comparison to metal oxides. A specific capacity of 295 $mAhg^{-1}$ and a specific energy of 500 $Whkg^{-1}$ were achieved. This translates to a graphite intercalation compound consisting of a 7.6:1 molar ratio of carbon to $AlCl_4^-$, similar to that reported for Li^+ of 6 and far below reported values. The relatively low energy and specific capacity of AIBs combined with affordability make AIBs ideal for stationary applications e.g. renewable energy storage. Carbon black and rGO exhibited specific capacities of 56.1 and 35.6 $mAhg^{-1}$ respectively, although this is caused by surface electro-adsorption of $AlCl_4^-$ only, with no evidence of intercalation.

Ex-situ Raman spectroscopy of graphite after charging indicates intercalation has taken place through formation of a D' peak resulting from G peak splitting in graphite. This demonstrates the onset of intercalant staging within the graphitic layers. A higher wavelength laser could be required to capture more of the intercalant staging with a greater shift in the G peak. STM demonstrated intercalation in between graphite layers through increased inter-layer height comparable to the diameter of $AlCl_4^-$ with the expansion of only select layers indicating lower stage intercalation. The insertion and de-insertion of ions caused observable disorder in the graphite layers in line with disorder from the D bands of the Raman spectra. Graphite XRD patterns show the onset of intercalation, achieving a calculated intercalant staging of 9 and a 4.66 Å gallery height which could fit an $AlCl_4^-$ ion at 5.28 Å given contraction of adjacent layers.

Graphite's ability to intercalate large ions is attractive for battery research, however it has still demonstrated irreversibility surrounding the intercalation as XRD revealed the structure did not return to its original form upon discharge due to the stresses caused by interlayer expansion and contraction at high potentials. Pushing for higher potentials to further charge the cell would

maximise intercalation but also comes with an increased risk of electrode degradation from further expansion as well as electrolyte degradation as chloroaluminate ions are oxidised at similar potentials.

Performance of metal-oxide positive electrode materials, WO_3 and MnO_2 was poor when compared to carbon-based electrodes, primarily due to the structural phase inhibiting intercalation of the large $AlCl_4^-$ ion. The exception is a hybrid battery utilising NMC lithium-based positive electrode (Li-intercalation) alongside the chloroaluminate electrolyte and Al metal anode with a specific capacity of 58 $mAhg^{-1}$.

When looking at commercial scalability of aluminium ion batteries, the low voltage, and low capacities (low energy density) seen in this study do not warrant scaling up. However, the performance of graphite merits more research into feasibility of commercialisation due to the relatively larger energy density observed up to 500 $Whkg^{-1}$. The automotive industry would benefit from a low-cost aluminium battery that has a large power density however, this is not feasible yet due capacity degradation rates, limited cell voltage, and the electrolyte limiting the cell capacity and resistance. Aluminium ion batteries could at this time be used where there are no strict size/weight constraints, such as backup power for stationary application.

7.2 Limitations of the study

There are some limitations that should be noted, to do with the carrying out of this research. Constantly adapting the methodology to suit the acidic nature of the electrolyte presented an unexpected challenge to overcome. The air and humidity sensitivity of the electrolyte also hindered analytical experiments requiring ad hoc solutions and new equipment and cell designs.

Time limitation was a key factor surrounding heavily sought time slots for the use of characterisation equipment. While time management is a key area for development for upcoming researchers, COVID-19 and other experimental challenges, (for example discontinuity of the electrolyte supply), and characterisation delays from fabrication of bespoke cells affected and delayed the progress of sample preparation, which may have negatively affected results.

7.3 Future Work

Areas of study that were not fully covered within this study or areas that future research should focus on are listed below:

- Further study into new electrolytes that have higher oxidation stability to allow higher cathode capacity and battery energy density. The reaction scheme for the formation of HCl upon electrolyte degradation which could adequately conclude the degradation products of chloride-based electrolytes by for example examining ultra-dry special gas carriers and Differential Electrochemical Mass Spectrometry.
- Cathodes were seen to be the limiting factor in AIBs due to the limited capacity and stability caused by large $AlCl_4^-$ size. Extending the cathode electrode materials research for AIBs that can support $AlCl_4^-$ intercalation as materials for energy application is a continuously evolving field and new materials are always emerging. Materials exploration which can be refined through modelling and crystallographic studies can identify new intercalation hosts for chloroaluminates.
- Hybrid lithium-aluminium batteries could be an interim solution to overcome the limitation of graphite anode limited capacity and cracking, by introducing abundant aluminium into the commercial battery market. Future research should include lithium salts in addition to that of Al in the electrolyte and study electrolyte composition and volume effects on capacity and lifetime.

References

1. *Lithium Ion Battery: Powering a Device*. 25/09/2020]; Available from: https://witcomputers.com/wp-content/uploads/2018/11/lithium-ion-battery-powering-device.png.
2. *Yoshio Nishi Biography*. 01/10/20]; Available from: https://www.nae.edu/105800/Yoshio-Nishi.
3. Goodenough, J.B., *A New Cathode Material For Batteries Of High Energy Density.* Material Research Bulletin, 1980. **15**(6).
4. *Lithium share price*. 01/10/20]; Available from: https://tradingeconomics.com/commodity/lithium.
5. Wang, Q., et al., *Thermal runaway caused fire and explosion of lithium ion battery.* Journal of Power Sources, 2012. **208**: p. 210-224.
6. Yamaki, S.-i.T.K.T.Y.S.J.-i., *Lithium ion cell safety.* Journal of Power Sources, 2000. **90**.
7. *Aluminium share price*. 01/10/20]; Available from: https://tradingeconomics.com/commodity/aluminum.
8. Brown, G. and M.P. Paranthaman, *Aluminium Ion Battery*. Oak Ridge National Laboratory.
9. Alias, N. and A.A. Mohamad, *Advances of aqueous rechargeable lithium-ion battery: A review.* Journal of Power Sources, 2015. **274**: p. 237-251.
10. Hou, Y., et al., *Macroporous LiFePO4 as a cathode for an aqueous rechargeable lithium battery of high energy density.* Journal of Materials Chemistry A, 2013. **1**(46): p. 14713-14718.
11. Ruffo, R., et al., *Electrochemical characterization of LiCoO2 as rechargeable electrode in aqueous LiNO3 electrolyte.* Solid State Ionics, 2011. **192**(1): p. 289-292.
12. Liu, S., et al., *Aluminum storage behavior of anatase TiO2 nanotube arrays in aqueous solution for aluminum ion batteries.* Energy & Environmental Science, 2012. **5**(12).
13. Lahan, H. and S.K. Das, *Reversible Al(3+) ion insertion into tungsten trioxide (WO3) for aqueous aluminum-ion batteries.* Dalton Trans, 2019. **48**(19): p. 6337-6340.
14. Lahan, H. and S.K. Das, *Al3+ ion intercalation in MoO3 for aqueous aluminum-ion battery.* Journal of Power Sources, 2019. **413**: p. 134-138.
15. Wang, F., et al., *Aqueous Rechargeable Zinc/Aluminum Ion Battery with Good Cycling Performance.* ACS Appl Mater Interfaces, 2016. **8**(14): p. 9022-9.
16. Petrowsky, M., et al., *Mass and charge transport in cyclic carbonates: implications for improved lithium ion battery electrolytes.* J Phys Chem B, 2013. **117**(19): p. 5963-70.
17. Prakash Reddy, V., M. Blanco, and R. Bugga, *Boron-based anion receptors in lithium-ion and metal-air batteries.* Journal of Power Sources, 2014. **247**: p. 813-820.
18. Mjalli, F.S., et al., *Tetrabutylammonium Chloride Based Ionic Liquid Analogues and Their Physical Properties.* Journal of Chemical & Engineering Data, 2014. **59**(7): p. 2242-2251.
19. Blomgren, S.D.J.a.G.E., *Low Temperature Molten Salt Electrolytes Based on Aralkyl Quaternary or Ternary Onium Salts.* Journal of The Electrochemical Society, 1989. **136**(2): p. 424-427.
20. Fullarton, C., *Working towards a New Sustainable Rechargeable Battery; Zinc, Conducting Polymer and Deep Eutectic Solvent System*, in *Department of Chemistry*. 2014, University of Leicester. p. 230.
21. Gao, P., et al., *VOCl as a Cathode for Rechargeable Chloride Ion Batteries.* Angewandte Chemie International Edition, 2016. **55**(13): p. 4285-4290.
22. Zhao, X., et al., *Metal oxychlorides as cathode materials for chloride ion batteries.* Angew Chem Int Ed Engl, 2013. **52**(51): p. 13621-4.

23. Hu, M., X. Pang, and Z. Zhou, *Recent progress in high-voltage lithium ion batteries.* Journal of Power Sources, 2013. **237**: p. 229-242.
24. Lin, M.C., et al., *An ultrafast rechargeable aluminium-ion battery.* Nature, 2015. **520**(7547): p. 325-8.
25. Canever, N., N. Bertrand, and T. Nann, *Acetamide: a low-cost alternative to alkyl imidazolium chlorides for aluminium-ion batteries.* Chem Commun (Camb), 2018. **54**(83): p. 11725-11728.
26. *Lithium batteries*, ed. J.-P. Gabano. 1983, New York: Academic Press Inc.
27. Xu, C., et al., *AlCl3/pyridinium chloride electrolyte-based rechargeable aluminum ion battery.* Materials Letters, 2020. **275**.
28. Li, C., et al., *A Novel Moisture-Insensitive and Low-Corrosivity Ionic Liquid Electrolyte for Rechargeable Aluminum Batteries.* Advanced Functional Materials, 2020. **30**(12).
29. Chiku, M., et al., *Aluminum Bis(trifluoromethanesulfonyl)imide as a Chloride-Free Electrolyte for Rechargeable Aluminum Batteries.* Journal of The Electrochemical Society, 2017. **164**(9): p. A1841-A1844.
30. Lee, D., G. Lee, and Y. Tak, *Hypostatic instability of aluminum anode in acidic ionic liquid for aluminum-ion battery.* Nanotechnology, 2018. **29**(36): p. 36LT01.
31. Dong, X., et al., *Commercial expanded graphite as high-performance cathode for low-cost aluminum-ion battery.* Carbon, 2019. **148**: p. 134-140.
32. Lee, H., et al., *A review of recent developments in membrane separators for rechargeable lithium-ion batteries.* Energy Environ. Sci., 2014. **7**(12): p. 3857-3886.
33. Cheng, S., D.M. Smith, and C.Y. Li, *How Does Nanoscale Crystalline Structure Affect Ion Transport in Solid Polymer Electrolytes?* Macromolecules, 2014. **47**(12): p. 3978-3986.
34. Mori, R., *A novel aluminium–Air rechargeable battery with Al2O3as the buffer to suppress byproduct accumulation directly onto an aluminium anode and air cathode.* RSC Advances, 2014. **4**(57): p. 30346.
35. Kobayashi, Y., et al., *Trivalent Al3+ Ion Conduction in Aluminum Tungstate Solid.* Chemistry of Materials, 1997. **9**(7): p. 1649-1654.
36. Mori, R., *A new structured aluminium–air secondary battery with a ceramic aluminium ion conductor.* RSC Advances, 2013. **3**(29): p. 11547.
37. Sun, H., et al., *A new aluminium-ion battery with high voltage, high safety and low cost.* Chem Commun (Camb), 2015. **51**(59): p. 11892-5.
38. Hideaki OHTSUKA, A.Y., *Preparation And Electrical Conductivity Of Lisicon Thin Films.* Solid State Ionics 1983. **8**.
39. Yokoyama, Y., et al., *Origin of the Electrochemical Stability of Aqueous Concentrated Electrolyte Solutions.* Journal of The Electrochemical Society, 2018. **165**(14): p. A3299-A3303.
40. Vila, J., et al., *Electrical conductivity of aqueous solutions of aluminum salts.* Phys Rev E Stat Nonlin Soft Matter Phys, 2005. **71**(3 Pt 1): p. 031201.
41. Abbot;, A.P., R.C. Harris;, and K.S. Ryder, *Application of Hole theory to Define Ionic Liquids by their Transport Properties.* Journal of Physical Chemistry, 2007. **111**: p. 4910-4913.
42. Fullarton, C., *Working towards a New Sustainable Rechargeable Battery; Zinc, Conducting Polymer and Deep Eutectic Solvent System*, in *Chemistry*. 2014, University of Leicester.
43. Obeten, M.E., B.U. Ugi, and N.O. Alobi, *A review on electrochemical properties of choline chloride based eutectic solvent in mineral processing.* Journal of Applied Sciences and Environmental Management, 2017. **21**(5).

44. Gelman, D., B. Shvartsev, and Y. Ein-Eli, *Aluminum–air battery based on an ionic liquid electrolyte.* J. Mater. Chem. A, 2014. **2**(47): p. 20237-20242.
45. Chen, H., et al., *Oxide Film Efficiently Suppresses Dendrite Growth in Aluminum-Ion Battery.* ACS Appl Mater Interfaces, 2017. **9**(27): p. 22628-22634.
46. Besenhard, J.O. and H.P. Fritz, *The Electrochemistry of Black Carbons.* Angewandte Chemie International Edition in English, 1983. **22**(12): p. 950-975.
47. Gao, Y., et al., *Understanding Ultrafast Rechargeable Aluminum-Ion Battery from First-Principles.* The Journal of Physical Chemistry C, 2017. **121**(13): p. 7131-7138.
48. Bhauriyal, P., A. Mahata, and B. Pathak, *The staging mechanism of AlCl4 intercalation in a graphite electrode for an aluminium-ion battery.* Phys Chem Chem Phys, 2017. **19**(11): p. 7980-7989.
49. Greco, G., et al., *Influence of the electrode nano/microstructure on the electrochemical properties of graphite in aluminum batteries.* Journal of Materials Chemistry A, 2018. **6**(45): p. 22673-22680.
50. EunJoo Yoo, J.K., Eiji Hosono, Hao-shen Zhou, Tetsuichi Kudo, and Itaru Honma, *Large Reversible Li Storage of Graphene Nanosheet Families for Use in Rechargeable Lithium Ion Batteries.* American Chemical Society, 2008. **8**(8).
51. Lian, P., et al., *Large reversible capacity of high quality graphene sheets as an anode material for lithium-ion batteries.* Electrochimica Acta, 2010. **55**(12): p. 3909-3914.
52. Wang, G., et al., *Self-Activating, Capacitive Anion Intercalation Enables High-Power Graphite Cathodes.* Adv Mater, 2018. **30**(20): p. e1800533.
53. Elia, G.A., et al., *Insights into the reversibility of aluminum graphite batteries.* Journal of Materials Chemistry A, 2017. **5**(20): p. 9682-9690.
54. Shkolnikov, E.I., et al., *Carbon materials as a cathode for aluminum-ion battery.* Materials Today: Proceedings, 2018. **5**(12): p. 26073-26077.
55. Li, Z., et al., *A Novel Graphite-Graphite Dual Ion Battery Using an AlCl3 -[EMIm]Cl Liquid Electrolyte.* Small, 2018. **14**(28): p. e1800745.
56. Ji, H., et al., *Ultrathin graphite foam: a three-dimensional conductive network for battery electrodes.* Nano Lett, 2012. **12**(5): p. 2446-51.
57. Wu, Y., et al., *3D Graphitic Foams Derived from Chloroaluminate Anion Intercalation for Ultrafast Aluminum-Ion Battery.* Adv Mater, 2016. **28**(41): p. 9218-9222.
58. Wang, S., et al., *Aluminum Chloride-Graphite Batteries with Flexible Current Collectors Prepared from Earth-Abundant Elements.* Adv Sci (Weinh), 2018. **5**(4): p. 1700712.
59. Wang, D.Y., et al., *Advanced rechargeable aluminium ion battery with a high-quality natural graphite cathode.* Nat Commun, 2017. **8**: p. 14283.
60. Tu, J., et al., *Nickel Phosphide Nanosheets Supported on Reduced Graphene Oxide for Enhanced Aluminum-Ion Batteries.* ACS Sustainable Chemistry & Engineering, 2019. **7**(6): p. 6004-6012.
61. Walter, M., et al., *Polypyrenes as High-Performance Cathode Materials for Aluminum Batteries.* Adv Mater, 2018. **30**(15): p. e1705644.
62. Gulbinska, M.K., *Lithium-ion battery materials and engineering : current topics and problems from the manufacturing perspective*, ed. M.K. Gulbinska. 2014: London : Springer.
63. Chen, C.H., et al., *Aluminum-doped lithium nickel cobalt oxide electrodes for high-power lithium-ion batteries.* Journal of Power Sources, 2004. **128**(2): p. 278-285.
64. Sun, X.G., et al., *A high performance hybrid battery based on aluminum anode and LiFePO4 cathode.* Chem Commun (Camb), 2016. **52**(8): p. 1713-6.

65. Li, H.-H., et al., *Shale-like Co3O4for high performance lithium/sodium ion batteries.* Journal of Materials Chemistry A, 2016. **4**(21): p. 8242-8248.
66. Komaba, S., et al., *Electrochemical Insertion of Li and Na Ions into Nanocrystalline Fe[sub 3]O[sub 4] and α-Fe[sub 2]O[sub 3] for Rechargeable Batteries.* Journal of The Electrochemical Society, 2010. **157**(1).
67. Liu, J., et al., *Nanosphere-rod-like Co3O4 as high performance cathode material for aluminium ion batteries.* Journal of Power Sources, 2019. **422**: p. 49-56.
68. Huang, H. and P.G. Bruce, *A 4 V Lithium Manganese Oxide Cathode for Rocking-Chair Lithium-Ion Cells.* Journal of The Electrochemical Society, 1994. **141**(9): p. 1-2.
69. Wei, J., et al., *Molybdenum Oxide as Cathode for High Voltage Rechargeable Aluminum Ion Battery.* Journal of The Electrochemical Society, 2017. **164**(12): p. A2304-A2309.
70. Suto, K., et al., *Electrochemical Properties of Al/Vanadium Chloride Batteries with AlCl3-1-Ethyl-3-methylimidazolium Chloride Electrolyte.* Journal of The Electrochemical Society, 2016. **163**(5): p. A742-A747.
71. Tu, J., et al., *Ordered WO3-x nanorods: facile synthesis and their electrochemical properties for aluminum-ion batteries.* Chem Commun (Camb), 2018. **54**(11): p. 1343-1346.
72. Wang, W., et al., *A new cathode material for super-valent battery based on aluminium ion intercalation and deintercalation.* Sci Rep, 2013. **3**: p. 3383.
73. Chiku, M., et al., *Amorphous Vanadium Oxide/Carbon Composite Positive Electrode for Rechargeable Aluminum Battery.* ACS Appl Mater Interfaces, 2015. **7**(44): p. 24385-9.
74. Yu, T., et al., *Nanoconfined Iron Oxychloride Material as a High-Performance Cathode for Rechargeable Chloride Ion Batteries.* ACS Energy Letters, 2017. **2**(10): p. 2341-2348.
75. Plunkett, L., *Investigation into the Relationship between an Ionic Liquid Electrolyte and the Capacity and Recharge Ability of Aluminium Ion Batteries*. 2016, Newcastle University.
76. *Lithium-ion discharge curve*. 22/10/20]; Available from: https://siliconlightworks.com/li-ion-voltage
77. Zhang, X., et al., *A Novel Aluminum–Graphite Dual-Ion Battery.* Advanced Energy Materials, 2016. **6**(11): p. 1502588.
78. Frenzel, N., J. Hartley, and G. Frisch, *Voltammetric and spectroscopic study of ferrocene and hexacyanoferrate and the suitability of their redox couples as internal standards in ionic liquids.* Phys Chem Chem Phys, 2017. **19**(42): p. 28841-28852.
79. Ni, W., et al., *The determination of 1-methylimidazole in room temperature ionic liquids based on imidazolium cation by cyclic voltammetry.* Journal of Electroanalytical Chemistry, 2017. **787**: p. 139-144.
80. Zhang, L., et al., *Large-Sized Few-Layer Graphene Enables an Ultrafast and Long-Life Aluminum-Ion Battery.* Advanced Energy Materials, 2017. **7**(15).
81. Horcas, I., et al., *WSXM: a software for scanning probe microscopy and a tool for nanotechnology.* Rev Sci Instrum, 2007. **78**(1): p. 013705.
82. Qian, Q., Y. Yang, and H. Shao, *Solid electrolyte interphase formation by propylene carbonate reduction for lithium anode.* Phys Chem Chem Phys, 2017. **19**(42): p. 28772-28780.
83. Kiyoshi Kanamura, T.O., Zen-ichiro Takehara, *Electrochemical oxidation of propylene carbonate (containing various salts) on aluminium electrodes.* Journal of Power Sources, 1995. **57**.
84. Aldous, L., et al., *Electrochemical studies of gold and chloride in ionic liquids.* New J. Chem., 2006. **30**(11): p. 1576-1583.

85. Zhang, Q., Y. Hua, and R. Wang, *Anodic oxidation of chloride ions in 1-butyl-3-methyl-limidazolium tetrafluoroborate ionic liquid.* Electrochimica Acta, 2013. **105**: p. 419-423.
86. Constanza Villagran, C.E.B., Christopher Hardacre, Richard G. Compton, *Electroanalytical Determination of Trace Chloride in Room-Temperature Ionic Liquids.* Anal Chem, 2004. **76**(7).
87. Jian Xie, T.L.R., *Electrochemistry of 1 -Ethyl-3-methylimidazolium Chloride in Acetonitrile.* Journal of the Electrochemical Society, 1998. **145**(8).
88. Gorodetsky, B., et al., *Electrochemical reduction of an imidazolium cation: a convenient preparation of imidazol-2-ylidenes and their observation in an ionic liquid.* Chem Commun (Camb), 2004(17): p. 1972-3.
89. Romann, T., et al., *Surface chemistry of carbon electrodes in 1-ethyl-3-methylimidazolium tetrafluoroborate ionic liquid – an in situ infrared study.* Electrochimica Acta, 2014. **125**: p. 183-190.
90. Richard T. Carlin, W.C., Michael Bersch, *Nucleation and Morphology Studies of Aluminum Deposited from an Ambient-Temperature Chloroaluminate Molten Salt.* Journal of The Electrochemical Society, 1992. **139**(10).
91. Song, G.L., *Corrosion behavior and prevention strategies for magnesium (Mg) alloys*, in *Corrosion Prevention of Magnesium Alloys*. 2013. p. 3-37.
92. Wang, H., et al., *Anion-effects on electrochemical properties of ionic liquid electrolytes for rechargeable aluminum batteries.* Journal of Materials Chemistry A, 2015. **3**(45): p. 22677-22686.
93. Ng, K.L., et al., *A low-cost rechargeable aluminum/natural graphite battery utilizing urea-based ionic liquid analog.* Electrochimica Acta, 2019. **327**.
94. Sun, S., et al., *Flexible and rechargeable electrochromic aluminium-ion battery based on tungsten oxide film electrode.* Solar Energy Materials and Solar Cells, 2020. **207**.
95. Almodóvar, P., et al., *δ-MnO2 Nanofibers: A Promising Cathode Material for New Aluminum-Ion Batteries.* ChemElectroChem, 2020. **7**(9): p. 2102-2106.
96. Jedvik, E., et al., *Size and shape of oxygen vacancies and protons in acceptor-doped barium zirconate.* Solid State Ionics, 2015. **275**: p. 2-8.
97. Thummavichai, K., et al., *In situ investigations of the phase change behaviour of tungsten oxide nanostructures.* R Soc Open Sci, 2018. **5**(4): p. 171932.
98. Roscher, S., R. Hoffmann, and O. Ambacher, *Determination of the graphene–graphite ratio of graphene powder by Raman 2D band symmetry analysis.* Analytical Methods, 2019. **11**(9): p. 1224-1228.
99. Das, S.K., *Graphene: A Cathode Material of Choice for Aluminum-Ion Batteries.* Angew Chem Int Ed Engl, 2018. **57**(51): p. 16606-16617.
100. Dimiev, A.M., et al., *Stage Transitions in Graphite Intercalation Compounds: Role of the Graphite Structure.* The Journal of Physical Chemistry C, 2019. **123**(31): p. 19246-19253.
101. Pimenta, M.A., et al., *Studying disorder in graphite-based systems by Raman spectroscopy.* Phys Chem Chem Phys, 2007. **9**(11): p. 1276-91.
102. Ejigu, A., et al., *Electrochemically Exfoliated Graphene Electrode for High-Performance Rechargeable Chloroaluminate and Dual-Ion Batteries.* ACS Appl Mater Interfaces, 2019. **11**(26): p. 23261-23270.
103. Hodkiewicz, J., *Characterizing Carbon Materials with Raman Spectroscopy*, T.F. Scientific, Editor.
104. Min, Y.H. and W.H. Park, *Investigation of out-of-plane structural properties of a graphene monolayer with gap-plasmons: mode-selective Raman enhancement and the influence of additional sp(3) type defects.* Phys Chem Chem Phys, 2014. **16**(47): p. 26385-8.

105. Aunkor, M.T.H., et al., *The green reduction of graphene oxide.* RSC Advances, 2016. **6**(33): p. 27807-27828.
106. McKerracher, R.D., et al., *Comparison of carbon materials as cathodes for the aluminium-ion battery.* Carbon, 2019. **144**: p. 333-341.
107. Xu, H., et al., *Capacitive charge storage enables an ultrahigh cathode capacity in aluminum-graphene battery.* Journal of Energy Chemistry, 2020. **45**: p. 40-44.
108. Smajic, J., et al., *Mesoporous Reduced Graphene Oxide as a High Capacity Cathode for Aluminum Batteries.* Small, 2018. **14**(51): p. e1803584.
109. Märker, K., et al., *Evolution of Structure and Lithium Dynamics in LiNi0.8Mn0.1Co0.1O2 (NMC811) Cathodes during Electrochemical Cycling.* Chemistry of Materials, 2019. **31**(7): p. 2545-2554.

Chapter 8. Appendices.

8.1 Appendix 1.

8.1.1 Electrolyte Preparation

Stock 1:1 Emic / $AlCl_3$ electrolyte comes in a 5-gram bottle.

Emic / $AlCl_3$ has a molar mass of 279.96 $gmol^{-1}$

5 grams / 279.96 $gmol^{-1}$ gives the moles of stock electrolyte and therefore the number of moles of both the Emic and the $AlCl_3$ present.

$$m_{Emic} \div M_{Emic/AlCl_3} = mols_{Emic/AlCl_3} = mols_{Emic} = mols_{AlCl_3}$$

$$\frac{5}{279.96} = 0.01786\ mols$$

To increase the molar ratio of the Emic / $AlCl_3$ electrolyte to 1:1.3, an additional 0.3 moles of powdered $AlCl_3$ needs to be added to the stock liquid electrolyte. Therefore 30% of the number of moles of $AlCl_3$ is calculated and multiplied by the molar mass of $AlCl_3$ (133.34 $gmol^{-1}$) to determine how much powdered $AlCl_3$ to add.

$$\left(mols_{AlCl_3} \times 30\%\right) \times M_{AlCl_3} = m_{AlCl_3}$$

$$0.01786 \times 0.3 = 0.005358\ mols$$

$$0.005358 \times 133.34 = 0.7144\ grams$$

0.7144 g of $AlCl_3$ is added to the stock 1:1 electrolyte to produce 1:1.3 Emic / $AlCl_3$.

8.1.2 Cathode Catalyst Preparation

To calculate the required catalyst material to be applied with a loading of 1 $mgcm^{-2}$ onto a glassy carbon electrode with a 1 cm diameter:

$$\pi \times 0.5^2 = 0.785\ cm^2$$

$$1\ mgcm^{-2} \times\ 0.785\ cm^2\ =\ 0.785\ mg$$

The amount of the binding agent (PVDF) needed is taken to be 10% of the amount of catalyst required. The associated solvent volumes are 0.1 ml of IPA per 1 mg of catalyst, and 0.33 ml per 1 mg of PVDF:

- PVDF: $0.785\ mg \times\ 10\%\ =\ 0.0785\ mg$
- IPA: $0.1 \times 0.785 = 0.0785\ ml$

- THF: $0.33 \times 0.0785 = 0.02618\ mg$

A Bulk / Loss factor of 20 is included in the calculations to scale-up and make the preparation more manageable and due to losses incurred. The make-up remains proportional.

- Catalyst: $0.785 \times 20 = 15.7mg$
- PVDF: $0.0785 \times 20 = 1.57mg$
- THF: $0.02618 \times 20 = 0.524ml$
- IPA: $0.0785 \times 20 = 1.57ml$

The catalyst is mixed with the IPA and ultrasonicated for 30 mins while the PVDF is mixed with the THF and ultrasonicated for 15 mins. Both suspensions are combined and ultrasonicated for a further 30 mins.

8.2 Appendix 2.

8.2.1 Theoretical Gravimetric Energy Density Calculation

The theoretical capacity and gravimetric energy density of AIBs and LIBs will change depending on the battery materials used. The most commonly reported values come from batteries using Mn_2O_4 therefore so will these calculations.

Theoretical capacity is calculated using Faraday's law:

$$\frac{Q}{m} = \frac{zF}{M}$$

- $AlMn_2O_4$ has a molar mass of 200.854 $gmol^{-1}$
- Al has a valence of 3
- Faraday's constant is 96,485 $Cmol^{-1}$ where 1 C is equal to 1 A·s

$$\frac{zF}{M} = \frac{3 \times 96485}{200.854} = 1441.121\ Asg^{-1}$$

$$1441.121 \div 3600 = 0.4\ Ahg^{-1}$$

$$0.4 \times 1000 = 400\ Ahkg^{-1}$$

Gravimetric energy density is calculated by multiplying the theoretical capacity by the operating voltage, which is the case for the commonly reported AIBs is 2.65 V.

$$400 \times 2.65 = 1060\ Whkg^{-1}$$

For LIBs where:

- $LiMn_2O_4$ has a molar mass of 180.813 $gmol^{-1}$
- Li has a valence of 1

Theoretical capacity is calculated as:

$$\frac{1 \times 96485 \times 1000}{180.813 \times 3600} = 148.227\ Ahkg^{-1}$$

Gravimetric energy density is calculated using an operating voltage of 4 V:

$$148.227 \times 4 = 593\ Whkg^{-1}$$

8.2.2 Full Cell Result Calculations

8.2.2.1 Graphite

Experimental setup provides the current as 0.001 A and the weight of the catalyst as 4.99 mg.

The average discharge voltage comes out at 1.697 V over a runtime of 1.471 hours.

Charging took 1.542 hours.

Discharge Capacity: $0.001 \times 1.471 = 0.001471\ Ah$

Specific Discharge Capacity: $\frac{0.001471 \times 1000}{0.00499} = 294.8\ mAhg^{-1}$

Charge Capacity: $0.001 \times 1.542 = 0.001542\ Ah$

Specific Charge Capacity: $\frac{0.001542 \times 1000}{0.00499} = 309.02\ mAhg^{-1}$

Coulombic Efficiency: $\frac{294.8}{309.02} \times 100 = 95\%$

Specific Energy: $mAhg^{-1} = Ahkg^{-1}$

$$294.8 \times 1.697 = 500.5\ Whkg^{-1}$$

8.2.2.2 NMC

Experimental setup provides the current as 0.0001 A and the weight of the catalyst as 0.785 mg.

The average discharge voltage comes out at 0.728 V over a runtime of 0.45 hours.

Charging took 0.76 hours.

Discharge Capacity: $0.0001 \times 0.45 = 0.000045\ Ah$

Specific Discharge Capacity: $\frac{0.000045 \times 1000}{0.000785} = 57.68\ mAhg^{-1}$

Charge Capacity: $0.0001 \times 0.76 = 0.000076\ Ah$

Specific Charge Capacity: $\frac{0.000076 \times 1000}{0.000785} = 96.8\ mAhg^{-1}$

Coulombic Efficiency: $\frac{57.68}{96.8} \times 100 = 59\%$

Specific Energy: $mAhg^{-1} = Ahkg^{-1}$

$$57.68 \times 0.728 = 41.7\ Whkg^{-1}$$

8.2.2.3 Carbon Black

Experimental setup provides the current as 0.00005 A and the weight of the catalyst as 0.785 mg.

The average discharge voltage comes out at 1.21 V over a runtime of 0.835 hours.

Charging took 0.224 hours.

Discharge Capacity: $0.00005 \times 0.835 = 0.0000418\ Ah$

Specific Discharge Capacity: $\frac{0.0000418 \times 1000}{0.000785} = 53.16\ mAhg^{-1}$

Charge Capacity: $0.00005 \times 0.224 = 0.0000112\ Ah$

Specific Charge Capacity: $\frac{0.0000112 \times 1000}{0.000785} = 14.27\ mAhg^{-1}$

Coulombic Efficiency: $\frac{53.16}{14.27} \times 100 = 373\%$

Specific Energy: $mAhg^{-1} = Ahkg^{-1}$

$$56.13 \times 1.21 = 64.4\ Whkg^{-1}$$

8.2.2.4 rGO

Experimental setup provides the current as 0.00005 A and the weight of the catalyst as 0.785 mg.

The average discharge voltage comes out at 1.21 V over a runtime of 0.559 hours.

Charging took 0.63 hours.

Discharge Capacity: $0.00005 \times 0.559 = 0.000028\ Ah$

Specific Discharge Capacity: $\frac{0.000028\times1000}{0.000785} = 35.6\ mAhg^{-1}$

Charge Capacity: $0.00005 \times 0.63 = 0.0000315\ Ah$

Specific Charge Capacity: $\frac{0.0000315\times1000}{0.000785} = 40.13\ mAhg^{-1}$

Coulombic Efficiency: $\frac{35.6}{40.13} \times 100 = 89\%$

Specific Energy: $mAhg^{-1} = Ahkg^{-1}$

$$35.6 \times 1.21 = 43.1\ Whkg^{-1}$$

8.2.2.5 Co_3O_4

Experimental setup provides the current as 0.00001 A and the weight of the catalyst as 0.785 mg.

The average discharge voltage comes out at 0.498 V over a runtime of 0.66 hours.

Charging took 0.75 hours.

Discharge Capacity: $0.00001 \times 0.66 = 0.0000066\ Ah$

Specific Discharge Capacity: $\frac{0.0000066\times1000}{0.000785} = 8.43\ mAhg^{-1}$

Charge Capacity: $0.00001 \times 0.75 = 0.0000075\ Ah$

Specific Charge Capacity: $\frac{0.0000075\times1000}{0.000785} = 9.55\ mAhg^{-1}$

Coulombic Efficiency: $\frac{8.43}{9.55} \times 100 = 88\%$

Specific Energy: $mAhg^{-1} = Ahkg^{-1}$

$$8.43 \times 0.498 = 4.2\ Whkg^{-1}$$

8.2.2.6 MnO_2

Experimental setup provides the current as 0.000002 A and the weight of the catalyst as 0.785 mg.

The average discharge voltage comes out at 1.71 V over a runtime of 3 hours.

Charging took 0.01 hours.

Discharge Capacity: $0.000002 \times 3 = 0.000006\ Ah$

Specific Discharge Capacity: $\frac{0.000006 \times 1000}{0.000785} = 7.64\ mAhg^{-1}$

Charge Capacity: $0.000002 \times 0.01 = 0.00000002\ Ah$

Specific Charge Capacity: $\frac{0.00000002 \times 1000}{0.000785} = 0.025\ mAhg^{-1}$

Coulombic Efficiency: $\frac{7.64}{0.025} \times 100 = 30000\%$

Specific Energy: $mAhg^{-1} = Ahkg^{-1}$

$$7.64 \times 1.71 = 13.1\ Whkg^{-1}$$

8.2.2.7 WO_3

Experimental setup provides the current as 0.000005 A and the weight of the catalyst as 0.785 mg.

The average discharge voltage comes out at 0.76 V over a runtime of 0.76 hours.

Charging took 0.85 hours.

Discharge Capacity: $0.000005 \times 0.76 = 0.0000038\ Ah$

Specific Discharge Capacity: $\frac{0.0000038 \times 1000}{0.000785} = 4.83\ mAhg^{-1}$

Charge Capacity: $0.000005 \times 0.85 = 0.00000425\ Ah$

Specific Charge Capacity: $\frac{0.00000425 \times 1000}{0.000785} = 5.41\ mAhg^{-1}$

Coulombic Efficiency: $\frac{4.83}{5.41} \times 100 = 89\%$

Specific Energy: $mAhg^{-1} = Ahkg^{-1}$

$$4.83 \times 0.76 = 3.7\ Whkg^{-1}$$

8.2.2.8 $CoAl_2O_4$

Experimental setup provides the current as 0.000005 A and the weight of the catalyst as 0.785 mg.

The average discharge voltage comes out at 0.87 V over a runtime of 0.17 hours.

Charging took 1.07 hours.

Discharge Capacity: $0.000005 \times 0.17 = 0.00000085\ Ah$

Specific Discharge Capacity: $\frac{0.00000085\times1000}{0.000785} = 1.07\ mAhg^{-1}$

Charge Capacity: $0.000005 \times 1.07 = 0.00000535\ Ah$

Specific Charge Capacity: $\frac{0.00000535\times1000}{0.000785} = 6.82\ mAhg^{-1}$

Coulombic Efficiency: $\frac{1.07}{6.82} \times 100 = 16\%$

Specific Energy: $mAhg^{-1} = Ahkg^{-1}$

$$1.07 \times 0.87 = 0.9\ Whkg^{-1}$$

8.2.2.9 $NiCo_2O_4$

Experimental setup provides the current as 0.0000005 A and the weight of the catalyst as 0.785 mg.

The average discharge voltage comes out at 0.65 V over a runtime of 0.7 hours.

Charging took 0.78 hours.

Discharge Capacity: $0.0000005 \times 0.7 = 0.00000035\ Ah$

Specific Discharge Capacity: $\frac{0.00000035\times1000}{0.000785} = 0.443\ mAhg^{-1}$

Charge Capacity: $0.0000005 \times 0.78 = 0.00000039\ Ah$

Specific Charge Capacity: $\frac{0.00000039\times1000}{0.000785} = 0.496\ mAhg^{-1}$

Coulombic Efficiency: $\frac{0.443}{0.496} \times 100 = 89\%$

Specific Energy: $mAhg^{-1} = Ahkg^{-1}$

$$0.443 \times 0.65 = 0.3\ Whkg^{-1}$$